

Universität Stuttgart

A moving bed reactor for thermochemical energy storage based on metal oxides applied for concentrated solar power plants

A thesis accepted by the Faculty of Energy-, Process- and Bio-Engineering of the
Universität Stuttgart to fulfill the requirements for the degree of
Doctor of Engineering Sciences (Dr.-Ing.)

by

Nicole Carina Neumann
born in Wiesbaden

Main referee: Prof. Dr. André Thess
Co-referee: Assoc. Prof. Dr. Henrik Leion

Date of oral exam: 21.10.2020

Institute for Building Energetics, Thermotechnology and Energy Storage

2020

Erklärung

Hiermit versichere ich, Nicole Carina Neumann, die vorliegende Arbeit ohne Hilfe Dritter und nur mit den angegebenen Quellen und Hilfsmitteln angefertigt zu haben. Alle Stellen, die Quellen entnommen wurden, sind als solche kenntlich gemacht worden. Diese Arbeit hat in gleicher oder ähnlicher Form noch keiner Prüfungsbehörde vorgelegen. In der abgegebenen Arbeit stimmen die schriftliche und elektronische Fassung überein.

Contents

Kurzfassung	9
Abstract	11
1 Introduction	13
1.1 Motivation	13
1.2 A CSP plant operated with metal oxide particles	14
1.3 State of the art	16
1.3.1 Metal oxide candidates for thermochemical energy storage	16
1.3.2 Reactors for thermochemical energy storage based on the redox reaction of metal oxides	21
1.4 Objectives	25
1.4.1 Scientific contributions	26
2 Publications	29
2.1 List of publications	29
2.2 Paper I	31
2.3 Paper II	45
2.4 Paper III	69
3 Discussion and conclusion	91
3.1 The impact of the modification of manganese-iron-oxide particles on their stability and handling	91
3.2 The effect of the oxidation on a moving bed operation	93
3.3 Evaluation of the manganese-iron-oxide application as TCS material for a continuous CSP system	96
4 Summary	99
Bibliography	101

Acknowledgments

It is my pleasure to thank those who made this thesis possible. In particular, I would like to thank:

- My dissertation advisor Prof. Dr. André Thess for his support during the last years, providing me with the opportunity to perform my research at the Institute of Engineering Thermodynamics at DLR, and the explanation why DLR is like apple juice or why a research question can be solved by comparing it to a fruit fly.
- My dissertation examiner Prof. Dr. Henrik Leion for making my research visits at Chalmers a great success and for the helpful advice during my stay there.
- My direct supervisor Dr. Marc Linder for his patience, enthusiastic encouragement, professional guidance, and for pushing me farther than I thought I could go. I highly appreciate your effort during the last years.
- Dr. Inga Bürger for her patience and very helpful advice concerning numerical issues.
- Andreas Kohzer for his technical and physical support and making seemingly impossible things possible. You made my time at TT very enjoyable.
- Niklas Giesen and Sofie Ek who wrote their thesis' under my supervision, for their valuable help, especially in terms of experimental work.
- All the previous and the present TCS colleagues: Andrea, Andreas, Christian, Christoph, Inga, Jana, Jonina, Kai, Marc, Marie, Matthias, Michael, and Mila. Working in the TCS group with you was just the right mixture of professional discussions, enthusiastic ideas, and simply having fun doing research.

Last but not least, I would like to thank my parents and grandparents for their full support, and for showing me that you can achieve everything with the right amount of ambition. Finally, I would like to thank my partner Kai for his encouragement and patience throughout this journey. Without whom I would have struggled to find the inspiration and motivation needed to complete this dissertation.

Kurzfassung

In der vorliegenden Arbeit wird die Wärmeauskopplung aus einem Metalloxidpartikelstrom untersucht, im Hinblick auf eine Anwendung der Metalloxide als thermochemisches Energiespeichermaterial in einem punktfokussierenden solarthermischen Kraftwerk. Der Schwerpunkt liegt auf der kombinierten Nutzung der thermischen und thermochemischen Energie der Metalloxide, aufgrund des hohen Temperaturniveaus von ca. 1000 °C am Partikeleintritt. Die Eignung eines Wanderbettreaktors in Gegenstromprinzip für die direkte Wärmeübertragung zwischen Metalloxidpartikelstrom und Gasstrom wird experimentell und numerisch analysiert. Dabei dient Mangan Eisenoxid ($(\text{Mn}_{0.7}\text{Fe}_{0.3})_2\text{O}_3$) wegen seiner chemischen Zyklenfestigkeit und geeigneten Reaktionstemperatur als Referenzmaterial. Aufgrund der bekannten Neigung zur Agglomeratbildung nach mehreren Redoxzyklen, wird zunächst die Wirkung einer Modifikation des Mangan Eisenoxides mit jeweils 20 % ZrO_2 , CeO_2 oder TiO_2 auf die Partikelstabilität und chemischen Reaktivität experimentell untersucht. Um den Einsatz in einem Wanderbettreaktor zu ermöglichen wird ZrO_2 als geeignetes Additiv identifiziert, da hiermit die Agglomerationsbildung stark eingeschränkt und die mechanische Stabilität verbessert werden kann. Die Wechselwirkung zwischen der temperatur- und druckabhängigen effektiven Reaktionsgeschwindigkeit und den Stoff- und Wärmetransportmechanismen wird numerisch mit einem 1D FEM Modell sowie experimentell im Maßstab von 2 kW für einen Wanderbettreaktor ermittelt. Beide Untersuchungen zeigen, dass die Oxidation eine nahezu isotherme Schicht im Wanderbett bewirkt, worauf ein Segment mit einem ausgeprägten Temperaturgradienten anschließt. Die numerische Analyse ergibt, dass der vorwiegende Anteil des Reaktionsumsatzes in dem Segment mit Temperaturgradient erfolgt. Allerdings hemmt dort bei geringeren Temperaturen die Reaktionsgeschwindigkeit den Reaktionsumsatz und führt zu einer limitierten Energiedichte der Mn-Fe-Oxid Partikel sowie Leistungsdichte des Reaktors. In dieser Arbeit wurde gezeigt, dass die untersuchte Betriebsweise mit dem eingesetzten Mangan Eisenoxid keine signifikanten Vorteile aufweist, da die Reaktionsgeschwindigkeit keinen vollständigen Reaktionsumsatz unter leistungsoptimierten Bedingungen zulässt. Eine Möglichkeit zur Steigerung des Reaktionsumsatzes wäre, die Wärme während der Reaktion indirekt und isotherm abzuführen und für einen geeigneten Hochtemperaturprozess zur Verfügung zu stellen.

Abstract

This thesis deals with the heat extraction from a metal oxide particle flow with regard to an application of the metal oxides as thermochemical energy storage for a point-focused solar power plant. The focus is on the combined utilization of the thermal and thermochemical energy of the metal oxides, due to their initial high temperature level of around 1000 °C. The suitability of a moving bed reactor for the direct heat transfer between a metal oxide particle flow and a counter-current gas flow is analyzed experimentally and numerically. Here, manganese-iron oxide ($(\text{Mn}_{0.7}\text{Fe}_{0.3})_2\text{O}_3$) serves as reference material, as it features high chemical cycle stability, environmental compatibility of the raw materials and suitability of the reaction temperature. From literature, the tendency to form agglomerates after several redox cycles is known, which is why a modification of the material was investigated in this thesis in order to enhance particle stability and handling. The addition of mostly inert ZrO_2 or CeO_2 diminished the agglomeration after several redox cycles, and especially ZrO_2 significantly improved the mechanical stability of the particles. Therefore, the manganese-iron oxide was modified with 20 % ZrO_2 to impede agglomeration and thus to enable the continuous operation of the moving bed reactor. The interrelation between the temperature and pressure dependent reaction rate and heat and mass transfer mechanisms in the moving bed reactor was examined experimentally in scale of 2 kW as well as numerically by means of a 1D FEM model. Both reveal two characteristic temperature segments of the moving bed. At first, the particles travel through a nearly isothermal bed segment, which can be attributed to the exothermic oxidation reaction, followed by a segment with a pronounced temperature gradient, where the sensible cooling dominates the temperature profile. The numeric analysis indicates that the temperature gradient segment contributes most to the extent of conversion. However, the temperature dependency of the reaction rate limits the extent of conversion at lower temperatures and thus the energy and power density of the reactor due to high cooling rates of the direct heat transfer operation. In the end, an additional indirect heat transfer to an isothermal high temperature process in the nearly isothermal segment of the moving bed could increase the oxidation conversion and thus the energy and power density of the reactor.

1 Introduction

The redox reaction of metal oxides can be applied for thermochemical energy storage in e.g. concentrated solar thermal power plants. Due to the elevated temperature level, the combined utilization of both the thermochemical and thermal energy of the metal oxides is crucial for enhanced system efficiency and energy storage density. The presented thesis contributes in this context with numerical and experimental investigations of the heat extraction in a moving bed reactor, which is designed for direct heat transfer between a metal oxide particle flow and a counter-current air flow and thus corresponds to the discharging step of the thermal energy storage system. Furthermore, it is examined whether the increased material requirements resulting from the continuous operation of the reactor can be compensated by metal oxide modifications.

1.1 Motivation

How can the electrical power supply of an ever growing world population be reconciled with criteria of sustainability, environmental compatibility and economics?

The discussion of the environmental compatibility of various energy conversion processes for electricity generation is largely dominated by the amount of greenhouse gas emissions correlated to the respective technology. As a result, the world wide electricity generation based on renewable energy sources increased by 59 % from 2009 to 2017, accounting for a share of 24.4 % of total electricity generation in 2017 [1]. Despite the promising development of the renewable energy sector, the inherent intermittent character of solar and wind power limits its growth. To decouple the energy supply from these renewable sources from the energy demand, energy storage systems are indispensable. Thermal energy storage plays a key role when large capacities have to be provided and especially when the renewable energy source is originally in form of thermal energy, such as in concentrated solar thermal power (CSP) plants [2]. The combination of CSP plants and thermal energy storage systems can compensate for weather instabilities and extend the operating time into the evening hours or even bridge the day-night cycle, thus enabling a renewable base load supply at lower levelized costs [3]. For example, the Shouhang Dunhuang 100 MW Phase II CSP plant in China can be operated up to 11 hours after sunset due to a thermal energy storage based on molten salt [4].

Thermal energy storage can be divided into three categories according to the inherent physical mechanism: Sensible thermal energy storage, latent thermal energy storage or thermochemical energy storage. Sensible thermal energy storage is the most mature

technology, followed by latent thermal energy storage, where thermal energy is stored or released at a specific temperature via the phase transition between in general solid and liquid phases with the corresponding latent heat. In contrast, the concept of thermochemical energy storage (TCS) is based on a chemically reversible reaction, e.g., of a gas and a solid. Here, the charging process of the thermal storage corresponds to the endothermic reaction, whereas the discharge represents the reverse exothermic reaction, whereby the previously chemically bound reaction enthalpy is released again. By keeping the solid and gas separately, the energy can be stored potentially loss-free and indefinitely in the chemical bonds at ambient temperature [2, 5]. Although TCS systems promise the highest energy densities in comparison to the other thermal energy storage technologies, they are the least developed technology so far. The reaction systems that are suitable for TCS cover a wide temperature range, e.g., from -20°C in case of the ab-/desorption reaction of coupled metal hydride [6] to 1400°C in case of the redox reaction of $\text{Fe}_2\text{O}_3 / \text{Fe}_3\text{O}_4$ [5]. Due to the high operation temperature of CSP plants, chemically reversible redox reactions of metal oxides are promising, as they react at elevated temperatures between 700°C and 1400°C [5, 7, 8, 9, 10]. These reactions can be described by the following generic reaction equation:



Here, MeO_{ox} and MeO_{red} symbolize the oxidized and reduced phase of the metal oxide, respectively. Since ambient air can provide the required oxygen for the oxidation reaction, the gas handling is simplified and open reactors are feasible without the need of gas storage [2]. This fact presents a major advantage in comparison to other TCS systems for high temperature applications, e.g., hydrates (e.g. $\text{CaO} / \text{Ca}(\text{OH})_2$ with H_2O) or carbonates (e.g. $\text{CaO} / \text{CaCO}_3$ with CO_2).

1.2 A CSP plant operated with metal oxide particles

A solar tower power plant with the integration of metal oxides as TCS material and heat transfer medium is schematically illustrated in Fig. 1.1. The presented system concept is based on a metal oxide particle loop between a solar receiver for charging (reduction) and a separate reactor for discharging (oxidation). In addition, two storage tanks at a high and low temperature level enable the decoupling of the system's capacity and thermal power. The principle application of particles as a heat transfer medium and storage material for point-focusing CSP plants has been initially investigated for sensible thermal energy storage [11, 12, 13, 14]. In this context, particle temperatures of 990°C were already successfully demonstrated [15] and are further expected to rise above 1000°C [16]. A

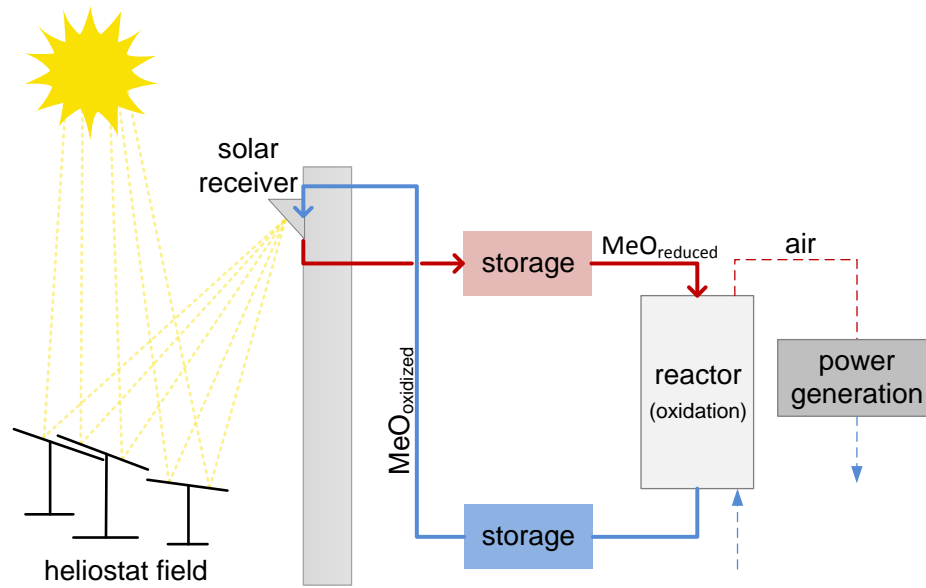


Figure 1.1 System concept of a concentrated solar tower plant based on metal oxide particles as heat transfer medium and thermochemical storage material.

similar concept for thermochemical materials was suggested by Schrader et al. [17] employing the phase transition $\text{CoO} / \text{Co}_3\text{O}_4$, however, for a pressurized and thus closed system. The thermodynamic evaluation revealed that a higher gas outlet temperature of the oxidation reactor due to increased gas pressures yields higher system efficiencies, although an additional compression power is required.

However, due to the elevated temperature level of the charging step, it is crucial in both cases to extract not only the thermochemical energy of the metal oxides, but also the inherent sensible thermal energy to enhance system efficiency and the energy density of the particles. This idea of a hybrid thermochemical/sensible storage material was originally suggested for honeycomb structures coated with, e.g., $\text{Co}_3\text{O}_4 / \text{CoO}$ or $\text{Mn}_2\text{O}_3 / \text{Mn}_3\text{O}_4$ [18]. The demonstration in a lab-scale setup indicated a beneficial effect of the oxidation on the exhaust gas temperature in case of cobalt oxide coated honeycombs in comparison to a purely sensible honeycomb. In contrast, a coating with Mn_3O_4 did not enhance the air outlet temperature during cooling [19]. Jafarian et al. [20] went one step further and investigated a process based on cobalt oxide, where sensible, latent and thermochemical energy is utilized as thermal storage for a CSP plant. In this concept, the solar receiver first reduces and then liquefies the solid cobalt oxide particles, while the discharging step is performed in two separated oxidation and quenching reactors. A process analysis revealed that the oxidation reactor can be operated at a constant temperature and flow rate, despite

a variable diurnal solar insolation.

In contrast to the investigated concepts, an open operation of the presented CSP system (compare Fig. 1.1) could reduce the system's complexity to a level that is comparable to an application with inert particles as sensible thermal energy storage, while still exploiting the potential higher energy density. For the realization of this CSP system, the solar receiver and oxidation reactor need to be designed to ensure the non-isothermal redox reaction of a continuous metal oxide flow (see Section 1.3.2). Besides, the metal oxide particles need to meet material requirements like high reaction enthalpy, long-term cycle stability, sufficient particle flowability and mechanical strength or low cost of the raw materials.

1.3 State of the art

The following sections present the state of the art regarding the application of metal oxides for thermochemical energy storage and existing reactor concepts in this field. The first section gives an overview about potential metal oxide candidates including system relevant material properties. The subsequent section focuses on experimentally investigated reactor concepts for the redox reaction of metal oxides.

1.3.1 Metal oxide candidates for thermochemical energy storage

In the last decade, several material screenings of metal oxide candidates were performed with regard to an application as TCS material [5, 9, 10, 21]. Furthermore, the redox reaction of metal oxides is also applied for water splitting or carbon dioxide splitting in the field of solar fuels [22, 23, 24, 25] or in chemical-looping combustion (CLC), where metal oxides act as an oxygen carrier [26, 27, 28, 29]. General Atomics evaluated 74 metal oxide candidates based on thermodynamic equilibrium data, from which 16 possible redox reactions for the application as TCS emerged [5]. Apart from iron oxide and copper oxide, particularly cobalt oxide, manganese oxide and barium oxide were favored candidates as TCS material in the context of a CSP system. The operating temperature, materials costs, and results of a thermogravimetric analysis (TGA) concerning reaction kinetics and thermal cycle stability as well as tests in a fixed bed reactor and a rotary kiln were considered [5].

The most promising pure metal oxides are compared concerning their theoretical gravimetric energy density at the particular equilibrium temperature for an oxygen partial pressure of 21 kPa with sintered bauxite as a widely applied sensible thermal energy storage material in Fig. 1.2. The sensible share in energy density is based on a lower temperature limit of 300 °C. For a simpler illustration of the sensible part and the thermochemical part of the energy density, it is shown for a temperature range around the equilibrium

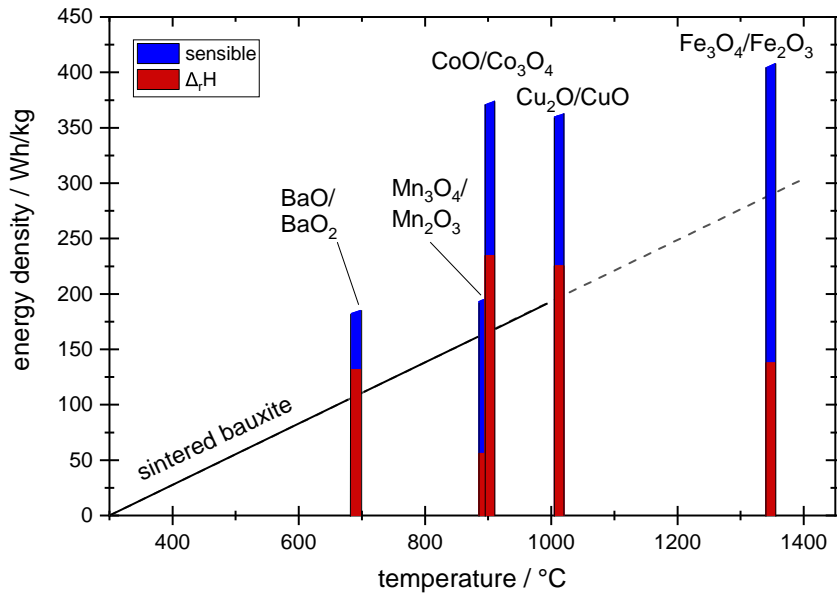


Figure 1.2 Gravimetric energy density of selected pure metal oxides in comparison to sintered bauxite as sensible energy storage material. The sensible share in energy density is based on a lower temperature of 300 °C and an averaged specific heat capacity [30, 31]. In case of a metal oxide, the energy density is depicted at a temperature range around the respective theoretical equilibrium temperature for an oxygen partial pressure of 21 kPa [9, 30] and based on the theoretical reaction enthalpy [5] plus the sensible share of energy density.

temperature. The combined utilization of sensible thermal energy and thermochemical energy offers the potential for higher energy densities compared to pure sensible thermal energy storage. Furthermore, Fig. 1.2 illustrates the influence of the varying reaction enthalpies and equilibrium temperatures on the achievable energy density.

Cobalt oxide (CoO / Co₃O₄) is one of the most investigated metal oxide materials in field of TCS owing to its high reaction enthalpy of 844 kJ/kg, based on the oxidized phase Co₃O₄, with an equilibrium temperature of 890 °C in air [5]. In addition, superior chemical reversibility is reported for 100 redox cycles by means of TGA [32]. However, cobalt oxide poses a potential carcinogenic health risk to human and animals and is rather costly with a raw material price of 20 €/kg [33].

Manganese oxide has several stable phases: MnO₂, Mn₂O₃, Mn₃O₄ and MnO. The redox reaction from MnO₂ to Mn₂O₃ is irreversible in air atmosphere at ambient pressure and the reduction temperature of the phase transition Mn₃O₄ / MnO is with around 1700 °C too high for current application in CSP [5]. In contrast, the phase transition (Mn₃O₄ / Mn₂O₃) is reported with an oxidation temperature between 500 °C and 850 °C, and reduction

temperatures between 920 °C and 1000 °C [34]. The reaction enthalpy determined with TGA ranged from 110 kJ/kg to 160 kJ/kg [34], which is below the theoretical reaction enthalpy of 202 kJ/kg [5]. Nevertheless, the low toxicity and low cost of manganese oxide results in a promising candidate for TCS at high temperatures. However, a slow oxidation behavior of Mn_3O_4 is frequently observed, leading to the necessity of low cooling rates [35, 18, 34]. A lower particle size was found to promote the densification of the sample during 30 redox cycles in TGA, which impedes the O_2 diffusion during oxidation, resulting in lower oxidation temperature and reaction rates [35]. The experimentally gained transition temperature of the forward and reverse direction of the redox reaction did vary in many studies by a difference of up to 281 K [5, 8, 36]. This so-called 'thermal hysteresis' describes a temperature range where especially the oxidation takes a long time to initiate and proceed.

The redox reaction of *barium oxide* ($\text{BaO} / \text{BaO}_2$) was already considered for application as TCS material in 1978 [37]. However, limited work has been published for this reaction system. The redox reaction was reported as reversible but with decreasing conversion after the first redox cycle performed with TGA [5]. The authors assumed that a layer of BaO_2 was formed on the surface and acted as a diffusion barrier, which slowed the re-oxidation. Several studies agree with the low cycle stability [38] or also report an incomplete redox reaction of $\text{BaO} / \text{BaO}_2$ [5, 37]. However, an impurity of Sr was discovered to foster the reaction after some initial cycles for a sample containing 95 % BaO_2 [39]. The authors found sufficient cycle stability over 30 cycles with a reaction enthalpy of 390 kJ/kg for samples with eliminated carbonate impurities. Furthermore, barium oxide is more abundant than cobalt oxide and less toxic [39].

The application of *iron oxide* ($\text{Fe}_3\text{O}_4 / \text{Fe}_2\text{O}_3$) as thermochemical energy storage material offers the advantage of high availability of the raw material, which is also of low cost and non-toxic. However, a minimum reduction temperature of 1361 °C in an atmosphere containing 20 % O_2 or 1145 °C in an atmosphere of Ar was determined with TGA [10]. Furthermore, Block and Schmücker [9] detected significant sintering effects after 3 redox cycles with a powder sample.

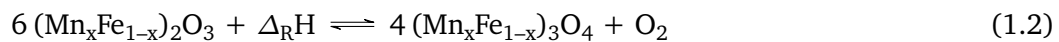
Copper oxide ($\text{Cu}_2\text{O} / \text{CuO}$) was found to have a comparable reaction enthalpy to cobalt oxide of 811 kJ/kg [5]. In addition, copper oxide is cost competitive and available in areas, which are attractive for CSP. The transition between CuO and Cu_2O in air takes place at temperatures around 700 °C to 1000 °C, but the melting point of Cu_2O of 1232 °C is close and could cause problems like grain coarsening [5]. Hänchen et al. [40] reported a decrease in O_2 capture capacity with increasing number of cycles, which was assumed to be caused by degradation and/or gas bypassing in the shrinking bulk. Agrafiotis et al. [21] investigated two CuO powders in TGA. Both powders showed a reduction at around 1040 °C, but strongly decreasing re-oxidation potential (- 50 % conversion after

one reduction). Adjusting the heating/cooling rate and dwell time at different temperature levels slightly improved the re-oxidation, but overall it was concluded that the phase transition between CuO and Cu₂O can not be reproducibly and quantitatively cycled even for a few cycles. Poor reversibility was also reported by Alonso et al. [41]. While the reduction reaction is rather fast [9], the re-oxidation was rather slow [5].

Criteria such as energy density, material price, long-term cycle stability, environmental compatibility and toxicity of the chosen metal oxide play a decisive role with regard to the material selection for a potential large-scale application in open reactor concepts. Furthermore, the reaction temperature for ambient pressure application needs to be in range of near future solar receiver temperatures. Non of the so far presented pure metal oxides meet all the described criteria to an acceptable degree.

Recent research focuses on the adjustment and improvement of redox materials by incorporating a second or tertiary metal cation [5]. In these *mixed oxides*, some primary oxide cations are replaced by secondary cations causing a lattice charge imbalance and thus enlargement of the anion vacancy density. The re-oxidation is faster, because the ionic mass transport is increased by such vacancies. In addition, mixed solid oxides show stabilized or improved long-term properties, which could be partially induced by a reduced grain size of mixed oxides. Finally, the operation temperature can be adjusted and mixed oxides can become cost efficient, due to mixing of low cost with some more expensive oxides [5, 42]. As a result, many binary or tertiary metal oxides were recently investigated like Co-Fe-oxides [34, 43], Co-Mn-oxides [8], Mn-Fe-oxides [34, 36, 44, 45] or Mn-Si-oxides [46]. Furthermore, the non-stoichiometric reaction of perovskites is suggested [47].

Manganese-iron oxides promise a long-term cycle stability [5, 45], a reduced temperature gap of reduction and oxidation (thermal hysteresis) in comparison to the redox couple Mn₃O₄ / Mn₂O₃ and faster re-oxidation reaction rates [36]. Therefore, the manganese-iron-oxide system was chosen as a reference material for this thesis. Thermodynamic and experimental investigations of the manganese-iron-oxide system reveal several stable phases for applications in air, depending on the temperature and manganese-to-iron ratio. At lower temperatures the oxidized phases in form of the cubic bixbyite phase [(Fe³⁺, Mn³⁺)₂O₃], and the trigonal hematite phase (Fe₂O₃) or a mixture are favored according to thermodynamics, whereas higher temperatures result in the reduced phase in form of a cubic spinel phase [(Fe²⁺, Mn²⁺)(Fe³⁺, Mn³⁺)₂O₄], a tetragonal hausmannite phase [(Mn²⁺)(Mn³⁺)₂O₄] or a mixture of both [34, 48, 49, 50, 51, 52]. However, the exact position of phase transitions varies between the published phase diagrams. The global reaction equation of manganese-iron-oxide



was experimentally verified for different molar ratios $x = Mn/(Mn + Fe)$ [5, 9, 34, 36]. The incorporation of Fe in the manganese-iron oxide enhanced the oxidation rate and cycle stability in most cases. Furthermore, the distinct thermal hysteresis of pure manganese oxide is diminished with increasing iron incorporation [36], although the reaction temperatures also rose [34]. The decreased thermal hysteresis is favorable, because considering a high temperature thermal energy storage, thermal hysteresis results in a loss of exergy [5]. In addition, an incorporation of Fe between 1 mol % and 40 mol % resulted in higher reaction enthalpies in comparison to the redox pair Mn_2O_3 / Mn_3O_4 [36]. For example, a reaction enthalpy of 233 kJ/kg was determined with simultaneous thermal analysis for a molar manganese ratio x of 67 % [9]. The long-term stability was investigated with 500 thermal redox cycles of a sample synthesized of MnO_2 with 0, 7.5, 10, 15, or 20 mol % Fe_2O_3 incorporation [5]. The mixed powders were annealed in air at a temperature of 900 °C for 100 h to form the phases $Mn_2O_3 + Fe_2O_3$. The authors suggested an optimal iron oxide composition of about 15 mol % (equaling 26 mol % Fe_2O_3 in Mn_2O_3), which indicated improved redox performance, especially of the reduction, with continued thermal cycling. However, sintering was observed independently of the Fe content, when comparing as-processed and cycled material after 3 cycles [34] or 30 cycles [36]. Microstructures of different manganese-iron oxides as-processed and after 500 cycles also revealed severe sintering behavior especially for an iron content of below 10 mol % (equaling 18 mol % Fe_2O_3 in Mn_2O_3) [5]. An incorporation of 10 mol % Fe resulted in a limited oxidation ability in the work of André et al. [34], from which was followed that sintering is not responsible for the limited re-oxidation and reactivity loss in case of pure Mn_2O_3 and Mn_2O_3 with 10 mol % Fe. Furthermore, André et al. [34] identified a minimum Fe content of around 15 mol % to avoid the formation of tetragonal spinel (Mn_3O_4), which impeded the re-oxidation. The evaluation of 30 redox cycles with 0, 1, 5, 10, 20 or 40 mol % Fe indicated that the addition of 20 mol % Fe promises the fastest oxidation reaction and the highest reaction enthalpy [36]. Furthermore, 100 redox cycles of a manganese-iron oxide with a molar Fe content of 25 % also resulted in sufficient cycle stability [45]. In summary, the presented studies suggest an incorporation of Fe of about 15 mol % to 26 mol % for higher energy density, long-term cycle stability and enhanced oxidation rates. The improved reaction characteristics are mainly attributed to the switch from a phase transition between the cubic bixbyite phase and tetragonal hausmannite phase to a phase transition between cubic bixbyite phase and cubic spinel phase [34, 36, 44]. Cubic spinel shows a higher reversibility of the redox reaction than tetragonal hausmannite, because in this crystal structure more Mn^{2+} are on octahedral sites, which is easier to oxidize than on tetragonal sites as is the case for tetragonal hausmannite [34]. One other possible reason for an improved oxidation rate with increasing Fe incorporation could be the increased oxidation temperature, allowing for faster oxidation rates [36].

Therefore, recent research indicates that the redox reaction of the manganese-iron oxide has the potential for an application as thermochemical energy storage with low raw material costs at a suitable reaction temperature for the CSP system. However, the design of the solar receiver and the oxidation reactor need to take the effective reaction kinetics of manganese-iron oxide into account to allow the combined utilization of thermochemical energy and sensible thermal energy. In addition, next to the apparently sufficient cycle stability of the redox reaction, a specific reactor concept might also require a high particle stability, which needs to be addressed to permit the long-term use of the particles.

1.3.2 Reactors for thermochemical energy storage based on the redox reaction of metal oxides

The system concept presented in Fig. 1.1 requires a solar receiver and oxidation reactor, which are able to reduce or oxidize a continuous particle flow. Beside the essential criteria of continuous operation, the reactors should guarantee a sufficient mass and heat transfer between gas and solid, adjustable residence time, low mechanical stress for the material and acceptable energy consumption of auxiliary devices, which is accompanied by a low pressure drop for the gas phase [53, 54]. Furthermore, the utilization of metal oxides as TCS material and heat transfer medium between the solar receiver and oxidation reactor facilitates an open mode operation, which leads to a simpler and cheaper reactor design due to less technical constraints like impermeability to gas or non-standard components [53].

So far, investigations of *solar receivers* for the reduction of metal oxides in particle shape for TCS are based on a rotary kiln concept [55, 41, 56], gravity-driven particle receivers [57, 58, 59], a fixed-bed concept [60], a conveying plate concept [61], a particle suspension concept [62] or a counter-flow fluidized bed concept [63]. Apart from modeling approaches and the reactor design of solar receivers based on metal oxide particles [57, 64, 61, 59, 62], extensive experimental experience was gained.

A rotary kiln reactor was tested with cobalt oxide based powders in a solar furnace operated at DLR in Cologne, Germany [55]. Up to 30 redox cycles proved the feasibility of the concept with a maximum extent of reduction conversion of 70 % and wall temperatures of up to 990 °C. Despite visible morphology changes due to sintering after the performed redox cycles, the conversion rate did not show a correlation with the reduced surface area. Insufficient mixing of the material was identified as one crucial improvement to support a higher extent of conversion [55].

Another rotary kiln reactor was operated at the solar furnace HoSIER in IER-UNAM, México with copper oxide particles in batch mode [41]. Wall temperatures up to 1000 °C could be demonstrated and an extent of reduction conversion of almost 80 % in case of

an atmosphere containing argon. However, the switch to an air atmosphere hindered the reduction, which caused the maximum extent of conversion to drop to 40 %. In addition, a decreasing reversibility of the redox reaction in the air atmosphere is reported, which could be correlated with an even stronger agglomeration and sintering of the particles in the presence of air instead of argon.

The first continuously working rotary kiln for a thermochemical energy storage based on manganese-iron oxide particles was investigated in a solar simulator at DLR in Cologne, Germany [56]. The receiver was closed with a window to enable the monitoring of the O_2 concentration in order to determine the reaction conversion. The first tests yielded an extent of a conversion of 40 % with wall temperatures up to 1058 °C. However, the extent of conversion is expected to increase by a prolonged residence time of the particles in the hot zone.

Furthermore, Nie et al. [59] propose a gravity-driven moving bed solar receiver. Here, particles flow through an absorbing section in quartz tubes, while they are heated by solar irradiation. The quartz tubes are filled with wear-resistant and ultra-refractory insert materials. So far, the flowability of inert particles in the tubes with an insert filling material has been demonstrated in a cold-state [65].

In addition, the phase transition of Mn_3O_4 / MnO was investigated with a fixed-bed reactor in a 7 kW solar simulator [60]. The crucible was heated to temperatures above 1400 °C in atmosphere with varying oxygen concentration. No complete reduction to MnO was observed with additional oxidation and reduction reactions including the phase Mn_2O_3 . Furthermore, a volume diminution of the particle bed and sintering of the particles resulting in different morphological structures were reported [60].

Moreover, the concept of a gravity-driven particle receiver in scale of 5 kW thermal power was demonstrated in the solar flux simulator in the Solar Fuels and Technologies Laboratory at Georgia Tech [58]. Calcium manganite granular powder was reduced and heated while flowing along an inclined plate in an irradiated cavity receiver. An intermittent flow behavior was reported, caused by slightly agglomerated heap of granular powder at the entrance of the incline. The total system efficiency nearly reached 70 % for steady-state operation regarding the achieved temperature increase of the particles and reduction conversion. Thus, an up-scaling to 100 kW is under progress.

In contrast to the extensive work on solar receiver design and demonstration, limited work has been published about *off-sun reactors*, which are suitable for the oxidation of metal oxide particles. A study about different contact pattern for thermochemical energy storage based on manganese oxide with gas as a heat transfer fluid for CSP plants indicated the advantage of continuously operated reactors in comparison to thermochemical batch reactors [66]. The authors conclude that a counter-current flow pattern between the heat transfer fluid and solid matter has the potential to enhance the gravimetric energy

storage density, in case of attained full chemical conversion and for cycling the solid matter between the outlet temperatures of the power block and the solar field. In this context, the application of moving bed reactors, multi-stage fluidized beds or rotary kiln is suggested for treating thermochemical storage materials as powders or granules [66].

Two types of particle based oxidation reactors are modeled for comparison in [67], namely a densely-fixed moving bed and a gravity-driven particle reactor. The reactors are designed for a later integration in an air Brayton cycle with a turbine inlet temperature of 1200 °C, thus, the reactors need to withstand 16.7 bar to deliver hot and pressurized air to the Brayton cycle. Based on this work, a counter-current falling-particle design was further elaborated as an oxidation reactor in scale of 1 kW thermal power [68]. The reactor is fed by preheated perovskite particles for subsequent oxidation and heat transfer to pressurized air flow in direct contact. The falling particles are dispersed by the counter-current air flow to enhance the heat transfer.

Furthermore, a reactor for fixed- or fluidized-bed operation for the redox reaction of pure manganese-oxide pellets or manganese-iron-oxide pellets (5 % Fe) was designed and demonstrated at the Universidad Politécnica de Madrid in cooperation with IMDEA [69]. The fixed-bed operation with manganese-oxide pellets resulted in a declining oxidation rate of the material after the first cycle with deactivated material after 25 cycles. The fluidized-bed operation improved the oxidation reactivity for a few more cycles and oxygen peaks, caused by the reduction reaction, were detectable up to 10 out of 25 performed cycles. Furthermore, the heat transfer between gas and solid was enhanced by the fluidization, which was determined by the highest achieved air temperatures of 960 °C. In contrast to the fixed-bed operation with pure manganese-oxide pellets, the manganese-iron-oxide pellets showed a redox reactivity for all 25 thermal cycles in a fixed-bed operation. However, the oxidation rate decreased with continued cycling. A material characterization revealed that all thermally cycled material exhibit a reduced average diameter and increased hardness in comparison to the initial material. However, sintering effects were visible in the lower bed height in case of the fixed-bed operation with pure manganese-oxide pellets.

The application of manganese-iron oxide particles as TCS material was also investigated in a fixed-bed reactor at DLR in Cologne, Germany [70]. The redox reaction of the particles caused a plateau of the bed temperatures, which moved in flow direction through the fixed bed. The bed temperatures were stabilized by the released or absorbed thermal energy offering a prolonged charging or discharging period in comparison to sensible thermal energy storage systems. Furthermore, the redox reaction affected the oxygen concentration in the air flow, which provided the oxygen for oxidation and acted as heat transfer fluid. A variation of air flow rates corroborated the $pO_2 - T$ -dependency of the reaction, which was identified by the achievement of the highest plateau temperatures when applying the highest air flow rate. Especially the lowest air flow rate did not provide sufficient amount

of O_2 and reduced the heat transport capability of the gas when the oxidation reaction proceeded with higher reaction rates, which resulted in a lower and prolonged plateau of bed temperatures. The variation of air inlet and initial bed temperatures revealed that the reaction process is accelerated for decreased temperatures during discharging due to the enhanced cooling effect. In the end, the authors concluded that the heat transport by the air capacity flow and not the reaction rate poses the limiting factor for the advancing reaction in the presented setup under the investigated operational parameters.

Metal oxides are also applied as oxygen carriers for CLC, which is a carbon capture and storage technology. The concept is based on the reduction and oxidation potential of metal oxides, which is utilized to oxidize fossil fuels in an oxygen-free atmosphere and re-oxidize in air. Here, especially the oxidation of granular metal oxides in a separate reactor, where the oxygen carriers are exposed to an atmosphere containing N_2 and O_2 , shows similarities with the application of metal oxides as thermochemical energy storage material. However, both the reduction and oxidation of the oxygen carriers is usually performed at isothermal conditions. Continuously operated reactors in the field of CLC are mainly designed as circulating fluidized beds [71, 72, 73, 74, 75], but also as moving beds [76, 77, 78, 79]. Abad et al. [72] present a continuously operated system consisting of two interconnected fluidized beds, one fuel reactor and one air reactor, with a thermal power of 1.5 kW. No agglomeration or defluidization was observed during the experiments with Cu-based oxygen carrier. Despite the decrease of oxygen in the air reactor due to the oxidation of the metal oxides, no significant influence of the exothermic reaction on the temperature in the air reactor is observed. These isothermal conditions in the air reactor were also found in the interconnected fluidized beds in Xu et al. [75], in spite of the re-oxidation of the Cu-modified manganese ores.

The fluidized bed in [71] was operated with manganese-iron oxide particles as oxygen carriers at Chalmers in Gothenburg, Sweden. The particles exhibited a low physical stability, but a sufficient oxygen release due to the reduction reaction when being fluidized in CO_2 above 850 °C. This system concept, which is composed of two interconnected fluidized beds was demonstrated with a thermal power of 100 kW by the same research group [73] or even up to 1 MW at the TU Darmstadt in Germany [74].

In contrast, Zeng et al. [78] present a bench-scale counter-current moving bed reactor for pretesting the isothermal oxidation of methane or syngas with iron-oxide based oxygen carriers at 900 °C to 950 °C. Sampling ports for the gas concentration along the bed height identified a region of inactive bed height, whose position was found to be a function of the iron oxide to methane flow ratio. The performed experiments in Tong et al. [76] and Zeng et al. [78] were pretest for a sub-pilot unit, which is composed of two counter-current moving bed reactors in a total scale of 25 kW [77, 76]. Both moving bed reactors are operated at isothermal conditions. In the 'reducer', the oxygen carrier Fe_2O_3 is reduced to

elemental Fe with methane as a reducing agent, whereas in the 'oxidizer', the elemental Fe is partially oxidized to Fe_3O_4 by steam to produce H_2 . A separate 'combustor', designed as a fluidized/entrained bed, provides the oxygen for a re-oxidation of the oxygen carrier to the phase Fe_2O_3 . A three day operation yielded nearly 100 % syngas conversion and hydrogen purity in the 'oxidizer' and 'reducer'.

A 30 kW moving bed reactor for CLC is operated at the Industrial Technology Research Institute in Kaohsiung, Taiwan [79, 80]. Particles in the size of 2.5 mm containing different amounts of iron-oxide (Fe_2O_3) modified with Al_2O_3 were applied as oxygen carriers. A temperature increase of 120 °C is reported for the 'combustor' which is attributed to the oxidation of Fe_3O_4 to Fe_2O_3 at solid temperatures between 640 °C to 760 °C by an counter-current air flow. Only minor attrition occurred which could be mainly caused by the fluidization in the riser connecting the 'combustor' at the top with the 'oxidizer' at the bottom of the setup.

In summary, the continuous reduction of a metal oxide particle flow has been already successfully demonstrated in solar receivers. However, no continuously operated reactor for non-isothermal oxidation of the metal oxides, which is necessary to utilize both the thermochemical and sensible share in energy density, has been reported so far. Based on the existing literature, the moving bed concept seems to be suitable for this specific and mandatory requirements of the oxidation reactor in a CSP plant.

1.4 Objectives

For a demand-oriented renewable power supply by means of CSP plants, the integration of thermal energy storage with an inherent decoupling of the storage capacity from the system power is indispensable. An innovative implementation due to high energy densities of the storage medium without increasing the system's complexity, is in the form of a continuously operated CSP system based on a particle flow of metal oxides, which serve as thermochemical energy storage material and heat transfer medium. Due to the elevated temperatures, it is crucial to utilize both the sensible thermal energy and the thermochemical energy of the metal oxide particles to maximize the system efficiency. Encouraging research has already been published on the integration of thermal energy, involving the reduction of the metal oxides, using solar receivers. However, the extraction of the thermal energy has not yet been sufficiently examined. Therefore, this thesis investigates the implementation of a continuously operated reactor based on the moving bed concept for the extraction of sensible thermal energy and thermochemical energy from a particle flow of metal oxide as well as the resulting material requirements. The work is performed on the basis of manganese-iron oxide acting as thermochemical storage material, as it has emerged as a promising reference material from the literature research.

1.4.1 Scientific contributions

The manganese-iron oxide particles have to meet several requirements for a long-term utilization in the suggested system concept. Next to chemical aspects like the reversibility of the redox reaction, mechanical or technical aspects need to be considered as well, e.g., attrition, agglomeration or flowability of the particles. However, the utilization of manganese-iron oxide particles as thermochemical energy storage material in a fixed bed reactor led to the formation of agglomerates after 17 consecutive redox cycles [70]. Results from fluidization experiments with different manganese-iron oxide particles in the context of CLC confirm this agglomeration tendency [81]. Beside defluidization of the bed caused by the agglomeration, the formation of fine dust was reported. The addition of inert supportive material to metal oxide particles showed a beneficial effect on the particle stability for application as oxygen carrier in CLC [82]. Therefore, **paper I** investigates the impact of the addition of ZrO_2 , CeO_2 or TiO_2 to manganese-iron oxide on agglomeration, attrition behavior and reactivity with regard to the specific conditions relevant for thermochemical energy storage. The different samples were treated in an attrition test rig, exposed to several redox cycles in a fixed bed reactor under harsh conditions and in a TGA to trigger mechanical, thermal or chemical stress. In the end, the most promising composition ($(\text{Mn}_{0.7}\text{Fe}_{0.3})_2\text{O}_3 + 20 \text{ wt.}\% \text{ZrO}_2$) allows the application in the presented system including the continuously operated reactors.

Besides the reacting material, the reactor for discharging (oxidation reactor) has to be understood and optimized with regard to the gas-solid heat transfer in order to ensure a maximum reaction conversion and the extraction of the inherent sensible thermal energy. In the reactor, the kinetics are interrelated with heat and mass transport mechanisms due to the pressure and temperature dependency of the reaction kinetics of the metal oxide. So far, no numeric investigation of a moving bed reactor considered the redox reaction of metal oxides concerning not only the extent of conversion but also the resulting temperature profile of the bed. Thus, **paper II** identifies the effect of the oxidation conversion and corresponding release of the reaction enthalpy on operational parameters, like mass flow and gas flow, as well as on the achievable energy density and thermal power. A transient 1D model for a counter-current moving bed is proposed, based on the oxidation of $(\text{Mn}_{0.75}\text{Fe}_{0.25})_3\text{O}_4$, which is used as reference material. To validate this model, experimental data from a fixed bed reactor are employed [70]. Sensitivity analyzes are carried out to investigate the limiting factors of the moving bed in the context of thermochemical energy storage application. The results reveal that the temperature dependency of the reaction rate inhibits the energy and power density of the moving bed reactor.

Finally, the experimental investigation of a counter-current moving bed reactor based

on modified manganese-iron oxide particles is presented in **paper III**. It is the first continuously operated reactor for non-isothermal oxidation of metal oxides. As the extraction of sensible thermal energy naturally reduces the temperature of the solid, the reaction rate of the thermochemical material is influenced. Hence, the impact of the reaction enthalpy release on the temperature profile in a moving bed reactor, working in steady-state, was experimentally studied. Additionally, the applicability of manganese-iron-oxide particles as heat transfer material and thermal storage medium is discussed.

2 Publications

2.1 List of publications

This thesis is based on the work contained in the following papers:

Paper I

Nicole Carina Preisner¹, Tina Block, Marc Linder, Henrik Leion. "Stabilizing Particles of Manganese-Iron Oxide with Additives for Thermochemical Energy Storage". *Energy Technology*, 6(11):2154-2165, **2018**. DOI: 10.1002/ente.201800211 *

Paper II

Nicole Carina Preisner¹, Inga Bürger, Michael Wokon, Marc Linder. "Numerical Investigations of a Counter-Current Moving Bed Reactor for Thermochemical Energy Storage at High Temperatures". *Energies*, 13(3), 772, **2020**. DOI: 10.3390/en13030772

Paper III

Nicole Carina Preisner¹, Marc Linder. "A Moving Bed Reactor for Thermochemical Energy Storage Based on Metal Oxides". *Energies*, 13(5), 1232, **2020**. DOI: 10.3390/en13051232

Contribution report

Paper I: Principal author, responsible for the experimental works - except for SEM imaging and XRD analysis - and data evaluation.

Paper II: Principal author, responsible for the numerical work and data evaluation.

Paper III: Principal author, responsible for the experimental works and data evaluation.

¹the surname changed from Preisner to Neumann during the work on this thesis.

*Reproduced with permission.

Additional scientific publications

During the work on this thesis the following publications were released in context of this thesis:

Nicole Carina Neumann, Henrik Leion, Dongmei Zhao, Michael Wokon, Marc Linder. "Particle stability investigation of Mn-Fe oxides supported by TiO₂, ZrO₂ or CeO₂ as thermochemical energy storage materials" Poster presentation at the 12th Material Science and Engineering Congress **MSE 2016** Darmstadt, Germany.

Nicole Carina Neumann, Marc Linder, Henrik Leion. "Thermochemical energy storage with manganese-iron oxides in a moving bed reactor" - Oral presentation at the 13th Doctoral Colloquium on Solar Concentrating Technologies **SOLLAB 2017**, Berlin, Germany

Nicole Carina Preisner, Niklas Giesen, Marc Linder. "A Moving Bed Reactor For Continuous Heat Extraction From Metal Oxides As Thermochemical Energy Storage" - Oral presentation at the 12th International Renewable Energy Storage Conference **IRES 2018**, Düsseldorf, Germany.

Nicole Carina Preisner, Sofie Ek, Marc Linder. "Experimental Investigation Of Continuous Heat Extra Of Metal Oxides In A Moving Bed Reactor" - Oral presentation at the 24th International Conference on Concentrating Solar Power and Chemical Energy Systems **SolarPACES 2018** in Casablanca, Marrocco. Conference paper published in **AIP Conference Proceedings** DOI: 10.1063/1.5117756

Reiner Buck, Stefania Tescari, Martin Schmücker, Nicole Carina Preisner, Christos Agrafiotis. "Techno-Economic Analysis of Thermochemical Storage for CSP Systems" - presented at the 25th International Conference on Concentrating Solar Power and Chemical Energy Systems **SolarPACES 2019**, in Daegu, South Korea. Conference paper to be published in **AIP Conference Proceedings**.

2.2 Paper I

Stabilizing Particles of Manganese-Iron Oxide with Additives for Thermochemical Energy Storage

N. C. Preisner,^{*,[a]} T. Block,^[b] M. Linder,^[a] and H. Leion^[c]

Manganese-iron oxide particles are a promising candidate for both chemical-looping combustion (CLC) and thermochemical energy storage. In CLC, the ability of metal oxides to oxidize fuels in an oxygen-free atmosphere and re-oxidize in air is addressed. Whereas, reaction enthalpy is the main focus of thermochemical energy storage for, e.g. concentrated solar power or an industrial process that requires high temperature levels. Sufficient mechanical strength of the particles while they endure chemical, thermal, or mechanical stress is a crucial factor for both concepts. Particle stability is investigated here by adding 20 wt.% of TiO_2 , ZrO_2 , or CeO_2 as a supportive material to $(\text{Mn}_{0.7}\text{Fe}_{0.3})_2\text{O}_3$. Thermal cyclization and temperature shock tests are conducted in a packed bed

reactor to identify chemical stability as well as the effect of chemical and thermal stress. A subsequent particle size distribution analysis is performed to determine the relevant breakage mechanism. Attrition resistance is tested with a customized attrition jet cup to estimate the mechanical strength of particles. It is found that the high tendency of unsupported manganese-iron oxide particles towards agglomeration can be improved with any of the chosen additives. The particles with CeO_2 , and especially with ZrO_2 , as an additive indicate an increase in resistance towards attrition. However, adding TiO_2 has a severe negative impact on the chemical reactivity of the manganese-iron oxide.

Introduction

The characteristic redox reaction of metal oxides is applied in several research fields, which are motivated by the necessity to mitigate global warming. Metal oxides are currently investigated for example as thermochemical energy storage material, for solar fuel production, and for chemical looping combustion. All of these applications utilize metal oxides in the form of particles and thus rely on a sufficient stability of the particles. Chemical looping combustion (CLC) is based on the ability of metal oxides (oxygen carriers) to oxidize in a reactor with air and carry oxygen to a fuel reactor, where the metal oxides react with gas-phase combustibles.^[1] In chemical looping with oxygen uncoupling (CLOU), the metal oxide releases gaseous oxygen in the fuel reactor, which is needed to oxidize not only the gas phase but also liquid and solid fuels.^[2] The exhaust gas of the fuel reactor consists of CO_2 and H_2O , which can be easily separated. The only exhaust from the air reactor is depleted air. Usually the concept is implemented in the form of two interconnected fluidized beds to allow a continuous operation with biomass, coal, methane, or any other fuel. Reactor setups are tested that range from lab-scale units,^[3,4] a 100 kW_{th} unit at Chalmers in Sweden,^[5] to a 1 MW_{th} pilot plant at TU Darmstadt, Germany.^[6] Recent promising metal oxide candidates are perovskites^[7] and Mn-combined oxides, e.g. manganese-iron oxides.^[8] Natural ores are successfully tested.^[9] Another application of metal oxides is the production of solar fuels, namely H_2 and CO , by splitting H_2O and CO_2 with metal oxides.^[10] The produced syngas can be further processed to denser liquid fuels via the Fischer-Tropsch process. The high temperature needed for reducing metal oxides in air is supplied by renewable sources, e.g. a concentrating solar power plant. Implemented reactor

concepts focus on porous structured metal oxides^[11] in a rotary kiln,^[12] moving particles in a fluidized bed reactor,^[13] a cavity reactor,^[14] a moving bed reactor,^[15–17] and a packed bed reactor.^[18–20]

Sustainable fuel conversion is the main objective of chemical looping and solar fuel research. However, the reaction enthalpy of the redox reaction is the main objective of thermochemical energy storage research. Thermochemical storage (TCS) systems are a promising way to increase the flexibility of concentrated solar power plants (CSP) or industrial processes operated at high temperature (700–1000 °C).^[21–26] Especially weather instability and expandable operation time can be addressed with TCS systems to lower the cost of CSP and provide dispatchable power generation.^[27] The reaction enthalpy of a chemical reversible gas-solid reaction stores heat in the endothermic reaction path and releases heat in the exothermic path. Solid gas redox reactions of metal oxides in air are suitable candidates for exploiting the accessible high temperatures of CSP. Besides applicable reaction temperature, the metal oxide should feature suffi-

[a] N. C. Preisner, Dr. M. Linder
Thermal Process Technology
DLR, Institute of Engineering Thermodynamics
Linder Höhe, 51147 Köln, Germany
E-mail: Nicole.Preisner@dlr.de

[b] Dr. T. Block
Structural and Functional Ceramics
DLR, Institute of Material Research
Linder Höhe, 51147 Köln, Germany

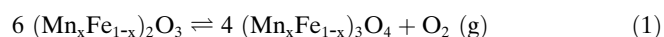
[c] Dr. H. Leion
Chemistry and Chemical Engineering
Chalmers University of Technology
Kemigården 4, Göteborg, Sweden

Supporting information for this article is available on the WWW under <https://doi.org/10.1002/ente.201800211>

cient mechanical strength, fast kinetics, high reaction enthalpy, and cycle stability.

Since oxygen from ambient air can be used as the reaction gas for a thermochemical reaction, no separate gaseous storage is necessary. The concept of two interconnected reactors for continuous charging and discharging is presented by Schrader et al.^[28] with CoO as thermochemical storage material and heat transfer medium. A solar reactor for reduction and an oxidation reactor are combined with cold and hot storage tanks to feed an air Brayton cycle. For this reason, the storage capacity and power are decoupled, allowing the separate adjustment of both power and capacity. In these continuous reactors, it is possible to extract thermochemical and sensible thermal energy and, thus, increase the energy density of metal oxide particles. So far, solar receivers for the reduction of metal oxide particles by direct solar radiation apply rotary kiln,^[29,30] gravity-driven particle receivers,^[31,32] or packed bed reactors.^[33] A fluidized bed reactor^[35] and packed bed reactors^[25,34] were investigated for reactors that are able to oxidize metal oxide particles and extract heat to a working fluid. A further development of the packed bed to a moving bed as a reactor concept for continuous heat extraction combines two main advantages. First, thermochemical as well as sensible heat can be extracted from the metal oxide particles to improve overall efficiency, while a stable temperature of a working fluid is allowed. Second, no moving reactor components at high temperatures need to be handled since particles are transported by gravity in contrast to continuous reactors like rotary kiln or sintering bands.

Manganese-iron oxides have an equilibrium temperature in air atmosphere between 900 °C and 1400 °C, depending on the manganese-to-iron ratio. Thermodynamic investigations of the manganese-iron-oxygen system in air identify the cubic bixbyite phase $[(\text{Fe}^{3+}, \text{Mn}^{3+})_2\text{O}_3]$, and the trigonal hematite phase (Fe_2O_3) at low temperatures and the cubic spinel phase $[(\text{Fe}^{2+}, \text{Mn}^{2+})(\text{Fe}^{3+}, \text{Mn}^{3+})_2\text{O}_4]$, and tetragonal hausmannite phase $[(\text{Mn}^{2+})(\text{Mn}^{3+})_2\text{O}_4]$ at high temperatures as thermodynamically stable phases.^[36–39] The oxides are non-toxic and show acceptable reaction time for oxidation and reduction as well as cycle stability. Several studies have investigated the redox behavior of manganese-iron-oxide systems with different manganese-iron ratios for thermochemical applications.^[22,40–42] Equation (1) presents the global reaction of manganese-iron oxides between bixbyite and spinel, which can be initiated by changing oxygen partial pressure or/and temperature.



A stoichiometric weight change caused by the redox reaction of 3.340 to 3.378 % with the Mn-cation content $(\text{Mn}/(\text{Mn} + \text{Fe})) \times$ between 0 and 1 can theoretically be achieved. However, agglomeration and particle stability problems occur after a number of redox reactions of $(\text{Mn}_{0.75}\text{Fe}_{0.25})_2\text{O}_3$ granules in a packed bed reactor.^[34] Under chemical looping conditions, similar problems with manganese-iron-oxide particles in

a fluidized bed reactor have been reported.^[43] A reactor concept with moving particles, such as a reactor with a moving bed or a fluidized bed, induces even greater stress on the particles than a packed bed. The attrition of particles results in the loss of material when small particles must be removed and a recycling or filtration system becomes necessary. Moreover, decreasing particle size causes higher pressure losses and, thus, lowers the performance of a reactor setup.

Particles undergo several kinds of stress in a reactor, such as chemical, mechanical, and thermal stress. As a consequence, particles may split, become fatigued, fractures may spall, or the surface may be smoothed due to attrition or abrasion, leading to a shift in particle size distribution. Mechanical stress includes particle-wall or particle-particle collision. When the kinetic energy of a collision at high velocity is absorbed, particles may fracture or be abraded. A low velocity collision causes surface abrasion resulting in very fine particles by smoothing the small edges on the particle. Particles endure thermal stress in the form of high heating or cooling rates, temperature gradients inside the particle, or different thermal expansion coefficients of multiphase particles.^[44] Chemical reactions can cause stress when phases with different densities or molar volumes are formed, resulting in intraparticle stresses, e.g. the reduction of Fe_2O_3 caused by the expansion of ferrite oxide crystals.^[45] A change in pore structure may weaken the overall particle,^[46] and the release of gas during a reaction can cause an internal pressure gradient in gas-solid reactions.

The agglomeration tendency of particles is an important criterion for the expected useful lifetime of any thermochemical storage material. Agglomeration can be caused by a temperature exceeding the onset sinter temperature, chemical reactions, or particle-collision-induced melting.^[45,47,48] Since any change in particle size distribution may have a tremendous impact on reactor performance, possibilities to improve the particle stability of chemically reacting Manganese-iron oxides are addressed in this paper.

Particle strength can be improved by adjustments made in the particle preparation, for instance, by choosing sol-gel granulation, spray drying, using precipitation methods, or by adding binders. Coating with a strong porous material can also strengthen particles as well as introducing compressive stresses by rapid heating and cooling of particles to harden the particle surface without sintering or phase changes.^[44]

The fluidized bed concept utilized in CLC can cause the severe attrition of oxygen carrier particles. Thus, in the research field of chemical looping, great effort has been put into improving, measuring, and predicting the strength of metal oxide particles and their agglomeration tendency.^[50] Adding supportive inert material, optimizing the calcination temperature, or choosing an adapted preparation method have shown promising results. Azimi et al.^[51] have investigated the effect of different additives (40 wt.%) to spray-dried $(\text{Mn}_{0.75}\text{Fe}_{0.25})_2\text{O}_3$ particles on mechanical strength and reactivity under chemical-looping conditions. Attrition resistance was found to be substantially improved with the addition of ZrO_2 (monoclinic), depending on the calcination temper-

ature of the particles. For this reason, the use of a rather low calcination temperature is recommended.^[51] A fixed amount of 7 wt.% TiO_2 was added by the authors of^[52] for its reactivity and magnetic properties to manganese-iron oxides with a Mn:Fe ratio between 0 and 1 and under chemical looping conditions. An increase in crushing strength was found compared to particles without the addition of Ti.

Particle stability and the modification of metal oxides have been comprehensively investigated by the chemical-looping research community.^[46,53–55] However, operation conditions and applied reactor concepts differ between chemical-looping and thermochemical storage applications. In CLC, isothermal reaction conditions are mainly applied in O_2 depleted air for the oxidation of metal oxides, and a fuel atmosphere for the reduction of metal oxides.^[2] In contrast, in the thermochemical storage concept, the reduction in O_2 -depleted air and oxidation in air are initiated thermally by exceeding the equilibrium temperature or by changing the partial pressure of O_2 under isothermal conditions.^[34] Particle size may vary depending on the applied reactor concept. For these reasons, it remains uncertain if the findings from particle stability investigations under chemical-looping conditions can be applied to thermochemical storage applications. This paper presents an investigation of the effect of the addition of ZrO_2 , CeO_2 , or TiO_2 to manganese-iron oxide on reactivity, agglomeration, and attrition behavior under the specific conditions relevant for thermochemical storage using a moving bed reactor.

Results and Discussion

Characterisation of the material

A manganese-iron oxide with a Mn/Mn + Fe ratio of 0.7 was chosen as a promising thermochemical storage material due to its suitable redox reaction time and temperature, cycle stability and reaction enthalpy.^[22,41,42] To further improve the mechanical strength of the material, ZrO_2 , CeO_2 , or TiO_2 was added as a support, each equaling 20 wt.% of the particle composition. Detailed composition and material properties are given in Table 1. The composition specifies the weight fraction of raw materials used for producing the particles.

Scanning electron microscopy was used to characterize the microstructures of all untreated samples (Figure 1). Internal imperfections are visible in the polished microsections in the figure. Further investigation with EDX indicated iron-rich, manganese-rich, and additive-rich regions. A bimodal grain distribution with larger Fe-rich regions and smaller Mn-rich regions was identified in the $(\text{Mn}_{0.7}\text{Fe}_{0.3})_2\text{O}_3$ particles. The internal distribution of the additive material seemed to increase in heterogeneity from Zr-cation, Ti-cation, to Ce-cation. Detailed data can be found as supporting information.

Table 1. Composition and bulk density of manganese-iron-oxide materials.

Acronym ^[a]	Molar Composition	Composition of raw materials (wt.%)	Bulk density (kg m^{-3})
Mn70Fe30	$(\text{Mn}_{0.7}\text{Fe}_{0.3})_2\text{O}_3$	69 % Mn_2O_3 31 % Fe_2O_3	1330
Mn70Fe30_Zr20	$(\text{Mn}_{0.7}\text{Fe}_{0.3})_2\text{O}_3/\text{ZrO}_2$	55.2 % Mn_2O_3 24.8 % Fe_2O_3 20 % ZrO_2	1539
Mn70Fe30_Ce20	$(\text{Mn}_{0.7}\text{Fe}_{0.3})_2\text{O}_3/\text{CeO}_2$	55.2 % Mn_2O_3 24.8 % Fe_2O_3 20 % CeO_2	1366
Mn70Fe30_Ti20	$(\text{Mn}_{0.7}\text{Fe}_{0.3})_2\text{O}_3/\text{TiO}_2$	55.2 % Mn_2O_3 24.8 % Fe_2O_3 20 % TiO_2	1193

[a] The acronym describes the molar ratio of Mn and Fe cations and the weight fraction of added ZrO_2 , TiO_2 , or CeO_2 .

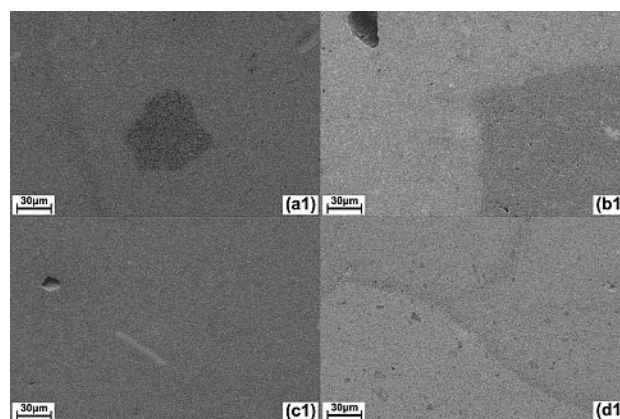


Figure 1. SEM profile image with 5.0 kV acceleration voltage and working distances of 8.0 mm (a, c, d) and 7.9 mm (b) of untreated Mn70Fe30 (a1), Mn70Fe30_Ce20 (b1), Mn70Fe30_Ti20 (c1), and Mn70Fe30_Zr20 (d1).

Effect of additives on energy storage density

A modification with inert additives potentially lowers the total energy density, since inert additives do not contribute to the thermochemical share in energy density. Regarding the sensible thermal energy stored in the particles, a supportive material with high heat capacity should be favored in case of thermochemical energy storage application, whereas a lower heat capacity is beneficial in case of CLC application. Rutile (TiO_2) offers the highest mean heat capacity of $934.04 \text{ J kg}^{-1} \text{ K}^{-1}$ for temperatures between 600 K and 1300 K, followed by ceria (CeO_2) with $603.56 \text{ J kg}^{-1} \text{ K}^{-1}$ and zirconia (ZrO_2) featuring $450.24 \text{ J kg}^{-1} \text{ K}^{-1}$.^[56] However, the bulk density of manganese-iron oxides with the addition of ZrO_2 is slightly higher than with the addition of TiO_2 , which affects the volumetric energy density of the storage material. When inert, the support material does not contribute to the thermochemical share of energy density.

According to reaction equation (1), a stoichiometric mass loss of 3.366 % can be calculated for pure $(\text{Mn}_{0.7}\text{Fe}_{0.3})_2\text{O}_3$. The additive, when behaving inert, reduces the stoichiometric mass loss to 2.693 % for $(\text{Mn}_{0.7}\text{Fe}_{0.3})_2\text{O}_3$ with 20 wt.% of ZrO_2 ,

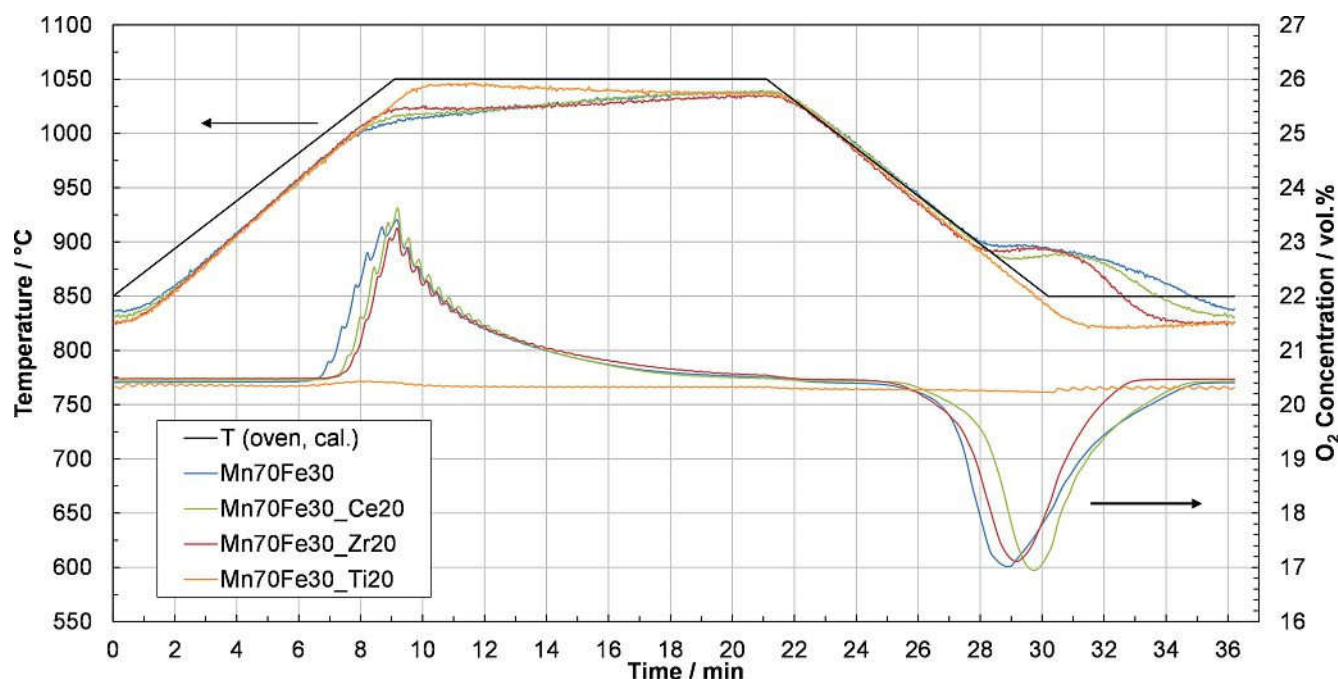


Figure 2. Measured bed temperature and set point temperature of the 25th cycle (upper curves) and O₂ concentration (lower curves) of 25th cycle of thermal cyclization in lab-scale packed bed reactor with pure (Mn_{0.7}Fe_{0.3})₂O₃ or supported with TiO₂, ZrO₂, or CeO₂.

TiO₂, or CeO₂. Thermogravimetric measurements with Mn70Fe30, Mn70Fe30_Zr20, or Mn70Fe30_Ce20 confirmed the stoichiometric mass loss of equation (1) with a deviation of 0.04–0.06 wt.%. Whereas Mn70Fe30_Ti20 showed a higher mass loss during reduction than pure Mn70Fe30, indicating that equation (1) is not the predominant reduction reaction under the given conditions.

Effect of thermal cyclization

The effects of chemical and thermal stress on supported manganese-iron oxide particles were investigated and quantified in the study. The experiments were conducted in a packed bed reactor to inhibit any friction of the material.

The effect of chemical stress on the particle stability and the reactivity of pure manganese-iron oxide and manganese-iron oxide with the addition of CeO₂, ZrO₂, or TiO₂ were investigated with thermal cyclization tests. The reduction and oxidation was initiated by changing the set point temperature of the oven between 850 °C and 1050 °C for 30 cycles.

The ability of manganese-iron oxides with different supporting additives to perform reversible redox reactions in air is illustrated in Figure 2 with the exemplary 25th cycle. An increase in O₂ concentration denotes the reduction to (Mn_{0.7}Fe_{0.3})₃O₄, and a decrease in O₂ concentration denotes the oxidation to (Mn_{0.7}Fe_{0.3})₂O₃ for Mn70Fe30 according to equation (1). The O₂ concentration in the exhaust gas of Mn70Fe30_Ti20 during thermal cyclization indicated no relevant reduction or oxidation of the material, whereas pure (Mn_{0.7}Fe_{0.3})₂O₃ and the samples supported with CeO₂ and

ZrO₂ were reduced and oxidized in air atmosphere. The increase in O₂ concentration up to a peak of around 23.5 % or reduction down to around 17 % was similar for the three remaining compositions, but varied in time and in temperature. The area under the O₂ line correlates to the extent of conversion. During the reduction of the 25th cycle, Mn70Fe30 reached the highest reduction conversion, even though the reactive mass was identical for the three samples. A detailed analysis of the oxidation conversion is given in Figure 3. The endothermic reduction started at around 971 °C, which limited the bed temperature during heating and the subsequent isothermal phase. The initiation temperature of reduction, however, seemed to decrease between Mn70Fe30_Zr20, Mn70Fe30_Ce20 to Mn70Fe30. The exothermic oxidation began slowly at around 966 °C and led to a temperature plateau in the range of 895 °C for Mn70Fe30 and Mn70Fe30_Zr20 and around 889 °C for Mn70Fe30_Ce20 during the cooling phase. The initiation temperatures of reduction and oxidation of Mn70Fe30 and Mn70Fe30_Ce20 were stable during 30 temperature cycles and were in agreement with reported equilibrium temperatures in phase diagrams.^[36,37,39] The initiation temperature of reduction and oxidation of Mn70Fe30_Zr20 showed a slight increase during cyclization from 975 °C to 983 °C in case of reduction and from 960 °C to 972 °C in case of oxidation. The conversion presented in Figure 3 was calculated as oxygen loss in the gas stream due to the oxidation of the particles relative to the stoichiometric oxygen uptake of the active manganese-iron oxide content, for the 2nd and last performed oxidations.

Only 28 cycles could be performed for Mn70Fe30_Zr20 due to practical reasons, while 30 cycles were conducted with

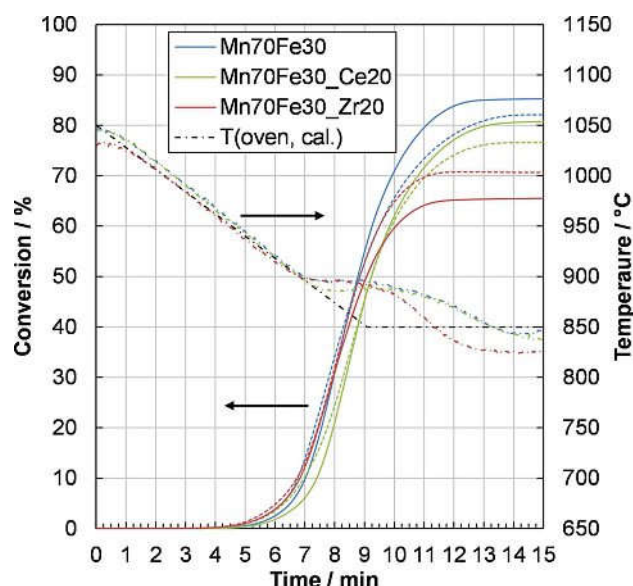


Figure 3. Oxidation conversion of Mn70Fe30 (blue), Mn70Fe30_Ce20 (green), and Mn70Fe30_Zr20 (red), relative to the stoichiometric oxygen uptake of the active manganese-iron oxide content in the sample, during the 2nd (-) and 28th (Mn70Fe30_Zr20) or 30th (--) cycle of thermal cyclization in a packed bed reactor. The bed temperature (•••) is displayed for the 2nd cycle of each composition as well as the set point temperature of the kiln.

the other displayed compositions. Each sample has been cooled to ambient temperature in air between the two displayed cycles, because the cyclization was performed on two consecutive days. The given time started at the end of the isothermal step at 1050°C. No conversion calculations were performed for Mn70Fe30_Ti20 since the O₂ concentration in the exhaust gas indicated only minor reduction and oxidation after one reduction during the first cycle. A detailed depiction of the occurring phases is presented in Figure 8–11. The manganese-iron oxides with the addition of CeO₂ and ZrO₂ showed a lower conversion than Mn70Fe30. While 85.2 % of the pure Mn70Fe30 sample could be oxidized during the 2nd cycle, Mn70Fe30_Ce20 and Mn70Fe30_Zr20 reached a total conversion of 80.8 % and 65.5 %, respectively. The length of the temperature plateaus in Figure 3 reflects the discrepancy between achieved conversion values, and the plateau formation is directly related to the highest oxidation rate. The conversion trend of Mn70Fe30 and Mn70Fe30_Ce20 declined with increasing cyclization number and showed no continuous effect of the prolonged oxidizing conditions while the reactor was cooled to ambient temperature after one day of experiments. In contrast, the cooling-down phase of a Mn70Fe30_Zr20 packed bed significantly improved the conversion of the redox reaction, resulting in an increase in conversion for the 28th cycle of 70.75 %. Furthermore, the reaction time needed to achieve 0.1 % to 50 % conversion increased for Mn70Fe30 and Mn70Fe30_Ce20 from the 2nd to the 30th cycle. Up to this point, Mn70Fe30 and Mn70Fe30_Ce20 seemed to be the most promising candidates as energy storage material with respect to oxidation behavior. It should be noted that the oxidation conversion of Mn70Fe30_Zr20 benefited most of the pro-

longed oxidation during the cooling of the packed bed between day 1 and 2. For this reason, a longer isothermal step may improve the cycle stability.

To eliminate the influence of the experimental conditions on the conversion results, the mass loss during 30 cycles of each material was measured with a simultaneous thermal analyzer. The temperature profile and the gas atmosphere was adjusted according to thermal cyclization conditions. The conversion of the 2nd, 15th, and 30th cycle was normalized with the stoichiometric mass loss (Table 2). After a mass loss of

Table 2. Conversion stability of pure and supported manganese-iron-oxide particles. 30 Cycles were performed with a simultaneous thermal analyzer with conditions similar to thermal cyclization experiments in a packed bed reactor.

Material	Cycle 2 Red.	Ox.	Cycle 15 Red.	Ox.	Cycle 30 Red.	Ox.
Mn70Fe30	92.4 %	91.5 %	92.1 %	91.8 %	92.4 %	91.2 %
Mn70Fe30_Zr20	92.8 %	92.1 %	91.3 %	91.7 %	92.1 %	91.3 %
Mn70Fe30_Ce20	92.1 %	92.1 %	91.7 %	91.4 %	91.4 %	89.9 %

1.40 % during the first reduction of Mn70Fe30_Ti20, only minor mass changes were observed in subsequent cycles. All materials, except Mn70Fe30_Ti20, showed stable conversion rates over 30 cycles with thermal cyclization conditions.

A particle size distribution analysis can reveal the predominant breakage mechanism. Therefore, the distribution before and after a treatment that caused stress to the particles was compared.^[58] In the differential particle size distribution plot (Figure 4), positive weight fractions denote an increase in the weight fraction for the given particle size, whereas a negative value corresponds to a decrease in the weight fraction for the given particle size. All samples were treated in a vibrating machine for 10 minutes to separate the different particle sizes according to the mesh sizes of the sieves.

The particle size distribution of untreated Mn70Fe30_Ce20 is included to illustrate the original particle size distribution of all the tested materials, which showed a very similar distribution. The Mn70Fe30 sample showed a high tendency towards agglomeration as indicated by particle sizes above the original 2–3 mm. In addition, the disintegration mechanism led to the production of fines for Mn70Fe30 after 30 cycles, which is displayed enlarged in the right corner. An image of a Mn70Fe30 agglomerate and Mn70Fe30 fines is presented in Figure 5 and Figure 6, respectively. The bed volume of Mn70Fe30 particles increased by 17 %, which could represent a particle “swelling” and result in an increased amount of particles in the diameter range of 3–4 mm. Wokon et al.^[42] have reported a similar effect for (Mn_{0.75}Fe_{0.25})₂O₃ particles in the size range of 1–3 mm after 100 redox cycles. In addition, Brown et al.^[46] have described an increase in the swelling effect for pure iron oxide particles, when they performed continuing redox reactions between Fe₂O₃ and Fe₃O₄ phase. The authors identified the formation of a porous instead of a lamella magnetite as the crucial point, and this

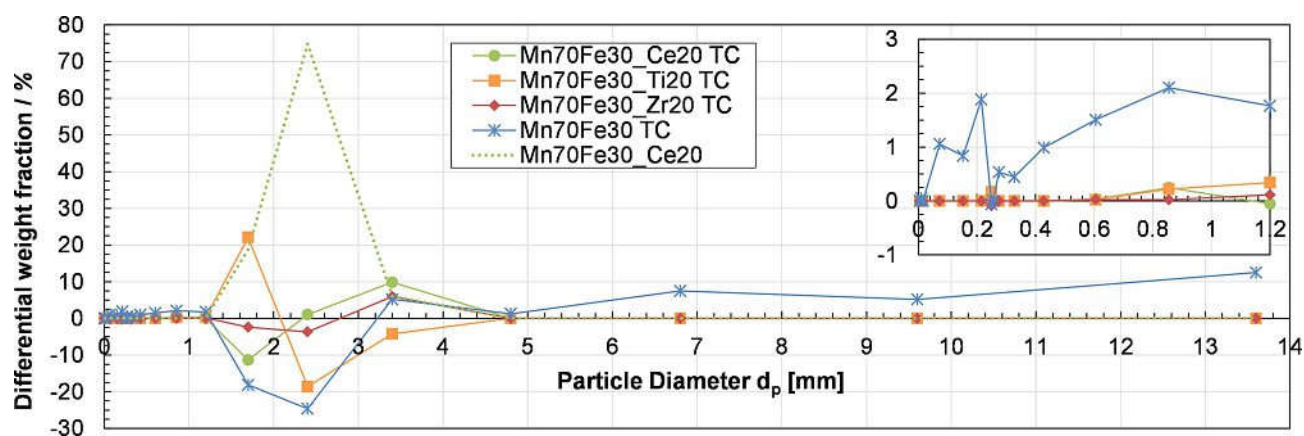


Figure 4. Differential particle size distribution of pure $(\text{Mn}_{0.7}\text{Fe}_{0.3})_2\text{O}_3$ and manganese-iron oxide with supporting additives after 30 cycles of thermal cyclization (TC) in a packed bed reactor compared to untreated particle size distribution with a close up of 0 to 1.2 mm particle size in the upper right corner. The values display the difference between the weight fraction of each measured particle size range before and after particle treatment in a packed bed reactor. The green dotted line symbolizes original particle size distribution before any treatment. The plotted particle size was calculated as arithmetic mean particle size of the sieve sizes.



Figure 5. Mn70Fe30 agglomerate after 30 temperature cycles.



Figure 6. Mn70Fe30 bulk after 30 temperature cycles.

resulted in fragile particles with a tendency towards fragmentation. Carrillo et al.^[41] suspect that sintering processes, or more precisely, a complete morphology change caused by high temperature conditions for the reduction and oxidation of $\text{Mn}_2\text{O}_3/\text{Mn}_3\text{O}_4$ or $(\text{Mn,Fe})_2\text{O}_3/(\text{Mn,Fe})_2\text{O}_3$ systems, are responsible for low re-oxidation rates. Those authors present sintering as a combination of densification and coarsening phenomena. They suggest that the sintering process impedes oxygen diffusion through Mn_3O_4 layers because of reduced active surface or particle aggregation.

In contrast to Mn70Fe30, all supported manganese-iron oxides showed no rise in bed volume height after 30 temperature cycles. All the supportive materials obviously impeded the agglomeration phenomenon to a minimum. Mn70Fe30_Ce20 and Mn70Fe30_Zr20 particles showed a redistribution of particle size from the lower end of original particle size to slightly larger particles. Some particles must have agglom-

erated, since no “swelling” effect could be observed. In contrast, Mn70Fe30_Ti20 particles tended towards breakage instead of disintegration and showed no agglomeration phenomenon.

In order to better understand and support the above findings, a detailed analysis of the morphology of the samples was performed. SEM images showed enlarged grains with irregular morphology in a comparison of the particle surface after thermal cyclization of Mn70Fe30, Mn70Fe30_Ti20, Mn70Fe30_Ce20, and Mn70Fe30_Zr20 (Figure 7) with untreated material.

The addition of ZrO_2 in particular seemed to reduce grain growth on particle surface during thermal cyclization (Figure 7 c1-c2). In a comparison of manganese-iron oxide with the addition of CeO_2 , ZrO_2 , or TiO_2 , Mn70Fe30_Ce20 developed the largest and most irregular surface grains and the most agglomerates, which is in agreement with the agglomeration tendency after redox reactions in air, indicated by the differential particle size distribution (Figures 4 and 12a).

XRD analyses of samples after thermal cyclization (Figures 8–11) suggested that ZrO_2 and CeO_2 are mostly inert additives to $(\text{Mn}_{0.7}\text{Fe}_{0.3})_2\text{O}_3$. This is in agreement with Bhavsar et al.^[48] However, the CeO_2 -supported manganese-iron oxide sample was not completely oxidized after thermal cyclization with subsequent cooling to ambient temperature in air. Furthermore, the TiO_2 -supported manganese-iron oxide sample formed an iron-titanate phase, detected as pseudobrookite (Fe_2TiO_5) with XRD, which also detected bixbyite (Mn_2O_3) and hematite (Fe_2O_3). According to Anovitz et al.,^[62] pseudobrookite is formed from hematite (Fe_2O_3) and rutile (TiO_2) and remains stable above 585°C , which explains the poor reactivity of this sample (see Figure 2). Therefore, pseudobrookite could have been already formed during the preparation process of the Mn70Fe30_Ti20 particles.

Thermal cyclization experiments focused mainly on chemical stress, but it must be noted that by initiating the redox

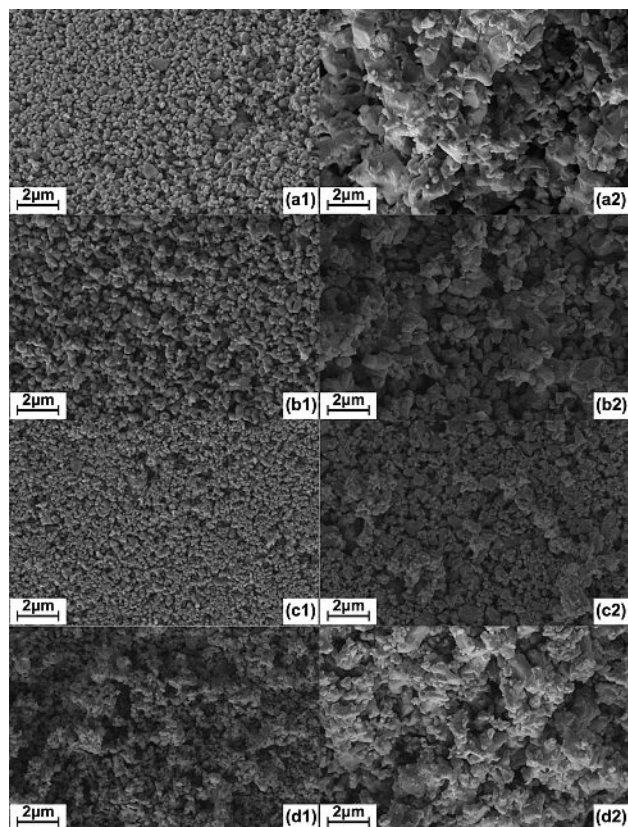


Figure 7. SEM images with 5.0 kV acceleration voltage and working distances 8.0 mm (a1, b1, b2, c1, c2 and d1, d2) and 7.9 mm (a2) of Mn70Fe30 (a1, a2), Mn70Fe30-Ti20 (b1, b2), Mn70Fe30-Zr20 (c1, c2) and Mn70Fe30-Ce20 (d1, d2) particle surface: untreated (1) and after thermal cyclization (2)

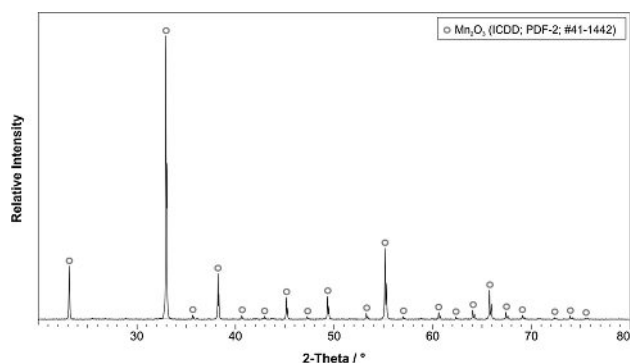


Figure 8. XRD pattern of the manganese-iron-oxide sample after thermal cyclization. Mn_2O_3 (space group: $la3$) can be detected. This pattern overlaps the Fe_2O_3 pattern (ICDD; PDF-2; #39-0238) (space group: $la3$), so that pure Mn_2O_3 , pure Fe_2O_3 , or $(\text{Mn,Fe})_2\text{O}_3$ cannot be distinguished.

reaction over temperature variation, instead of oxygen pressure variation, chemical and thermal stresses cannot be separated completely. For this reason, additional “temperature shock” experiments were performed.

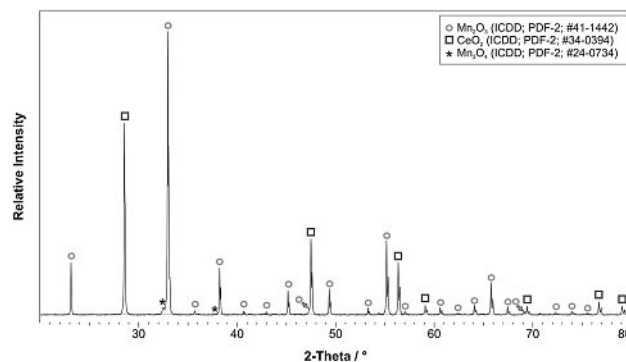


Figure 9. XRD pattern of the manganese-iron-oxide sample with the addition of CeO_2 after thermal cyclization. Mn_2O_3 (space group: $la3$), CeO_2 (space group: $\text{Fm}3\text{m}$), and Mn_2O_4 (space group: $I41/amd$) can be detected. As described in Figure 8 overlap with the Fe_2O_3 pattern (ICDD; PDF-2; #39-0238) (space group: $la3$) is possible, so that pure Mn_2O_3 , pure Fe_2O_3 , or $(\text{Mn,Fe})_2\text{O}_3$ cannot be distinguished.

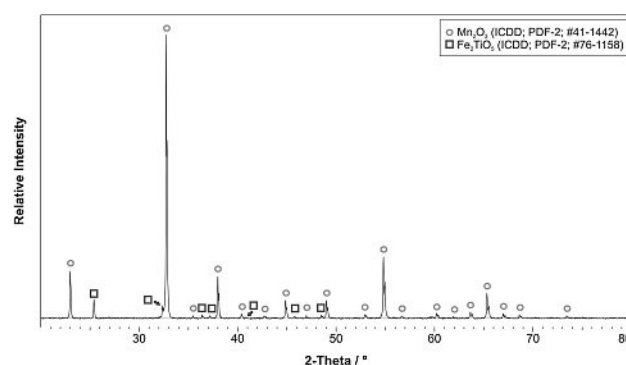


Figure 10. XRD pattern of the manganese-iron-oxide sample with the addition of TiO_2 after thermal cyclization. Mn_2O_3 (space group: $la3$) and Fe_2TiO_5 (space group: Cmcm) can be detected. As described in Figure 8 overlap with the Fe_2O_3 pattern (ICDD; PDF-2; #39-0238) (space group: $la3$) is possible, so that pure Mn_2O_3 , pure Fe_2O_3 , or a $(\text{Mn,Fe})_2\text{O}_3$ cannot be distinguished.

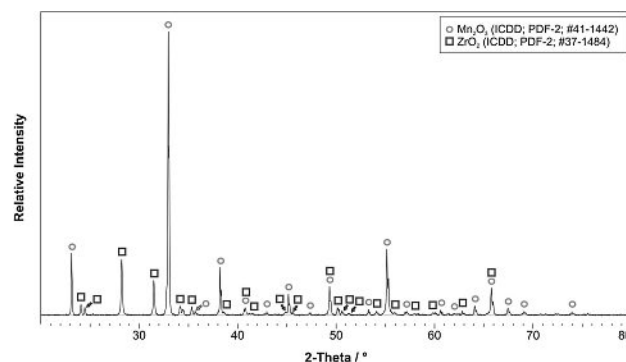


Figure 11. XRD pattern of the manganese-iron-oxide sample with the addition of ZrO_2 after 30 temperature cycles. Mn_2O_3 (space group: $la3$) and ZrO_2 (space group: $\text{P}21/a$) can be detected. As described in Figure 8 overlap with the Fe_2O_3 pattern (ICDD; PDF-2; #39-0238) (space group: $la3$) is possible, so that pure Mn_2O_3 , pure Fe_2O_3 , or a $(\text{Mn,Fe})_2\text{O}_3$ cannot be distinguished.

Effect of temperature shocks

The effect of thermal strain on Mn70Fe30, Mn70Fe30_Ce20, and Mn70Fe30_Zr20 samples was investigated by applying high cooling rates to the packed bed. Fifteen subsequent cycles in air and in N₂ were performed. Since Mn70Fe30_Ti20 showed no stable redox reaction in the previous cyclization test, it was excluded from further examination. A nitrogen atmosphere prohibits the re-oxidation of previously reduced manganese-iron oxide particles, whereas an air atmosphere allows a re-oxidation reaction. It must be noted that due to the fast average cooling rate of $110 \pm 4 \text{ K min}^{-1}$, a complete conversion was not reached in air. In general, conversion decreased with cycle number for all samples. While a conversion of 77.7 % for reduction and 76.9 % for oxidation of Mn70Fe30 was achieved in the first cycle, the conversion dropped to 26.9 % for reduction and 31.1 % for oxidation in the 15th cycle. Mn70Fe30_Ce20 and Mn70Fe30_Zr20 indicated a similar behavior with a decrease of oxidation conversion of 64.4 % to 21.2 % and 48.8 % to 5.1 % respectively.

However, a direct comparison with the experiments performed in N₂ showed clear effects that could be ascribed to the chemical reaction. The differential particle size distribution after a temperature shock test in air atmosphere showed an agglomeration of Mn70Fe30_Ce20 and, especially, Mn70Fe30 particles (Figure 12a). In contrast, thermal strain seemed to provoke splitting of Mn70Fe30_Zr20 particles to nearly half the original diameter.

The particle size distribution for Mn70Fe30_Ce20 and Mn70Fe30 showed no direct splitting effect when the air atmosphere allowed a redox reaction. In contrast, the temperature shock test in the nitrogen atmosphere (Figure 12b) did not initiate any agglomeration of any of the tested compositions. This means that the agglomeration of (Mn_{0.7}Fe_{0.3})₂O₃/(Mn_{0.7}Fe_{0.3})₃O₄-based compositions is strongly related to the phase change caused by the redox reaction in the oxygen atmosphere and was not influenced by heating or cooling rates up to 110 K min^{-1} . An apparent higher splitting of the Mn70Fe30_Zr20 sample in the nitrogen atmosphere than in the air atmosphere could be caused by a stronger reduced phase or experimental variance in sieving due to a rather low mass of 10 to 12 g of sample. However, Mn70Fe30_Ce20 and Mn70Fe30_Zr20 developed higher particle splitting due to thermal stress than Mn70Fe30 particles (Figure 12b). It can be speculated that there could be a superposition of splitting and subsequent agglomeration process for Mn70Fe30_Ce20 because Mn70Fe30_Ce20 indicated minor particle splitting during the temperature shock test in the nitrogen atmosphere but no particle splitting when the air atmosphere allowed for a redox reaction. In the end, the chemical reaction seemed to provoke the agglomeration of unsupported manganese-iron-oxide, and thermal gradients induced the splitting of ZrO₂-supported manganese-iron-oxide particles.

The morphology on the particle surface especially of Mn70Fe30 and Mn70Fe30O_Ce20 changed with the 15 temperature shocks in air or nitrogen (Figure 13 a1–b2). An EDX analysis of Mn70Fe30 after 15 temperature shocks in air

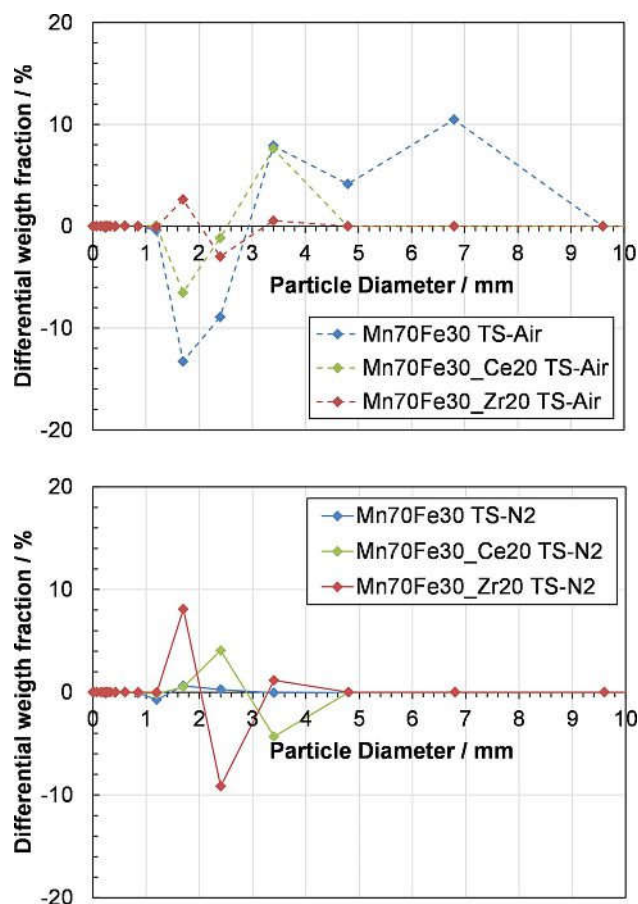


Figure 12. Differential particle size distribution after 15 temperature shocks in air (TS-Air) (a) and nitrogen atmospheres (TS-N2) (b) with Mn70Fe30, Mn70Fe30_Ce20, and Mn70Fe30_Zr20 in a packed bed reactor.

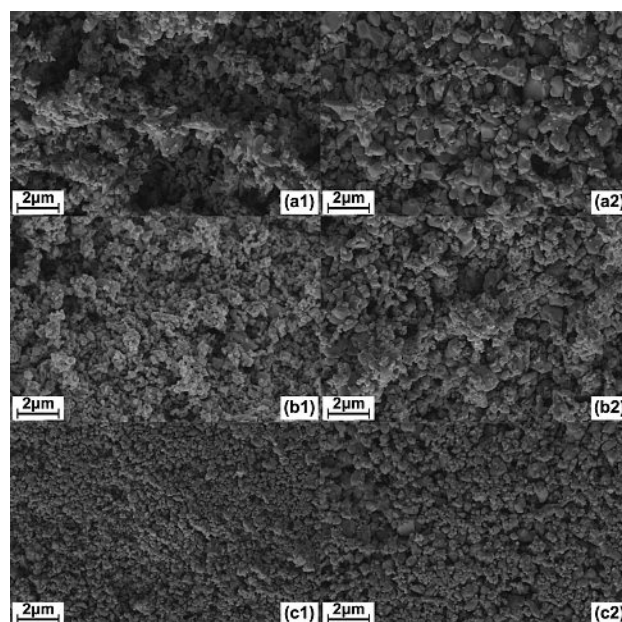


Figure 13. SEM images with 5.0 kV acceleration voltage and working distances 8.0 mm (a1, a2, b1, c1, c2) and 8.1 mm (b2) of Mn70Fe30 (a1, a2), Mn70Fe30_Ce20 (b1, b2) and Mn70Fe30_Zr20 (c1, c2) particle surface: after 15 temperature shock in air (1) or in nitrogen (2)

indicated Mn-rich areas as well as areas with an equal distribution of Mn and Fe cations. Whereas an even cation distribution was detected at the EDX measuring points of Mn70Fe30 after 15 temperature shocks in nitrogen. EDX analysis of Mn70Fe30_Zr20 after the temperature shock test in nitrogen revealed an irregular distribution of Mn, Fe, and Zr cations at the measuring points, whereas the EDX measuring points indicated an equal cation distribution in Mn70Fe30_Zr20 after the temperature shock test in air. However, optically, the surface morphology of Mn70Fe30_Zr20 seems to be the most stable one compared to the other compositions after all experiments (Figure 7 c1–c2 and Figure 13 c1–c2). Detailed EDX data can be found as supporting information.

Particle stability investigation

An attrition jet cup was utilized to estimate the tendency towards abrasion of all four compositions in untreated form and after the experiments above. The device was designed for quick screening tests with a low sample weight of 5 g. The mechanical stress in this attrition jet cup is much greater than the stress found under moving bed conditions but may give an indication of the mechanical properties of the sample. The particle size distribution before and after an attrition rig test showed, that the test rig caused both abrasion and fragmentation. Previous examinations of oxygen carriers in the attrition jet cup indicated that the fine production follows either a linear trend over time or a logarithmic trend with a stabilized attrition rate after around 30 min.^[54] Therefore, a total attrition A_{tot} (eq. 2 in Experimental Section) and the attrition rate A_i (eq. 3 in Experimental Section) are used to describe the attrition behavior. The attrition rate corresponds to the slope of the attrition curve over time between 30 min and 1 h operation. The total attrition A_{tot} and the attrition rate A_i in Figure 14 clearly demonstrate the improved attrition behavior of processed material with the addition of ZrO₂ and CeO₂.

Mn70Fe30_Zr20 promised high particle stability. In comparison to untreated particles, thermal stress, induced with temperature shock test in air or nitrogen, had only a minor effect on particle stability according to the attrition test

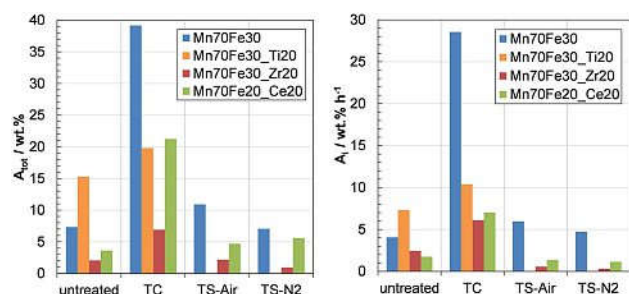


Figure 14. The total attrition (a) and the slope of the attrition curve of the last 30 min (b) of 1 h operation in the attrition jet cup of untreated particles and processed in thermal cyclization (TC) or temperature shock (TS) in air or nitrogen.

method. Fifteen temperature shocks even improved the attrition resistance of Mn70Fe30_Zr20 (Figure 14b). In contrast, 30 temperature cycles increased the total attrition and attrition slope of all material compositions, especially of the unsupported manganese-iron oxide samples. Again, ZrO₂ was found to be the most promising supportive material regarding attrition resistance. However, the attrition rate after thermal cyclization tests with Mn70Fe30_Ce20 is in the range of the Mn70Fe30_Zr20 sample (Figure 14b). In ceramic research, ZrO₂ is known to significantly improve the toughness of alumina due to its high fracture toughness, which describes the resistance of a material to the propagation of preexisting flaws.^[60,61]

The attrition values over time are displayed in Figure 15 with silica sand as a reference material. The Mn70Fe30 sample indicates a linear attrition rate, while the logarithmic attrition curves of Mn70Fe30_Ce20 and Mn70Fe30_Ti20 reach a stable but high level in the figure.

The strong agglomeration tendency and low particle stability (abrasion and disintegration) of Mn70Fe30, which is mainly caused by the chemical stress, can be ameliorated by supporting the manganese-iron oxide with ZrO₂ or CeO₂. From a technical point of view, the choice of modified material depends mainly on the mechanical and thermal stress the particles will experience in the chosen reactor and process concept. In applied reactor concepts, which cause high mechanical stress, e.g. a fluidized bed reactor, Mn70Fe30_Zr20 is the favored composition of the investigated materials in this paper. The attrition test and the 30 temperature cycles proved strong particle stability. However, in comparison to the other compositions, Mn70Fe30_Zr20 indicated a tendency to particle splitting when high temperature gradients occurred. Considering reactor or process concepts with lower attrition risk, e.g. a packed bed, Mn70Fe30_Ce20 showed

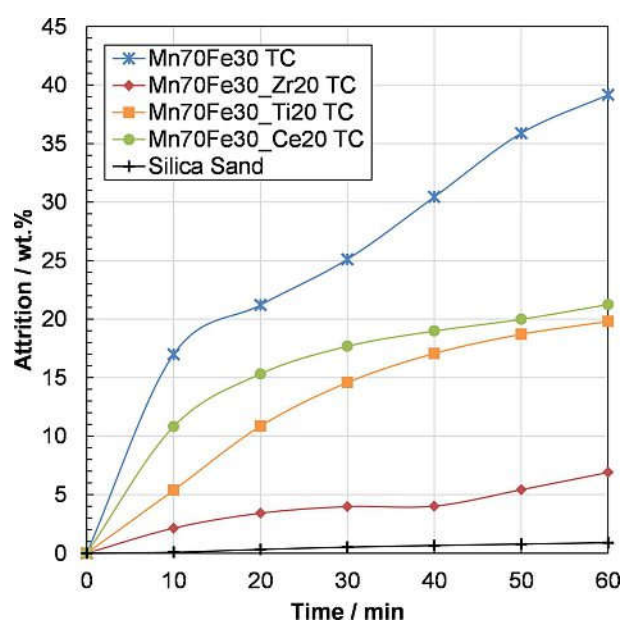


Figure 15. Attrition test of manganese-iron-oxide samples after thermal cyclization. Silica sand is the reference.

advantages over Mn₇₀Fe₃₀_Zr₂₀ particles since it reached the highest oxidation conversion of all the modified particles. Even though Mn₇₀Fe₃₀_Ce₂₀ shows the highest attrition in total numbers for the supported manganese-iron oxides, the slope of the attrition curve (tendency for stabilization) is similar to the results found using Mn₇₀Fe₃₀_Zr₂₀ and a major improvement over Mn₇₀Fe₃₀ particles. In conclusion, supporting Mn₇₀Fe₃₀ with ZrO₂ or CeO₂ promises a prolonged mechanical particle lifetime. However, it must be noted that the production process influences the overall stability behavior of the particles. In future research, an optimal ratio of active manganese-iron-oxide particles to inert ZrO₂ or CeO₂ content will be addressed in terms of particle stability, agglomeration tendency, and reaction conversion.

Conclusions

The reactivity and particle stability of (Mn_{0.7}Fe_{0.3})₂O₃ as an active material supported by 20 wt.% of either CeO₂, ZrO₂, or TiO₂ was tested in a packed bed reactor and with an attrition test rig. From a technical engineering standpoint, the following conclusions can be drawn:

- Mn–Fe oxides are very well suited as thermochemical storage material and oxygen carrier material for chemical-looping combustion.
- Pure (Mn_{0.7}Fe_{0.3})₂O₃ showed the highest reactivity and redox conversion. However, it also showed a great tendency towards agglomeration and low particle stability, which reduces the expected lifetime of the particle. Therefore, a modification of this material is mandatory, despite the drawback of reduced energy density.
- The addition of TiO₂ led to a deactivation of the manganese-iron oxide by forming pseudobrookite.
- Pure (Mn_{0.7}Fe_{0.3})₂O₃ and (Mn_{0.7}Fe_{0.3})₂O₃ supported with CeO₂ or ZrO₂ showed sufficient cycle stability. The reaction rate was faster with the addition of CeO₂ than with ZrO₂ under the experimental conditions, but was still slower than with pure (Mn_{0.7}Fe_{0.3})₂O₃. Consequently, the operational conditions must be adjusted (e.g. a longer reaction time) to avoid incomplete conversion.
- All investigated additives hindered or clearly decreased the agglomeration and improved the particle strength of manganese-iron-oxide particles. Especially ZrO₂ promises a higher resistance towards attrition. A variation of the CeO₂ or ZrO₂ content should be addressed in future research to optimize the particle from the attrition, agglomeration, and reaction rate standpoints for use as thermochemical storage material or oxygen carrier.

Experimental Section

Materials preparation

The Flemish Institute for Technological Research (VITO) in Belgium produced the particles with a build-up granulation

technique by mixing the raw materials Mn₃O₄ (Chemalloy, Trimanox), Fe₂O₃ (Alfa Aesar, 99 %) and one of the supports TiO₂ (Venator, Hombikat™ M211), CeO₂ (American Elements, 99 %) or ZrO₂ (Saint Gobain, 99.9 % ZrO₂ + HfO₂). A pretreatment in air at 800 °C for 10 h allowed Mn₃O₄ and Fe₂O₃ to change into the bixbyite (Mn,Fe)₂O₃ phase. After granulation, the particles were sieved to a size between 2 and 3 mm.

Materials characterization

The weight loss due to reduction was measured with a simultaneous thermal analyzer from Netzsch (STA 449 F3 Jupiter®) to confirm equation (1). Two particles with a total mass of 30 mg were oxidized at 850 °C for 5 h in a Pt/Rh crucible without a cap in an atmosphere containing 20 % oxygen (Linde, 99.995 %) and 80 % nitrogen (Linde, 99.999 %). The reduction was initiated by increasing the temperature with a heating rate of 20 K min^{−1} up to 1050 °C in a nitrogen atmosphere and maintaining the temperature for 5 h. A total gas flow of 100 ml min^{−1} was kept constant for the entire test.

An analysis of crystalline phases of manganese-iron-oxide particles was performed with an X-ray diffractometer (Bruker D8 Advance with Cu-Kα_{1,2} radiation). Scanning electron microscopy (Zeiss Ultra 55) gave information about the shape and morphology of the particles and their polished microsection in combination with energy dispersive X-ray point measurements (Oxford Inca Penta FETX3). EDX measurements were performed with the secondary electron detector at a working distance of 8 mm with accelerating voltage of 15.0 kV and are listed as supporting information. Oxygen has been detected with EDX but is not listed in the supporting information, due to inaccuracy of the EDX measuring method in case of oxygen.

The bulk density was measured by filling and weighing a 50 ml glass cylinder with 2–3 mm particles.

A customized jet cup is available at Chalmers University of Technology in Gothenburg, Sweden, to evaluate the attrition resistance of the oxygen carriers used for chemical looping combustion. A detailed description of the attrition rig setup can be found in.^[54] A sample mass of 5 g was fit into an attrition cup and was fluidized with a moisturized air flow entering the cup through a nozzle. The particles were fluidized into a settling chamber above the cup. A minimal gas flow of 16 Nl min^{−1} carried fines with a diameter below 10 μm through the settling chamber to a particle filter at the top of the chamber, since the terminal velocity of the densest particles equals the gas velocity in the widest part of the settling chamber. The change of filter weight at the gas exit corresponded to the fine production during the measuring time. The total fine production A_{tot} caused by attrition for a measuring period of 1 h was calculated according to equation (2).

$$A_{\text{tot}} = 100 \cdot \frac{m_{f,1h} - m_{f,\text{start}}}{m_s} \quad (\text{wt.}\%) \quad (2)$$

The attrition rate describes the trend of the attrition curve between 30 min and 1 h operation and is calculated according to equation (3).

$$A_i = 100 \cdot \frac{60}{30} \cdot \frac{m_{f,1h} - m_{f,30\text{ min}}}{m_s} \quad (\text{wt.}\% \text{ h}^{-1}) \quad (3)$$

In equations (2) and (3), m_s is the sample weight placed in the cup and $m_{f,t}$ equals the filter weight for a given operation time t .

Experiments in a packed bed reactor

Thermal cyclization tests and temperature shock tests were performed in a packed bed reactor. Particles were placed on a porous quartz plate at the bottom of the reactor (Figure 16). A detailed description of the reactor setup can be found in.^[51]

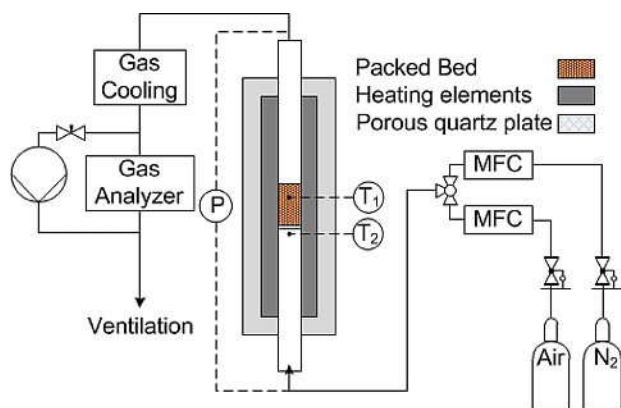


Figure 16. Schematic setup of the packed bed reactor.

The set temperature for the oven was controlled by two thermocouples (Pentronic CrAl/NiAl with inconel-600), each enclosed in a quartz thermowell. One was placed 25 mm above the quartz plate (T_1), and one was placed 5 mm below the plate (T_2). The bed height always exceeded 25 mm and thermocouple T_1 was employed to determine the bed temperature. The reactor could be used as a packed bed or fluidized bed depending on gas velocity. A gas flow of 3 Nl min^{-1} was chosen for all experiments, which resulted in a packed bed operation since the flow was well below the minimum fluidization velocity.

Thermal cyclization was conducted by varying the temperature with a heating rate of 20 K min^{-1} between 850°C for oxidation and 1050°C for reduction in the packed bed reactor. The redox reaction was initiated by changing the temperature. An isothermal step followed each heating and cooling phase for 12 min at 1050°C and for 6 min at 850°C . 30 redox cycles were performed with a mass of 21 g manganese-iron oxide material or 26 g supported manganese-iron oxide material to compensate for the possibly inert additive. The thermal cyclization experiments were executed on two consecutive days, and the packed bed reactor was cooled to ambient temperature in air at the end of the first day.

The fast cooling rates for the temperature shock tests were achieved by opening the oven circa 4 cm to permit effective cooling rates of $110 \pm 4 \text{ K min}^{-1}$. A sample of 10 g manganese-iron-oxide particles or 12 g manganese-iron-oxide with an additive was placed on the quartz plate for temperature shock test. The temperature shock tests were performed 15 times in air for an oxidizing environment and 15 times in a pure nitrogen atmosphere for a reducing environment.

Acknowledgements

The authors acknowledge the work of the late Dongmei Zhao (deceased Dec. 18, 2016). At the time of her death, she was

deeply involved in this research and made many important contributions. Financial support was provided by DLR internal funding and ÅForsk.

Conflict of interest

The authors declare no conflict of interest.

Keywords: Manganese · Iron · Redox chemistry · Thermochemistry · Particle stability

- [1] A. Lyngfelt, B. Leckner, T. Mattisson, *Chem. Eng. Sci.* **2001**, 56, 3101–3113
- [2] T. Mattisson, A. Lyngfelt, H. Leion, *Int. J. Greenhouse Gas Control* **2009**, 3, 11–19
- [3] A. Abad, I. Adánez-Rubio, P. Gayán, F. García-Labiano, L. F. de Diego, J. Adánez, *Int. J. Greenhouse Gas Control* **2002**, 6, 189–200
- [4] L. Xu, H. Sun, Z. Li, N. Cai, *Appl. Energy* **2016**, 162, 940–947
- [5] A. Lyngfelt, C. Linderholm, *Energy Procedia* **2014**, 63, 98–112
- [6] J. Ströhle, M. Orth, B. Epple, *Appl. Energy* **2015**, 157, 288–294
- [7] M. Arjmand, A. Hedayati, A.-M. Azad, H. Leion, M. Rydén, T. Mattisson, *Energy Fuels* **2013**, 27, 4097–4107
- [8] N. M. Pour, G. Azimi, H. Leion, M. Rydén, T. Mattisson, A. Lyngfelt, *Energy Technol.* **2014**, 2, 469–479
- [9] M. Arjmand, H. Leion, A. Lyngfelt, T. Mattisson, *Int. J. Greenhouse Gas Control* **2012**, 8, 56–60
- [10] A. Steinfeld, *Sol. Energy* **2005**, 78, 603–615
- [11] D. Marxer, P. Furler, M. Takacs, A. Steinfeld, *Energy Environ. Sci.* **2017**, 10, 1142–1149
- [12] L. O. Schunk, P. Haeberling, S. Wepf, D. Willemin, A. Meier, A. Steinfeld, *J. Sol. Energy Eng.* **2008**, 130, 021009
- [13] N. Gokon, T. Mataga, N. Kondo, T. Kodama, *Int. J. Hydrogen Energy* **2011**, 36, 4757–4767
- [14] S. Abanades, P. Charvin, G. Flamant, *Chem. Eng. Sci.* **2007**, 62, 6323–6333
- [15] R. B. Diver, J. E. Miller, M. D. Allendorf, N. P. Siegel, R. E. Hogan, *J. Sol. Energy Eng.* **2008**, 130, 041001–041001-8
- [16] I. Ermanoski, N. P. Siegel, E. B. Stechel, *J. Sol. Energy Eng.* **2013**, 135, 031002–031002-10
- [17] E. Koepf, S. G. Advani, A. Steinfeld, A. K. Prasad, *Int. J. Hydrogen Energy* **2012**, 37, 16871–16887
- [18] P. Lichty, X. Liang, C. Muhich, B. Evanko, C. Bingham, A. W. Weimer, *Int. J. Hydrogen Energy* **2012**, 37, 16888–16894
- [19] L. J. Venstrom, R. M. De Smith, Y. Hao, S. M. Haile, J. H. Davidson, *Energy Fuels* **2014**, 28, 2732–2742
- [20] S. Abanades, H. I. Villafan-Vidales, *Chem. Eng. J.* **2011**, 175, 368–375
- [21] C. Agrafiotis, M. Roeb, M. Schmücker, C. Sattler, *Sol. Energy* **2014**, 102, 189–211.
- [22] T. Block, M. Schmücker, *Sol. Energy* **2016**, 126, 195–207
- [23] A. J. Carrillo, J. Moya, A. Bayón, P. Jana, V. a. de la Peña O'Shea, M. Romero, J. Gonzalez-Aguilar, D. P. Serrano, P. Pizarro, J. M. Coronado, *Sol. Energy Mater. Sol. Cells* **2014**, 123, 47–57
- [24] W. E. Wentworth, E. Chen, *Sol. Energy* **1976**, 18, 205–214.
- [25] C. Prieto, P. Cooper, A. I. Fernández, *Renewable Sustainable Energy Rev.* **2016**, 60, 909–929
- [26] H. Zhang, J. Baeyens, G. Cáceres, J. Degève, Y. Lv, *Prog. Energy Combust. Sci.* **2016**, 53, 1–40
- [27] M. Romero, A. Steinfeld, *Energy Environ. Sci.* **2012**, 5, 9234–9245
- [28] A. J. Schrader, A. P. Muroyama, P. G. Loutzenhiser, *Sol. Energy* **2015**, 118, 485–495
- [29] E. Alonso, C. Pérez-Rábago, J. Licurgo, E. Fuentealba, C. A. Estrada, *Sol. Energy* **2015**, 115, 297–305
- [30] M. Neises, S. Tescari, L. de Oliveira, M. Roeb, C. Sattler, B. Wong, *Sol. Energy* **2012**, 86, 3040–3048
- [31] A. S. Oles, G. S. Jackson, *Sol. Energy* **2015**, 122, 126–147

- [32] A. J. Schrader, G. De Dominicis, G. L. Schieber, P. G. Loutzenhiser, *Sol. Energy* **2017**, *150*, 584–595
- [33] E. Alonso, F. Gomez-Garcia, J. Gozalez-Aguilar, M. Romero, *Proceedings of the SolarPACES Conference*, Spain **2011**, 20–23.
- [34] M. Wokon, A. Kohzer, M. Linder, *Sol. Energy* **2017**, *153*, 200–214
- [35] S. Álvarez de Miguel, J. Gonzalez-Aguilar, M. Romero, *Energy Procedia* **2014**, *49*, 676–683
- [36] J. V. Crum, B. J. Riley, J. D. Vienna, *J. Am. Ceram. Soc.* **2009**, *92*, 2378–2384
- [37] L. Kjellqvist, M. Selleby, *J. Phase Equilib. Diffus.* **2010**, *31*, 113–134
- [38] A. Muan, S. Sōmiya, *Am. J. Sci.* **1962**, *260*, 230–240
- [39] D. G. Wickham, *J. Inorg. Nucl. Chem.* **1969**, *31*, 313–320
- [40] L. André, S. Abanades, L. Cassayre, *J. Solid State Chem.* **2017**, *253*, 5–14
- [41] A. Carrillo, D. P. Serrano, P. Pizarro, J. M. Coronado, *ChemSusChem* **2015**, *8*, 1947–1954
- [42] M. Wokon, T. Block, S. Nicolai, M. Linder, M. Schmücker, *Sol. Energy* **2017**, *153*, 471–485
- [43] G. Azimi, H. Leion, M. Ryden, T. Mattisson, A. Lyngfelt, *Energy Fuels* **2013**, *27*, 367–377
- [44] C. H. Bartholomew, *Appl. Catal. A* **2001**, *212*, 17–60
- [45] Y. Zhong, Z. Wang, Z. Guo, Q. Tang, *Powder Technol.* **2014**, *256*, 13–19
- [46] T. A. Brown, F. Scala, S. A. Scott, J. S. Dennis, P. Salatino, *Chem. Eng. Sci.* **2012**, *71*, 449–467
- [47] C. R. Bemrose, J. Bridgwater, *Powder Technol.* **1987**, *49*, 97–126
- [48] S. Bhavsar, B. Tackett, G. Veser, *Fuel* **2014**, *136*, 268–279
- [49] A. Khadilkar, P. L. Rozelle, S. V. Pisupati, *Powder Technol.* **2014**, *264*, 216–228
- [50] Y. De Vos, M. Jacobs, P. Van Der Voort, I. Van Driessche, F. Snijders, A. Verberckmoes, *Chem. Eng. J.* **2017**, *309*, 824–839
- [51] G. Azimi, H. Leion, T. Mattisson, M. Ryden, F. Snijders, A. Lyngfelt, *Ind. Eng. Chem. Res.* **2014**, *53*, 10358–10365
- [52] M. Abián, A. Abad, M. T. Izquierdo, P. Gayán, L. F. de Diego, F. García-Labiano, J. Adánez, *Fuel* **2017**, *195*, 38–48
- [53] M. Jacobs, J. Van Noyen, Y. Larring, M. McCann, M. Pishahang, S. Amini, M. Ortiz, F. Galluci, M. V. Sint-Annaland, D. Tournigant, E. Louradour, F. Snijders, *Appl. Energy* **2015**, *157*, 374–381
- [54] M. Rydén, P. Moldenhauer, S. Lindqvist, T. Mattisson, A. Lyngfelt, *Powder Technol.* **2014**, *256*, 75–86
- [55] A. Tilland, J. Prieto, D. Petitjean, E. Schaer, *Chem. Eng. J.* **2016**, *302*, 619–632
- [56] I. Barin in *Thermochemical data of pure substances*, Vol. 3 (Eds.: K. Sora, J. Gardiner), VCH Verlagsgesellschaft mbH, Weinheim, **1995**.
- [57] A. Cabello, P. Gayán, F. García-Labiano, L. F. de Diego, A. Abad, J. Adánez, *Fuel Process. Technol.* **2016**, *148*, 188–197
- [58] F. Scala, F. Montagnaro, P. Salatino, *Energy Fuels* **2007**, *21*, 2566–2572
- [59] B. Amblard, S. Bertholin, C. Bobin, T. Gauthier, *Powder Technol.* **2015**, *274*, 455–465
- [60] N. Claussen, *J. Am. Ceram. Soc.* **1976**, *59*, 49–51
- [61] S. Hori, M. Yoshimura, S. Sōmiya, *J. Mater. Sci. Lett.* **1985**, *4*, 413–416
- [62] L. M. Anovitz, A. H. Treiman, E. J. Essene, B. S. Hemingway, E. F. Westrum Jr., V. J. Wall, R. Burriel, S. R. Bohlen in *The Heat-capacity of ilmenite and phase equilibria in the system Fe-Ti-O*, *Geochimica et Cosmochimica Acta* **49**, Pergamon Press Ltd., **1985**, pp. 2027–2040.

Manuscript received: March 12, 2018

Revised manuscript received: April 24, 2018


Accepted manuscript online: April 25, 2018

Version of record online: October 1, 2018

2.3 Paper II

Article

Numerical Investigations of a Counter-Current Moving Bed Reactor for Thermochemical Energy Storage at High Temperatures

Nicole Carina Preisner ^{1,*} , Inga Bürger ², Michael Wokon ¹ and Marc Linder ²¹ Institute of Engineering Thermodynamics, DLR, Linder Höhe, 51147 Köln, Germany² Institute of Engineering Thermodynamics, DLR, Pfaffenwaldring 38-40, 70569 Stuttgart, Germany

* Correspondence: nicole.preisner@dlr.de

Received: 27 January 2020; Accepted: 5 February 2020; Published: 10 February 2020



Abstract: High temperature storage is a key factor for compensating the fluctuating energy supply of solar thermal power plants, and thus enables renewable base load power. In thermochemical energy storage, the thermal energy is stored as the reaction enthalpy of a chemically reversible gas-solid reaction. Metal oxides are suitable candidates for thermochemical energy storage for solar thermal power plants, due to their high reaction temperatures and use of oxygen as a gaseous reaction partner. However, it is crucial to extract both sensible and thermochemical energy at these elevated temperatures to boost the overall system efficiency. Therefore, this study focuses on the combined extraction of thermochemical and sensible energy from a metal oxide and its effects on thermal power and energy density during discharging. A counter-current moving bed, based on manganese-iron-oxide, was investigated with a transient, one-dimensional model using the finite element method. A nearly isothermal temperature distribution along the bed height was formed, as long as the gas flow did not exceed a tipping point. A maximal energy density of 933 kJ/kg was achieved, when $(\text{Mn,Fe})_3\text{O}_4$ was oxidized and cooled from 1050 °C to 300 °C. However, reaction kinetics can limit the thermal power and energy density. To avoid this drawback, a moving bed reactor based on the investigated manganese-iron oxide should combine direct and indirect heat transfer to overcome kinetic limitations.

Keywords: moving bed; thermochemical energy storage; redox reaction

1. Introduction

High temperature thermal energy storage is one key factor for further proliferation of concentrated solar power (CSP) plants. The integration allows a plant to decouple energy supply from energy demand, e.g., for cloudy days or during the night. Thus, CSP coupled with thermal energy storage is able to provide base load electricity, making it a renewable alternative for fossil fuel power plants. Thermochemical energy storage is a promising option for thermal energy storage, next to latent or sensible energy storage. In this concept the reaction enthalpy of a reversible gas-solid reaction is utilized as thermal energy storage, which potentially enables loss-free energy storage in the form of the separated products and offers the advantage of high energy densities [1,2]. The endothermic reaction (charging phase) can be driven by concentrated solar thermal energy, while the exothermic reaction (discharging phase) recovers the stored thermochemical energy during hours of high energy demand or low solar irradiation. Usually, the separate storage of gas and solid for thermochemical energy storage systems involves complex gas handling, e.g., for the CaO/CO_2 or $\text{CaO}/\text{H}_2\text{O}$ reaction systems. In contrast, metal oxides react with oxygen under atmospheric pressure. Oxygen as a gaseous reaction partner drastically simplifies the system's complexity, because ambient air can act as reactive gas.

Therefore, no separate storage of the gas is needed and an open reactor system is feasible, which makes metal oxides suitable thermal energy storage material for CSP plants [3,4]. Furthermore, the utilization of metal-oxide particles as heat transfer medium and storage material is possible. The investigated system concept based on metal-oxide particles is shown in Figure 1.

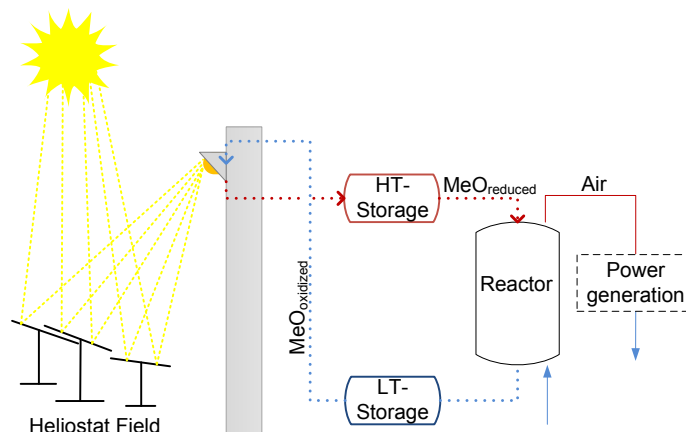
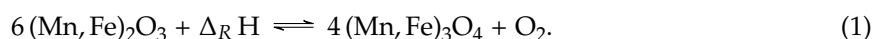


Figure 1. Concept of thermochemical energy storage based on metal oxide particles for solar tower applications. The metal oxide particles are cycled between a solar tower, high temperature (HT) storage, the reactor for discharging, and a low temperature (LT) storage.

Metal oxide particles are circulated between a solar receiver for charging and a continuously operated reactor for discharging. At this point, it is crucial to extract the thermochemical and sensible share in stored thermal energy to boost the overall system efficiency, since metal oxides react under elevated temperatures (700 °C to 1400 °C [3,4]). The considered system concept is able to supply dispatchable renewable energy. Furthermore, the storage capacity and system power are decoupled, which results in an improved operational flexibility.

This work focuses, therefore, on manganese-iron oxide as a reference material to investigate the simultaneous sensible and thermochemical heat extraction. The reaction equation of the redox reaction of manganese-iron oxide is given below:



The (Mn, Fe)₂O₃ granules with a Mn/(Mn + Fe) ratio of 0.75 were already successfully tested in a lab-scale packed bed reactor by our group [5]. Moreover, sufficient redox cycle stability of manganese-iron oxide has been proven by Wokon et al. [6], which represents a part of our preliminary work for this study.

In the presented system (Figure 1), the discharging is realized using a moving bed reactor for direct heat transfer to a counter-current gas flow. The moving bed concept is widely applied when the redox reaction of metal oxides is in focus; e.g., in chemical-looping combustion (CLC) or for iron-ore reduction in the steel-making industry. In general, a moving bed reactor presents a simple design for continuous movement of particles with the possibility to transfer sensible and thermochemical energy from the particles to a gas flow [7]. In CLC, high reaction conversion of metal oxide particles has been reported for moving bed reactors in bench-scale [8], with a thermal power of 25 kW [9] or up to 30 kW [7]. Furthermore, the moving bed design causes low mechanical stress for the particles and low parasitic losses. Therefore, the concept of a moving bed reactor was chosen for this study.

Several steady-state models have been suggested for a moving bed simulation. A one-dimensional (1D), steady-state model with an assumed local thermal equilibrium is presented for iron making in [10] and validated with a lab-scale reactor. Optimal operational parameters for iron making using a counter-current moving bed, i.e., a shaft furnace, are obtained with a 1D steady-state model in [11–13], where no local thermal equilibrium between gas and solid is assumed. The authors of [14] set up a 1D

model for the direct reduction of hematite in a moving bed in dimensionless form. The reaction in a pellet is simulated with a three-moving-front model and the inclusion of the water-gas shift reaction is discussed. Furthermore, a 2D model was developed, including a shrinking core model [15] for the kinetics of iron oxide reduction.

Transient models have been proposed as well for both CLC and iron-making processes. The authors of [16] developed a 1D model for the direct reduction of hematite in a counter-current moving bed reactor. A modified grain model is applied for the kinetics of the multiple gas-solid reactions in the pellet and was validated with experimental data. In [17], a 1D model for direct and indirect heat transfer in a counter-current moving bed equipped with heat transfer tubes is proposed for post combustion CO₂ capture. The effect of the flow rate on CO₂ capture is discussed, as is a dynamic process response to variations of inlet temperature, solid sorbent loading, and gas composition.

So far, simulative approaches on moving bed reactors, based on the redox reaction of metal oxides, focus mainly on the overall conversion; i.e., the conversion of fuel or oxygen carrier in chemical-looping combustion or the production of iron in the steel-making industry. However, the envisaged system concept (see Figure 1) relies on a counter-current moving bed reactor, which is optimized for gas-solid heat transfer, including both thermochemical and sensible thermal energy. As a consequence, this study focuses on the extraction of thermal energy and the effect of the conversion and operational parameters on achievable thermal power and energy density. Furthermore, the combined extraction of thermochemical and sensible thermal energy is discussed with respect to power and energy density. A transient 1D model is presented for a counter-current moving bed based on the oxidation of (Mn_{0.75}Fe_{0.25})₃O₄ applied as reference material. The model is validated with experimental data of a fixed-bed reactor. The limiting factors of the moving bed concept, in the context of thermochemical energy storage, are investigated further by means of sensitivity analyses.

2. Model Description

This work presents a one-dimensional FEM model of a counter-current moving bed reactor, suitable for thermal energy extraction in the presented system (Figure 1). At first, the geometry is described and assumptions are stated. Then, governing equations are presented and initial and boundary conditions are given.

2.1. Geometry of the Moving Bed

The 1D geometry of the counter-current moving bed reactor is presented in Figure 2a. A bed height of 0.7 m is simulated with the gas inlet at position $x = 0$ m and the particle inlet at $x = 0.7$ m. A mesh refinement study showed that as the number of elements in mesh increased from 100 to 1000 and from 1000 to 2000, the solid outlet temperature changed by 1.2 % and 0.016 ‰ respectively. Since the results do not change much by increasing the number of elements beyond 1000, the geometry is represented by 1000 elements of equal size.

2.2. Assumptions

The following assumptions are made:

- (i) The characteristic behavior of a counter-current moving bed reactor can be represented by a 1D model, since the main effects are expected to occur in the axial direction. Thus, the thermal energy losses to the surrounding are neglected.
- (ii) For the gaseous components of air, the ideal gas law can be applied.
- (iii) The total porosity of the manganese-iron oxide bulk does not change between oxidized and reduced phase or over consecutive cycles, based on [18] for a similar material composition.
- (iv) The solid particles have a homogeneous temperature distribution and are treated as a continuum, since the Biot-number is sufficiently small.

- (v) The work done by pressure change can be neglected in the energy balance for the gas phase, based on ([19] p. 41).

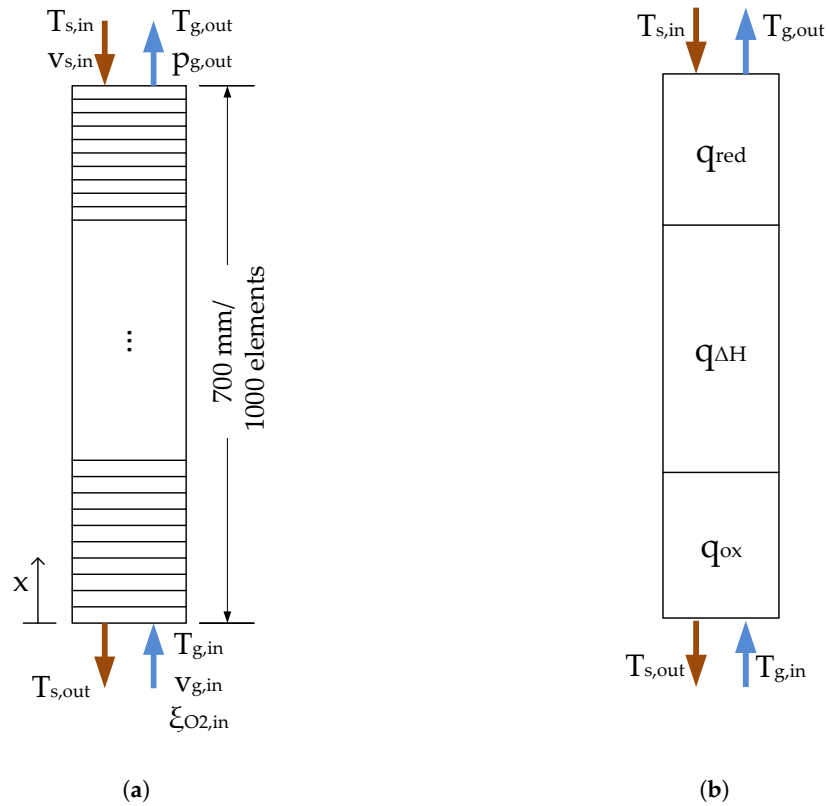


Figure 2. (a) 1D geometry of the moving bed reactor, including the boundary conditions at the inlet (in) or outlet (out) of the gas (g) and solid (s) flows. (b) Schematic description of the three heat transfer sections: sensible thermal energy of the reduced phase (q_{red}), thermochemical energy due to reaction enthalpy ($q_{\Delta H}$), and sensible thermal energy of the oxidized phase (q_{ox}).

2.3. Mathematical Formulation

The governing equations are derived as follows, considering the assumptions and simplifications. The mass balance for the gas phase is expressed as:

$$\frac{\partial(\epsilon \rho_g)}{\partial t} + \nabla \cdot (\rho_g \vec{v}_g) = -(1 - \epsilon) q_R, \quad (2)$$

where ϵ is the total void fraction in the bulk, ρ_g the gas density, \vec{v}_g the superficial gas velocity, and q_R the chemical production rate.

As the O_2 concentration changes due to the reaction, and the reaction rate depends on the O_2 partial pressure, the mass balance of O_2 also needs to be considered. The mass balance for O_2 is:

$$\epsilon \rho_g \frac{\partial \xi_{O_2}}{\partial t} + \rho_g \vec{v}_g \cdot \nabla \xi_{O_2} - \nabla \cdot (\rho_g D \nabla \xi_{O_2}) = -(1 - \epsilon)(1 - \xi_{O_2}) q_R, \quad (3)$$

where ξ_{O_2} is the mass fraction of O_2 , and D the diffusion coefficient between O_2 and N_2 .

The momentum equation for the gas phase is considered according to Darcy's law, where the superficial gas velocity \vec{v}_g and the pressure difference ∇P are correlated:

$$\vec{v}_g = -\frac{K}{\mu} \nabla P. \quad (4)$$

Here, μ is the dynamic viscosity of the gas. The permeability constant K is determined with the Carman-Kozeny relationship $K = \frac{d_p^2 \epsilon_b^3}{180(1-\epsilon_b)^2}$, which is valid for approximately spherical shaped particles with a narrow range of diameters d_p . In this case, ϵ_b is the bulk porosity and ϵ_{por} the particle porosity, which are linked to the total porosity ϵ according to:

$$(1 - \epsilon) = (1 - \epsilon_b)(1 - \epsilon_{por}). \quad (5)$$

The energy balance of the gas phase and solid phase can be written according to ([19] p. 42):

$$\left(\epsilon \rho_g c_{p_g} \right) \frac{\partial T_g}{\partial t} + \left(\rho_g c_{p_g} \vec{v}_g \right) \cdot \nabla T_g = -\nabla \cdot \left(-\epsilon_b \lambda_g \nabla T_g \right) + h_{gs} a_{gs} (T_s - T_g), \quad (6)$$

$$\left((1 - \epsilon) \rho_s c_s \right) \frac{\partial T_s}{\partial t} + \left(\rho_s c_s \vec{v}_s \right) \cdot \nabla T_s = -\nabla \cdot \left(-\lambda_{s,eff} \nabla T_s \right) + h_{gs} a_{gs} (T_g - T_s) + (1 - \epsilon) q_R \Delta H. \quad (7)$$

Here, ρ_g and ρ_s are the density; c_{p_g} and c_s are the specific heat capacities; T_g and T_s are the temperatures; and \vec{v}_g and \vec{v}_s are the superficial velocities of the gas and solid phases, respectively. The effective thermal conductivity of the solid $\lambda_{s,eff} = \lambda_{bulk,eff} - \epsilon_b * \lambda_g$ is calculated with the effective thermal conductivity of the bulk $\lambda_{bulk,eff}$ according to the extended Zehner-Bauer-Schlünder model, which also includes the radiative contribution [20,21]. For the convective heat transfer coefficient h_{gs} in a counter-current moving bed reactor, the correlation according to [22] is applied, together with the specific surface area $a_{gs} = \frac{6(1-\epsilon_b)}{d_p}$.

Initial and Boundary Conditions

The initial temperatures of gas and solid are set to 1050 °C. At the gas inlet ($x = 0$ m), the mass fraction of O_2 $\xi_{O_2,in}$ is set to 23.27%, and the gas inlet temperature $T_{g,in}$ equals 300 °C. Similarly, for the particle inlet ($x = 0.7$ m), the gas pressure $p_{g,out}$ is set to ambient conditions (1013.25 hPa), and the particle inlet temperature $T_{s,in}$ to 1050 °C.

3. Material Properties

The considered material $(Mn_{0.75}Fe_{0.25})_2O_3$ was investigated concerning thermodynamics and kinetics in a previous study [6] of our group. The particles were produced by VITO (Mol, Belgium) via build-up granulation. For the preparation, the raw materials Mn_3O_4 (Trimanox electronic grade, Chemalloy) and Fe_2O_3 (98% metal basis, Alfa Aesar) were mixed in powder form, before the granulation using an Eirich Mixer (see [6] for further details). Table 1 presents a compilation of relevant material properties for the model description.

Three main parameters of the material are characteristic for the planned combination of heat transfer of thermochemical and sensible energy (see Figure 2b). Firstly, the heat transfer of sensible energy (q_{red}) between the reduced solid phase and the gas flow is confined downwards by the onset temperature of the oxidation, because this temperature is regarded as the lower threshold value of this heat transfer section. Due to the occurrence of thermal hysteresis of the manganese-iron oxide, the temperature threshold value for the oxidation onset determined via simultaneous thermal analyses deviates from the calculated thermodynamic equilibrium temperature. For example, an oxygen partial pressure of 20.4 kPa yields an oxidation onset temperature of 918.3 °C, whereas thermodynamic equilibrium calculations result in 966.8 °C [6]. Secondly, the transfer of the released heat of reaction ($q_{\Delta H}$) is directly influenced by the reaction kinetics of the Mn-Fe oxide. The oxidation kinetics has been already determined by means of thermogravimetric analysis [6]:

$$\frac{d\alpha}{dt} = 1.78 \times 10^{16} \frac{1}{s} \cdot \exp\left(-\frac{463.53 \frac{\text{kJ}}{\text{mol}}}{R \cdot T}\right) \cdot \left(\ln \frac{p_{\text{O}_2}}{p_{\text{eq}}(T)}\right)^{7.06} \times 1.38(1-\alpha)(-\ln(1-\alpha))^{1-\frac{1}{1.38}}. \quad (8)$$

Table 1. Material parameters.

Parameter	Symbol	Value/Correlation	Unit	Reference
Mean particle diameter	d_p	2.42	mm	[6]
Bulk density	ρ_{bulk}	1353	kg/m ³	[5]
Reaction enthalpy, based on oxidized phase	$\Delta_r H$	271	J/g	[6]
Specific heat capacity of Mn ₃ O ₄	$c_{p_{\text{red}}}$	$\left(613.07996 + 2.58034\left(\frac{T_s}{\text{K}} - 298\right)^{0.68764}\right)$	J/kg/K	[23]
Specific heat capacity of (Mn _{0.75} Fe _{0.25}) ₂ O ₃	$c_{p_{\text{ox}}}$	$\left(669.28596 + 0.62604\left(\frac{T_s}{\text{K}} - 298\right)^{0.8982}\right)$	J/kg/K	see Appendix A
Intrinsic thermal conductivity for Mn ₂ O ₃ (400 K to 1400 K)	λ_s	$0.99395 + 6.98315 \times 10^{-4} \cdot \frac{T_s}{\text{K}} - 1.23972 \times 10^{-7} \cdot \frac{T_s^2}{\text{K}^2}$	W/m/K	polynomial fit based on c_p for Mn ₂ O ₃ [23] and thermal diffusivity [24]
True density of (Mn _{0.75} Fe _{0.25}) ₂ O ₃	ρ_s	5125	kg/m ³	measured via He-pycnometry
Total porosity	ϵ	0.736	—	calculated with true density
Bulk porosity	ϵ_b	0.34	—	calculated with Equation (5)
Intra-particle porosity	ϵ_{por}	0.6	—	measured via Hg-intrusion-porosimetry

Finally, the specific heat capacity $c_{p_{\text{ox}}}$ is a crucial thermophysical parameter considering the amount of heat that can be transferred between the oxidized phase and the gas flow (q_{ox}). The $c_{p_{\text{ox}}}$ values of the phase (Mn_{0.75}Fe_{0.25})₂O₃ were determined by means of differential scanning calorimetry (DSC). The specific heat capacity of the reduced phase $c_{p_{\text{red}}}$ is approximated with the specific heat capacity of Mn₃O₄ [23]. Values applied for $c_{p_{\text{ox}}}$ and $c_{p_{\text{red}}}$ are illustrated in Appendix A.

The thermal conductivity of the specific oxide (Mn_{0.75}Fe_{0.25})₂O₃ is unavailable presently. Therefore, the reported values for manganese oxides are applied for determination of the intrinsic thermal conductivity of the solid material λ_s . With the specific heat capacity of Mn₂O₃ [23] and thermal diffusivity [24] of manganese ores, the intrinsic thermal conductivity is estimated for a temperature range between 400 K and 1400 K. A polynomial fit function for this temperature range (listed in Table 1) is used as an input value for the determination of the effective thermal conductivity of the bulk $\lambda_{\text{bulk,eff}}$ according to the extended Zehner-Bauer-Schlünder model [20,21]. Furthermore, the emissivity of the manganese-iron oxide particles was approximated to 0.87, based on measured values for Fe₂O₃ particles [25] and a Mn-Fe-Zr-coating [26].

4. Validation

The model is validated with experimental results from our group [5] using a fixed bed reactor for direct heat transfer between (Mn_{0.75}Fe_{0.25})₂O₃/(Mn_{0.75}Fe_{0.25})₃O₄ and a gas flow of ambient air.

4.1. Experimental Setup for Validation

This section presents only the data of the experimental setup relevant for the model validation. A detailed description of the schematic setup and further experimental investigations can be found in [5]. A lab-scale tube reactor (nickel-based alloy 2.4856) with an inner diameter of 54.3 mm is filled

with 471.2 g metal-oxide particles ($\text{Mn}_{0.75}\text{Fe}_{0.25}\text{O}_3$). Air heated by means of an electrical gas heater, integrated into the reactor unit, enters the reaction bed from the bottom via a perforated plate and a gas distribution disc. A vertical tube furnace encases the reactor tube to assist the gas heater, minimize heat losses to the ambient, and to control the bulk temperature. Four thermocouples (Type K, class 1, $\varnothing = 1$ mm) measure the temperature profile in the central position along the bed height at distances of 10 mm (T1), 50 mm (T2), 90 mm (T3), and 130 mm (T4) from the gas distribution disc. The oxygen concentration in the off-gas is analyzed via a paramagnetic oxygen measurement (NGA-2000 MLT-2, Emerson Process Management/Rosemount Analytical). A change of the oxygen concentration in the off-gas can be attributed to the redox reaction of the metal-oxide bulk and is thus used for conversion calculations.

4.2. Model Validation

The model is validated based on a discharging experiment in the fixed bed reactor using the described granular manganese-iron oxide particles. Ten redox cycles have been performed with the material prior to this dynamic discharging step presented here. The validation experiment corresponds to the experiment cycle number 11 in [5]. In the preceding charging stage, the bulk was heated to a temperature of 1040°C ($T_{s,0}$) and reduced with 10 L/min air flow \dot{V}_n . All gas flow rates in this study are based on norm conditions ($T_{g,n} = 0^\circ\text{C}$ and $p_n = 1013.25$ hPa). For discharging, the tube furnace and the air inlet temperature ($T_{g,in}$) were reduced at a rate of 5 K/min down to 400°C , during which phase the oxidation was initiated. In Figure 3, simulation and experimental results are displayed.

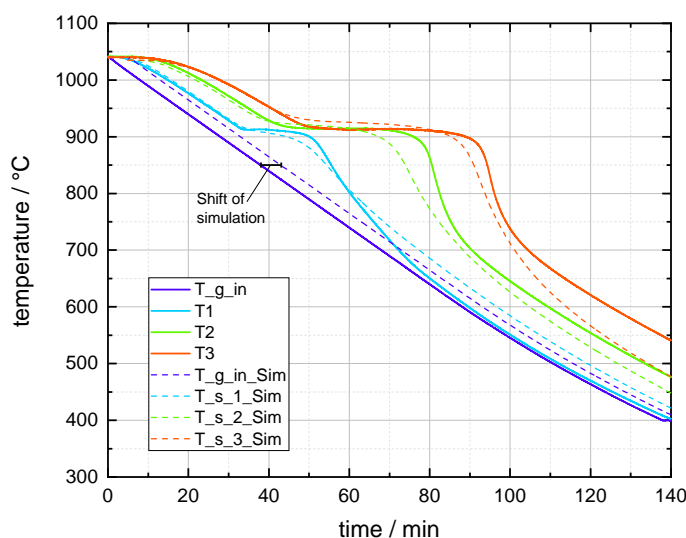


Figure 3. Simulation of dynamic cooling with oxidation of $(\text{Mn}_{0.75}\text{Fe}_{0.25})_3\text{O}_4$ in a lab-scale fixed bed reactor. Solid lines display temperatures measured in the experiment, whereas dashed lines present the simulated temperatures. The simulation was shifted by 5 min to allow for a better comparison.

The solid temperatures decrease until the exothermic oxidation stabilizes the temperatures at a plateau for about 16 min at a bed height of 10 mm (T1) and up to 38 min at a bed height of 90 mm (T3). The simulated solid temperatures show a similar trend with a maximal offset of 13°C to the measured temperature plateau of $\approx 913^\circ\text{C}$. However, during the first minutes of the discharging phase, the difference between the gas inlet temperature and the solid temperature T1 in the experiment exceeds the difference in the simulation. To compensate the experimental delay, the gas inlet temperature is shifted by 5 min for the simulation. A detailed discussion of this time shift is presented in Appendix B. In the end, the model sufficiently reflects the oxidation progress and the cooling effect of the gas on the

manganese-iron oxide. The simulation meets the onset temperature of the reaction and is able to describe the course of the solid temperature in the temperature range, where only thermal energy is transferred.

5. Results and Discussion

As a next step, the bulk movement is included in the model, which is based on the same equations (Section 2.3). This model is applied to investigate the impacts of operational parameters, i.e., gas and particle flow, on the thermal power and energy density.

5.1. Moving Bed Design

At first, a rough estimate for such a counter-current moving bed system has to be made, since now the power output is affected by further operational parameters, in comparison to a fixed-bed reactor. As an exemplary system, a thermal power of 3 kW is considered as realistic, which is in range of the discussed fixed-bed reactor. Therefore, the operational parameters required as starting values for the moving bed simulation were analytically determined for a thermal power of 3 kW. For this initial estimation of particle and gas mass flows and required bed height, only convective heat transfer between gas and solid is considered. Since a heat transfer of sensible and thermochemical energy between metal oxide particles and a counter-current gas stream occurs, the moving bed can be divided into three sections (see also, Figure 2b):

1. Sensible heat transfer q_{red} till metal oxide granules reach the onset temperature of oxidation ($\dot{Q}_{red} = \int_{T_{s,in}}^{T_{s,out}} \dot{m}_s c_{p,s}(T_s) dT_s$);
2. Heat transfer of thermochemical energy $q_{\Delta H}$, where metal oxide granules are oxidized and the released reaction enthalpy is transferred to the gas stream ($q_{\Delta H} = \Delta_r H$);
3. Sensible heat transfer q_{ox} till metal oxide granules reach the desired particle outlet temperature ($\dot{Q}_{ox} = \int_{T_{g,in}}^{T_{g,out}} \dot{m}_g c_{p,g}(T) dT_g$).

The estimation of mass flows is based on the NTU (number of transfer units) method, which was developed for sensible heat exchangers. One crucial characteristic factor to evaluate a moving bed reactor is the heat capacity rate ratio F , defined as:

$$F = \frac{\dot{m}_{red} \cdot \tilde{c}_{p,red}(T_{m,red}) + \dot{m}_{ox} \cdot \tilde{c}_{p,ox}(T_{m,ox})}{\dot{m}_g \cdot \tilde{c}_{p,g}(T_{m,g})}. \quad (9)$$

Here, \dot{m}_{red} and \dot{m}_{ox} are the mass flow rates, and $\tilde{c}_{p,red}$ and $\tilde{c}_{p,ox}$ are the averaged specific heat capacities for the mean temperature $T_{m,red}$ and $T_{m,ox}$ of the reduced and oxidized phase, respectively. The rough estimation yields that a particle mass flow of 4 g/s in counter-current to a gas flow \dot{V}_n of 183 L/min is necessary to achieve a heat transfer of 3 kW, considering also the boundary conditions given in Section 2.3. The gas and solid velocities v_g and v_s are calculated with an assumed reactor diameter of 0.152 m. A detailed description for the calculations is given in Appendix C.

5.2. Temperature Profiles of a Thermochemical Moving Bed

The estimated gas and particle flow rates were used as initial input values for first simulations. Figure 4 displays the solid temperature along the height of the moving bed for time steps normalized to $t_{stat} = 400$ min, which equals the time till a stationary temperature profile is achieved for the given particle and gas flow rates. The particle bed is simulated with a starting and inlet temperature of 1050 °C and a gas inlet temperature of 300 °C. Therefore, the particle temperature starts to decrease at position 0. The highest temperature gradient arises between the gas inlet and 5 cm above. A nearly isothermal temperature zone in the range of 900 °C to 942 °C moves upwards until a steady state is reached. After 400 min, the particles exit the moving bed with 329 °C at position $x = 0$, and a steady-state operation is reached.

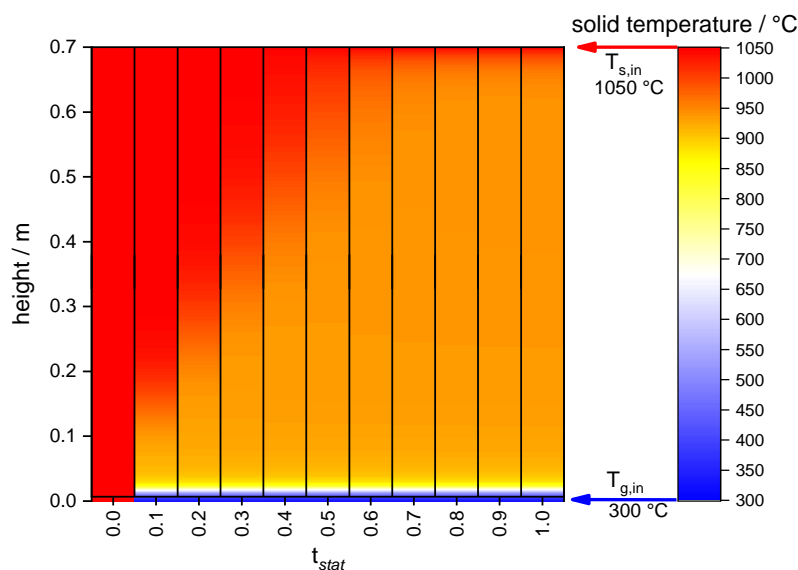


Figure 4. Heat map for the solid temperature development along the bed height of 0.7 m of a moving bed with Mn-Fe-oxide particles moving with 4 g/s in counter-current to 183 L/min air flow \dot{V}_n . The time steps are normalized to the time t_{stat} when a stationary temperature profile occurs after 400 min for the current particle and gas flow rates.

Comparison of Inert and Thermochemical Moving Bed

The reaction was disabled for one simulation to highlight the difference between a purely sensible (inert) and a thermochemical material in a moving bed reactor. In Figure 5a two different stationary temperature profiles for the manganese-iron-oxide particles and the counter-current gas flow are displayed along the height of the moving bed.

In general, the gas and solid temperature profiles are very similar in the reactive and inert cases. Considering the reactive case, the uniform coloring in the heat map of Figure 4 ($t_{stat} = 1.0$) corresponds to the temperature plateau of the reactive case in Figure 5a. The solid temperature reaches 928 °C at a bed height of 0.1 m, and up to 940 °C at a height of 0.6 m.

Technically relevant p_{O_2} -T conditions experimentally determined based on simultaneous thermal analyses (see [6]) give a temperature threshold value of 919.6 °C for the oxidation onset at a p_{O_2} of 20.9 kPa. However, the equilibrium temperature for the phase change from the two-phase region “bixbyite + spinel” (spinel being the reduced phase) to the bixbyite (being the oxidized phase) was calculated to 967.9 °C for a p_{O_2} of 20.9 kPa [6]. Thus, the formed temperature plateau is in between the extrapolated onset temperature and thermodynamic equilibrium of the phase boundary “bixbyite”–“bixbyite + spinel.” Kinetic investigations further revealed the extremely low reaction rates of the oxidation at temperatures between the extrapolated onset temperature and the calculated equilibrium temperature [6]. In this area of “thermal hysteresis” especially, the oxidation reaction takes a long time to initiate and proceed; e.g., an isothermal oxidation at 926.6 °C required an induction period of over 30 min at an oxygen partial pressure of 20.4 kPa [6]. In Figure 5b the oxidation conversion along the bed height is displayed for an operation in steady state and corresponds to the gas and solid temperature course of the reactive case depicted in Figure 5a. The largest part of the reaction conversion is achieved in the cooling section close to the gas inlet within the first 5 cm of the bed, as the highest reaction rates occur in this temperature range of the prevailing temperature profile. However, the cooling rate seems to impede full oxidation conversion, as the conversion adds up to only 65% at the particle outlet. Remarkably, the overall conversion benefits only to a very small extent (conversion below $\sim 0.1\%$) from a bed height of 60 cm, between 0.1 m and 0.7 m. In this area of nearly isothermal conditions only a small amount of heat can be transferred from solid to gas, since the gas has already

reached the effective onset temperature. However, the low conversion of the material in the nearly isothermal bed section is still sufficient to stabilize the solid temperature against the cooling effect of the gas flow and thus form the isothermal bed section. Eventually, the reactor could be shortened to a bed height of around 15 cm, without negatively influencing the conversion, thermal power, or achievable energy density for these operational parameters. However, the displayed gas and solid temperature profiles strongly depend on kinetics and the convective heat transfer coefficient. The effect of faster kinetics and lower convective heat transfer between gas and solid will be further discussed in Section 5.4.

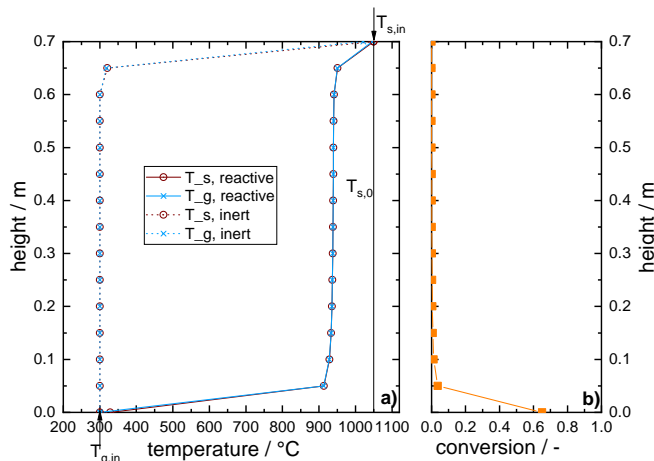


Figure 5. Results for a moving bed with 4 g/s Mn-Fe-oxide particles and counter-current air flow \dot{V}_n of 183 L/min operated in steady state. (a) Comparison of gas and solid temperature profiles with (solid line) and without (dotted line) reaction. (b) Reaction conversion along the bed height for operation in steady state.

In the considered inert moving bed (Figure 5), the solid particle temperature decreases to the level of the gas inlet temperature in a distance of less than 10 cm away from the particle inlet. Thus, the bed height could be limited to the area exhibiting this large temperature gradient without losing thermal power. Apparently, the heat flow due to the proceeding chemical reaction leads to an additional rate of heat flow from the solid to the gas compared to the case of purely sensible storage material, which shifts the major temperature gradient from the particle inlet (inert storage material) to the gas inlet (thermochemical storage material).

5.3. Flexibility of Power and Energy Density

5.3.1. The Effect of the Variation of Gas Flow Rates

In the scope of thermochemical energy storage, the main task of the simulated moving bed reactor is to transfer heat from Mn-Fe-oxide particles to a counter-current gas flow. Therefore, the effect of gas flow variation on the reactor performance is investigated in this section. In Figure 6, stationary solid temperature profiles are displayed for a particle flow rate of 4 g/s and various gas flow rates, ranging from 150 L/min to 230 L/min.

The profiles indicate a temperature plateau formation for gas flow rates between 150 L/min and 190 L/min. For higher flow rates, 210 L/min and above, a temperature profile similar to the purely inert moving bed in Figure 5a is obtained. In this case all three sections (q_{red} , $q_{\Delta H}$, q_{ox}), described above, are present within the top 5 cm of the moving bed. The point where the stationary temperature profile and hence the storage operation changes, between 190 L/min and 210 L/min, is called the “tipping point” hereinafter. The closer the gas flow is to this tipping point, the higher the temperature gradient is below and above the temperature plateau. This fact can be attributed to the higher heat capacity flow of the gas. Furthermore, with lower gas flow rates, the particles exit the moving bed with a higher outlet temperature. The corresponding conversion of the Mn-Fe-oxide particles is depicted in

Figure 6b. For gas flow rates above the tipping point, the kinetic limitation of the material leads to a reduced conversion as a consequence of increased cooling rates. Furthermore, the particles oxidize shortly after the particle inlet; i.e., in less than 5 cm. The oxidation of the particles can only take place within the range of the topmost 5 cm below the particle inlet.

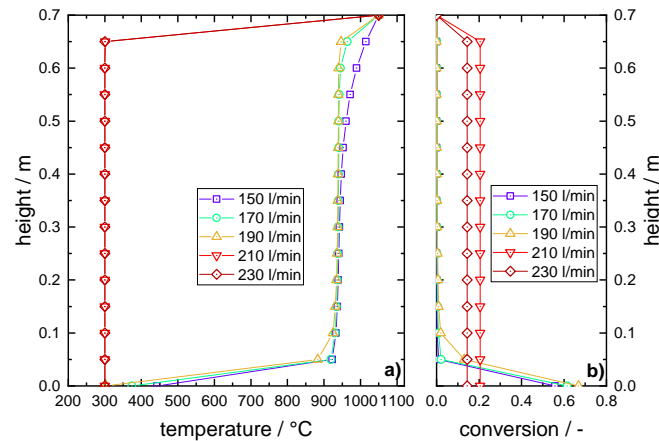


Figure 6. (a) Temperature profile of solid particles along the bed height of a moving bed (4 g/s particle flow rate) with different gas flow rates operated in steady state. (b) Conversion profiles along the bed height of the moving bed reactor operated in steady state.

The achieved conversion at the particle outlet ($x = 0$ m) and gas temperature at the gas outlet ($x = 0.7$ m) are displayed in Figure 7 in comparison to a purely inert moving bed of Mn-Fe-oxide particles with 4 g/s solid mass flow.

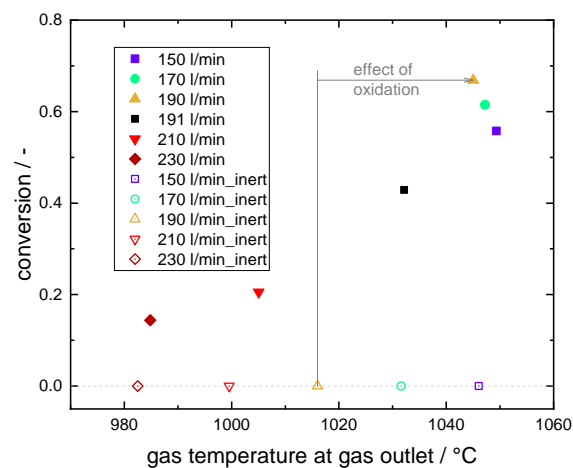


Figure 7. Obtained conversion at particle outlet ($x = 0$ m) and gas temperature at particle inlet ($x = 0.7$ m) of a moving bed (4 g/s particle flow rate) with different gas flow rates. Full symbols represent thermochemical storage material undergoing a chemical reaction; empty symbols represent inert storage material used for sensible storage only.

In general, higher gas flow rates lower the achievable gas outlet temperature. However, the increase in conversion (between \dot{V}_n 210 L/min and 190 L/min) is directly correlated to a strong increase in gas outlet temperature. Changing the gas flow \dot{V}_n from 190 L/min to 191 L/min shifts the gradient of the particle temperature to the particle inlet, resulting in a temperature profile similar to the profile of higher gas flow rates. This low increase of gas flow rate has a high impact on the achievable conversion and gas outlet temperature, which indicates the position of the tipping point in between those two gas flow rates for a particle flow rate of 4 g/s. A comparison to an inert moving

bed (see empty symbols at conversion 0.0 in Figure 7) highlights the benefit of the thermochemical material. In case of a gas flow \dot{V}_n of 190 L/min, the gas outlet temperature is increased by 29 °C due to the additional release of the reaction enthalpy with a reaction conversion of 66.9%. However, it has to be noted that by lowering the gas flow rate to, e.g., 150 L/min, the gas outlet temperature in the inert moving bed can reach a similar level to that with reactive material.

The correlation of transferred thermal power in a moving bed reactor with 4 g/s of Mn-Fe-oxide particles to the energy density is displayed for various gas flow rates in Figure 8.

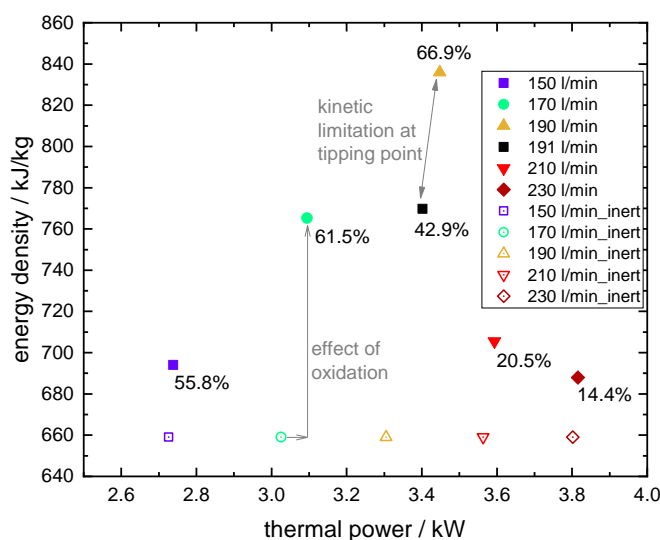


Figure 8. Thermal power and energy density of a moving bed of 4 g/s with different gas flow rates \dot{V}_n . The numbers next to the full symbols represent the conversion (%) achieved in steady state operation. Empty symbols represent the Mn-Fe-oxide particles acting only as sensible thermal storage material.

The calculation of the resulting gravimetric energy density is based on the solid inlet and outlet temperature, the specific heat capacity as stated in Table 1, and the achieved conversion of the Mn-Fe oxide (as highlighted in Figure 8). For the determination of the transferred thermal power, the corresponding rise in gas temperature is considered. Figure 8 also illustrates the results for a purely inert moving bed under the same operational conditions. In the investigated range of gas flow rates, the thermal power generally increases with increasing flow rate, whereas the energy density shows a peak when the gas flow rate is close to the tipping point. Furthermore, an increase of gas flow rate, and thus a lower gas outlet temperature (see Figure 7), still increases the thermal power in most cases. However, when the gas flow is increased to just above the tipping point, the thermal power slightly decreases due to a lower conversion and the accompanied strong decrease of gas outlet temperature. As the solid outlet temperature of the purely inert moving bed equals the gas inlet temperature in all cases shown, the energy density of the solid material remains unchanged. The rise in energy density can be attributed only to the reaction enthalpy and its effect on the gas and solid outlet temperatures, when comparing inert and reactive moving bed results. In case of a gas flow rate \dot{V}_n of 190 L/min and a conversion of 66.9%, the thermochemical share in energy density accounts for 23% of the total energy density of the storage material.

5.3.2. Optimizing the Gas and Particle Flow Rates for High Solid Conversion

In a next step, the flow rates were optimized for high reaction extents. For different selected particle flow rates between 1 g/s and 6 g/s, the gas flow rates were varied until the highest possible conversion could be observed for each particle flow rate. The highest conversion was found for a gas flow rate just below the tipping point, comparable to the findings in Figure 6.

In Figure 9a the temperature profiles of a moving bed with conversion optimized flow rates are displayed for steady state. Figure 9b shows the corresponding conversion profile along the bed height. The figure presents only a section of the 0.7 m long simulated geometry. The temperature profiles in the excluded section ($x = 0.2$ m to $x = 0.7$ m) show a similar trend to the temperature profiles in Figure 6. A temperature plateau in the range of 931 °C to 939 °C is formed for all flow rate combinations. In general, the profiles vary only to a small extent in the section where the oxidation occurs (position 0.05 m to 0.1 m) and sensible heat is transferred from the solid to the gas flow (position 0 m to 0.1 m). The solid temperature at the outlet is not affected by this flow rate variation. Therefore, the change in achieved energy density (see Figure 10) of the Mn-Fe-oxide particles is only caused by the different extent of conversion, as illustrated in Figure 9b. The lower the flow rates, the higher the achievable conversion. This clearly demonstrates the kinetic limitation of the moving bed with Mn-Fe-oxide particles, undergoing the redox transition $(\text{Mn}_{0.75}\text{Fe}_{0.25})_3\text{O}_4 / (\text{Mn}_{0.75}\text{Fe}_{0.25})_2\text{O}_3$.

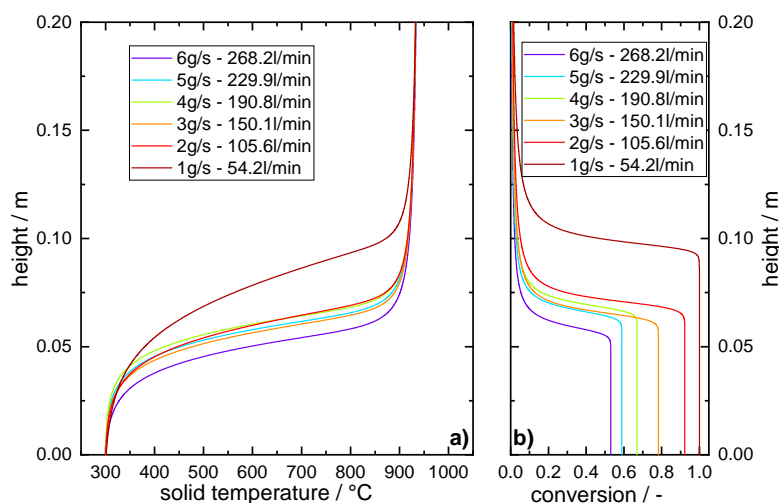


Figure 9. Solid temperatures (a) and conversion profiles (b) at a 0.2 m section of the 0.7 m simulated bed height with different particle and gas flow rates at steady state operation. The flow rates were chosen for optimized overall conversion of the particles obtained at the reactor outlet for the given particle mass flow.

The attained thermal power for the flow rate variations is plotted against the achieved energy density of the Mn-Fe-oxide particles in Figure 10. The extent of conversion and the residence time of the particles in a bed height of 10 cm are stated as well.

The energy density and the thermal power follow a contrarian trend when both flow rates are increased. Higher flow rates result in a higher thermal power, whereas the energy density of the manganese-iron oxide decreases. A higher solid mass flow leads to a decrease of residence time in the bed section exhibiting high temperature gradients. Therefore, the achievable conversion is lower, and thus, the energy density is too (see also Figure 9). As a consequence, the share of thermochemical energy in the overall energy density decreases from 30.8% with 1 g/s to 19.1% for 6 g/s. The heat capacity rate ratio F (Equation (9)) changes from 1.3 to 1.6, when the particle mass flow is increased from 1 g/s to 6 g/s. Apparently, the solid heat capacity flow together with the achievable conversion, and thus release of reaction enthalpy determines the gas flow rate at the tipping point. The heat capacity rate ratio F increases with higher gas and particle flow rates, since the achievable conversion depends on the reaction kinetics. Thus, in the case of the presented manganese-iron oxide, the position of the tipping point, i.e., solid and gas mass flows, depends also on the reaction kinetics. However, higher gas and particle flow rates still result in higher thermal power. Thus, besides the material kinetics being the limiting factor, the thermal power of the moving bed reactor can be adjusted by applying higher flow rates.

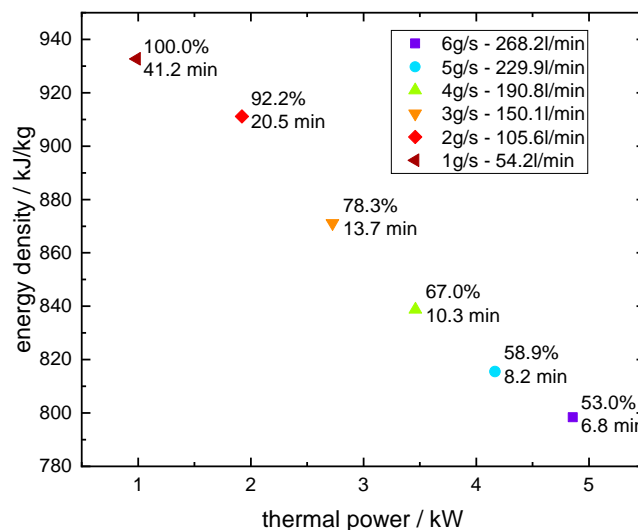


Figure 10. Thermal power of the moving bed reactor for the steady state case and energy density of the Mn-Fe-oxide with different particle flows and gas flow rates. The gas flow rates were chosen for optimized conversion of the particles at the reactor outlet. The overall conversion and the residence time of the particles in the first 10 cm after the gas inlet are also included.

So far, the following remarks can be made with respect to the simulative investigation of a moving bed with $(\text{Mn}_{0.75}\text{Fe}_{0.25})_3\text{O}_4$ / $(\text{Mn}_{0.75}\text{Fe}_{0.25})_2\text{O}_3$ particles:

- Increasing the gas flow rate has a stronger impact on the thermal power than a higher extent of conversion in the range of the operational parameters investigated.
- Reaction kinetics are the limiting factor: a material with faster kinetics would be required to allow for the exploitation of both the sensible share and the complete thermochemical share in energy density.
- The oxidation stabilizes the temperature along the bed height for a gas flow rate below the tipping point and increases the gas outlet temperature.
- The moving bed reactor facilitates a more stable gas outlet temperature with a fluctuating gas flow below the tipping point, which results from the oxidation of the Mn-Fe-oxide particles.

5.4. Sensitivity Analysis

As a next step, the effect of faster reaction kinetics and the sensitivity of the results towards a change of the convective heat transfer coefficient, e.g., due to channeling effects in the bulk material, are investigated.

5.4.1. The Influence of Channeling Effects on the Moving Bed Operation

The effect of potentially-occurring channeling on the gas-solid heat transfer and the achievable conversion was examined based on the moving bed simulation model. Furthermore, the required bed height for gas-solid heat transfer can be deduced for a bulk exhibiting channeling effects. Kunii and Suzuki [27] investigated the convective heat transfer coefficient for low Péclet numbers ($Pe < 10$) for packed bed reactors. The authors included the channeling effect in the determination of the heat transfer coefficient with a channeling ratio ζ , which is defined as the average channel length to the particle diameter d_p . Figure 11 illustrates the effect of a variation of the channeling ratio ζ on the steady state temperature and conversion profile of a moving bed with a particle mass flow of 4 g/s in counter-current to an air flow \dot{V}_n of 190.8 L/min.

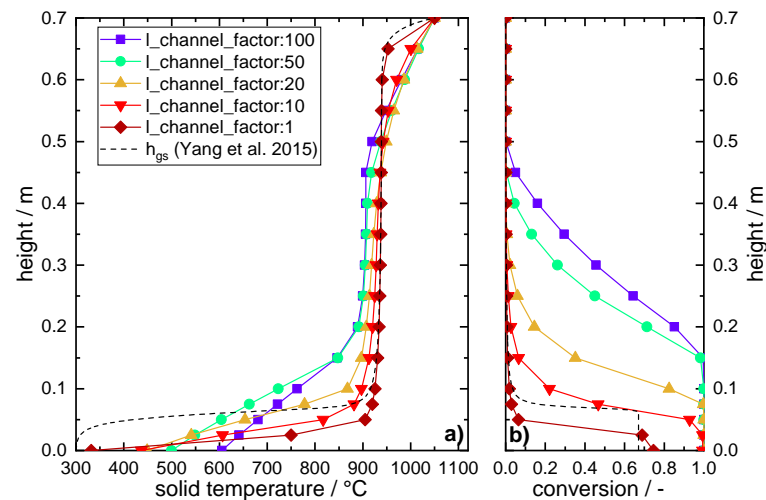


Figure 11. A variation of the channeling ratio ζ between 1 (no channels) and 100 (channels with 100 times length of d_p). (a) Solid temperature profile of the stationary moving bed with 4 g/s in counter-current to an air flow rate of 190.8 L/min and (b) the conversion profile of the Mn-Fe-oxide particles.

The channeling ratio is varied between 1 and 100, where 100 would refer to a channel length of 0.242 m. The solid temperature profile, which results from the application of the heat transfer coefficient for a moving bed (Yang et al. 2015 [22]), is added as a comparison to the channel factor of 1. The application of the heat transfer coefficient according to Kunii and Suzuki yields lower coefficients which can be identified by the lower temperature gradient at the gas inlet area. For example, the heat transfer coefficient h_{gs} equals 66.4 W/m²/K for an application of h_{gs} according to Kunii and Suzuki, whereas h_{gs} by Yang et. al gives 182.7 W/m²/K at a medium bed height ($x = 0.35$ m), where the solid temperature is 937 °C in both simulations.

With an increased channel length, the convective heat transfer coefficient decreases. As a result, the plateau temperature of the nearly isothermal bed height drops and the temperature gradient at the particle inlet and outlet is less steep. Therefore, the oxidation kinetics allow for an earlier beginning of the oxidation. Furthermore, the particle residence time in a temperature range, which is suitable for oxidation, is prolonged. In summary, lower convective heat transfer due to channeling effects lead to a higher extent of the reaction conversion. However, the particle outlet temperature increases, thus decreasing the sensible share in energy density. It is obvious that the convective heat transfer coefficient has a strong impact on the required bed height to assure both thermochemical and sensible heat transfer. Therefore, experimental investigations are required to analyze the flowability and potential channeling effect of manganese-iron-oxide particles in a counter-current moving bed.

5.4.2. Kinetic Limitation

In many cases, the oxidation reaction of metal oxides was found to proceed slower than the reduction and is thus often the limiting reaction step, e.g., for CuO / Cu₂O [28], Co₃O₄ / CoO [29,30], or manganese-iron-oxide [6,31]. However, some binary mixtures of Co-Cu, Cu-Mn or the pure metal oxide pair Fe₂O₃ / Fe₃O₄ promise faster oxidation kinetics [3,32]. For example, the oxidation of Fe₃O₄ was observed in less than 20 s within a temperature range of 673 K to 973 K during isothermal thermogravimetric analyses in 80% O₂, but with a conversion just above 80%.

To investigate the sensitivity of achievable energy densities and thermal power, the storage material in the current study was idealized to overcome kinetic limitations. Therefore, in this section, the kinetic limitation is assumed to be artificially inhibited by multiplying the reaction rate with the arbitrarily chosen factor of 10. In Figure 12, the kinetically improved material is compared to the actual

material concerning energy density and thermal power for fixed particle flow rates. The gas flow rate was increased to exploit the improved energy density and thus heat release transferred to the gas.

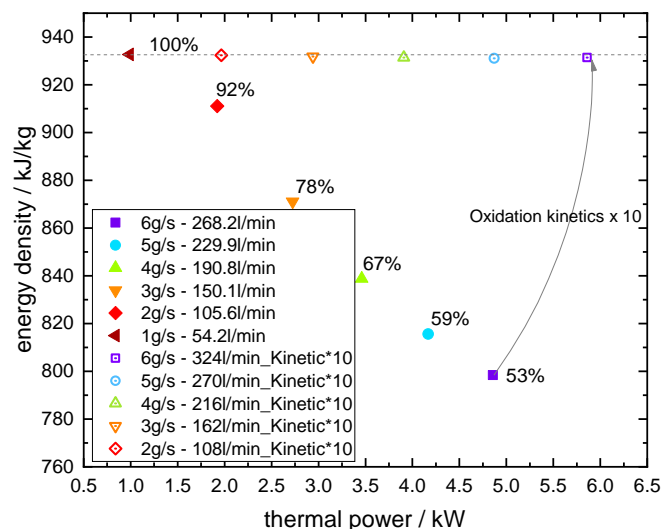


Figure 12. Energy density and thermal power of varied flow rates with either standard kinetics (full symbol) or accelerated kinetics (empty symbols). The numbers mark the conversion achieved for each simulated pair of flow rates.

The artificially accelerated kinetics (times 10) overcome the kinetic limitation. Therefore, the energy density becomes independent from the chosen flow rates or thermal power. In addition, the thermal power can be also increased because higher gas flow rates are possible. The ratio F is constant at 1.3 for the case of accelerated kinetics, which can thus be considered as the ideal flow rate ratio (tipping point) for the investigated manganese-iron oxide in the absence of the kinetic limitation.

Besides the selection of different materials with faster kinetics, other possibilities are conceivable to overcome this limitation. In principle, the application of a higher oxygen partial pressure would accelerate the kinetics [6], and thus increase the conversion for the same flow rates. However, this is technically not favored because the main advantage of the metal oxides in this system concept is to use ambient air as heat transfer fluid. Furthermore, indirect heat extraction along the bed section with nearly isothermal conditions could lead to higher reaction rates, if the plateau temperature can be lowered to below 920 °C. This could be achieved by preheating the gas indirectly along the bed section with nearly isothermal conditions before introducing the preheated gas to the moving bed. However, this would result in higher solid outlet temperatures.

6. Conclusions

A 1D moving bed simulation for thermochemical energy storage has been validated with experimental data of a packed bed reactor. The model has then been extended by particle flow for the simulation of a counter-current moving bed reactor in regard to the system concept of a solar thermal power plant. The following conclusions can be drawn for a steady state operation:

- The oxidation of the manganese-iron-oxide particles in a thermochemical moving bed leads to a bed section with nearly isothermal conditions. However, the major part of the reaction conversion does not occur in this isothermal section, but overlaps with the cooling of the particles below the temperature plateau. Thus, the thermochemical section $q_{\Delta H}$ and the sensible section q_{ox} develop simultaneously. Furthermore, the exothermic reaction leads to an increase of the energy density and thermal power in comparison to a reactor operated with inert storage material, since higher gas flows can be applied for a fixed particle flow rate. From a technical point of

view, the isothermal section would be suitable for an indirect heat transfer to lower the plateau temperature and support oxidation kinetics. Thereby, the reaction enthalpy of the storage material can be fully exploited.

- Oxidation kinetics of the redox transition $(\text{Mn}_{0.75}\text{Fe}_{0.25})_2\text{O}_3/(\text{Mn}_{0.75}\text{Fe}_{0.25})_3\text{O}_4$ are the limiting factor concerning the attainable energy density and thermal power of the moving bed reactor. A full conversion is only achievable for low gas and solid flow rate (e.g., particle flow in the range of 0.001 kg/s. If higher gas flow rates are applied and the exerted cooling effect is too high, an isothermal section cannot be formed, the conversion strongly decreases, and the temperature profile resembles the profile of a moving bed with inert storage material. Both the energy density and achievable thermal power benefit from faster kinetics when a higher reaction rate is assumed.
- The thermal power and energy density show a contrarian trend when the particle and gas flow rates are increased and the gas flow rate is determined for the maximum achievable reaction conversion. The energy density drops, whereas the thermal power is increased independently of the achieved reaction conversion for the considered operational parameters. This again shows the kinetic limitation of the chosen manganese-iron oxide.
- A sensitivity analysis showed that the potential development of channels within the moving bulk material would lower the heat transfer between solid and gas. Without consideration of channeling effects, a bed height of 20 cm would be sufficient to cool down the particle flow from 1050 °C to 300 °C with a suitable gas flow. However, if channeling effects occur, the required bed height increases up to 70 cm.

Future work will comprise an experimental investigation of the proposed reactor concept for the discharging step based on metal-oxide particles applied as thermochemical storage material and a heat transfer medium. Besides material specific parameters, such as kinetics and agglomeration, the thermal power is mainly influenced by the process control. A coupling of direct and indirect heat transfer constitutes a promising operational mode.

Author Contributions: Conceptualization, N.C.P. and M.L.; methodology, N.C.P. and I.B.; software, I.B.; validation, N.C.P., M.W. and I.B.; formal analysis, N.C.P.; investigation, N.C.P.; resources, N.C.P.; data curation, N.C.P. and M.W.; writing—original draft preparation, N.C.P.; writing—review and editing, I.B., M.W., and M.L.; visualization, N.C.P. and M.W.; supervision, M.L.; project administration, M.L.; funding acquisition, M.L. All authors have read and agreed to the published version of the manuscript.

Funding: This research received no external funding.

Acknowledgments: The authors wish to thank Henrik Winnemöller (Johannes Gutenberg University Mainz, Mainz) for proofreading. We further thank Matthias Schmidt and Kai Risthaus for intellectual discussions.

Conflicts of Interest: The authors declare no conflict of interest.

Appendix A. Specific Heat Capacity

The specific heat capacity determines the energy density for a sensible thermal energy storage material, and is thus a crucial thermophysical property for choosing a thermal energy storage material. In Figure A1, specific heat capacity data of the pure metal oxides Mn_2O_3 and Mn_3O_4 (literature data [23]) are compared to values for the mixed manganese-iron oxide measured by means of DSC.

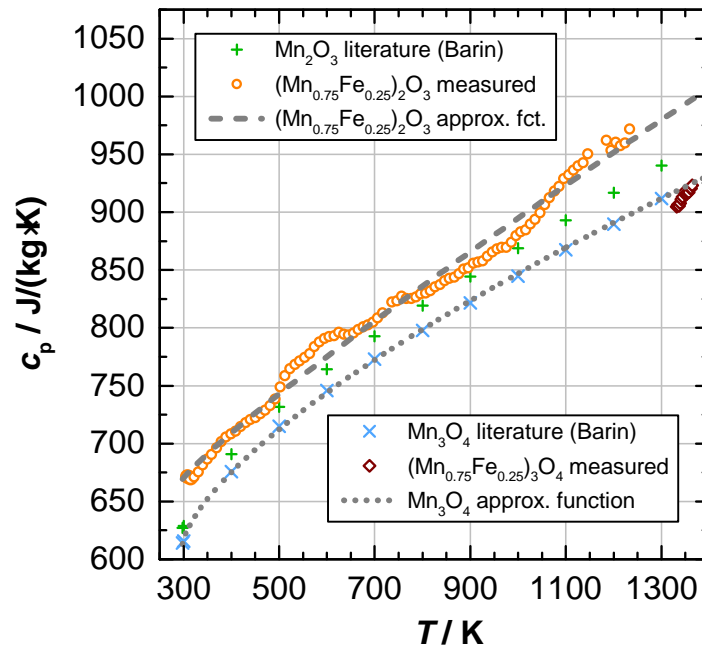


Figure A1. Specific heat capacity of manganese-iron oxide: Measured and approximated values for $(\text{Mn}_{0.75}\text{Fe}_{0.25})_2\text{O}_3$ and $(\text{Mn}_{0.75}\text{Fe}_{0.25})_3\text{O}_4$.

As the manganese-iron oxide represents a novel compound with a different lattice structure compared to iron oxide, the specific heat capacities of the mixed oxide cannot be calculated from the specific heat capacities of the respective single oxides Mn_2O_3 and Fe_2O_3 for the oxidized phase and Mn_3O_4 and Fe_3O_4 for the reduced phase of Mn-Fe-oxide, respectively. Therefore, the specific heat capacities $c_{p,ox}$ and $c_{p,red}$ of the binary oxide were measured by means of DSC. At first, the samples were prepared by pestling the granules to powder and afterward compressing the powder to pellets (85.0 mg and 91.3 mg). The compressed pellets were calcined at 950 °C for 10 h in air prior to the measurements. Finally, the pellets were heated in a Pt/Rh-crucible with a pierced lid from 30 °C up to 1200 °C with 10 K/min in an air flow of 50 mL/min (norm condition). Using a baseline measurement, a sensitivity calibration measurement with a sapphire disc of known c_p -values and the actual sample measurement, the unknown c_p -values of Mn-Fe oxide can be evaluated based on a comparative method. Between ~400 K and ~1000 K, the measured values of the oxidized phase are in the range of the pure manganese oxide Mn_2O_3 . However, above ~1050 K the measured values exceed the pure metal oxide data. The curve of measured values for the oxidized phase can be best approximated with a power equation:

$$c_{p,ox}(T) = \left(669.28596 + 0.62604 \left(\frac{T}{K} - 298 \right)^{0.8982} \right) \text{ J/kg/K.} \quad (\text{A1})$$

After a complete reduction, only a few values were obtained for the reduced phase $(\text{Mn}_{0.75}\text{Fe}_{0.25})_3\text{O}_4$. Nevertheless, they are in the range of the pure manganese oxide Mn_3O_4 . The specific heat capacity of the reduced phase is approximated using the literature data for Mn_3O_4 :

$$c_{p,red}(T) = \left(613.07996 + 2.58034 \left(\frac{T}{K} - 298 \right)^{0.68764} \right) \text{ J/kg/K.} \quad (\text{A2})$$

Appendix B. Experiment for Model Validation

In the fixed-bed experiment for validation, manganese-iron-oxide particles were cooled by a gas flow of 10 L/min (norm condition). The temperatures of the gas at the inlet of the reaction bed and the

temperature of the tube furnace, which enclosed the fixed-bed reactor, were decreased by 5 K/min. In Figure A2, the gas inlet temperature and the temperatures of the bulk and the reactor tube wall, the latter measured on the outer surface of the tube, are displayed for the first 15 min of the experiment.

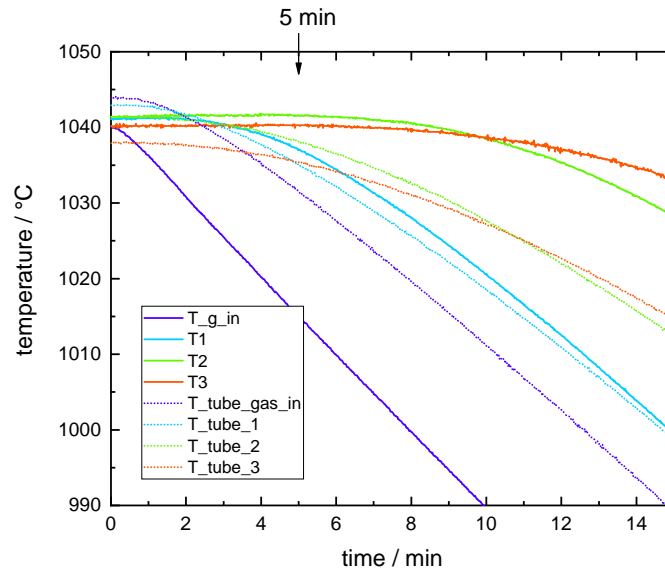


Figure A2. Temperatures of the gas, bulk material, and outer reactor tube wall during the first 15 min of the fixed-bed discharging experiment for the validation of the simulation. The position of the tube temperatures corresponds to the same height of the bulk temperature in the radial direction.

The temperatures of the reactor wall (dotted line) and the bulk temperatures (solid line) indicate a delay time until the effect of the decrease in temperature of the gas flow and tube furnace is measurable. Thus, it is assumed that the thermal mass of the reactor tube acts as a thermal buffer for the temperature decrease in the experiment during the first minutes of the experiment. However, no thermal mass is included in the simulation. For better comparison of the cooling rate of the bulk, and the temperature plateau position and length, the simulation was shifted by 5 min.

Appendix C. Initial Design of a 3 kW Moving Bed Reactor

A common way to design heat exchangers is via the NTU method (number of transfer units), where the capacity flows of solid and gas are compared [33]. For designing a heat exchanger, the characteristic numbers P_i , NTU_i , and ϑ indicate the influence of different fluid flow feed (counter-current, co-current, stirred vessel, etc.) on the exchanged power:

$$P_i = \frac{\dot{Q}}{(\dot{m}c_p)_i (T_{i,in} - T_{j,out})} = \frac{kA}{(\dot{m}c_p)_i} \frac{\Delta T_M}{(T_{i,in} - T_{j,out})}. \quad (A3)$$

Here, \dot{Q} denotes the thermal power of the heat exchanger, and $P_i = NTU_i \cdot \vartheta$ the dimensionless temperature change with $\vartheta = \frac{\Delta T_M}{(T_{i,in} - T_{j,out})}$ and the logarithmic temperature difference ΔT_M based on the maximal temperature difference. The desired thermal power is set to 3 kW for initial calculations, and the heat exchanger is divided into three sections (see Figure 2b). The necessary solid and air flows are calculated according to an idealized convective heat transfer between gas and solid particles. The thermochemical section ($q_{\Delta H}$) is assumed to be isothermal at 895 °C, which is the onset temperature for the oxidation of $(\text{Mn}_{0.75}\text{Fe}_{0.25})_2\text{O}_3$, determined for a cooling rate of 10 K/min [6]. Thermogravimetric measurements of our group [6] show that the particles should stay at least 15 min in the thermochemical section in order to be fully oxidized. Furthermore, it is assumed that the reduced manganese-iron-oxide particles enter the moving bed at 1050 °C and exit the reactor at a desired

particle outlet temperature of 350 °C. An air inlet temperature of 300 °C is chosen for a calculation of an achievable air outlet temperature. The air flow is limited to air velocities below the fluidization velocity [34]. Furthermore, a temperature difference of 2 K is assumed between gas and solid, when the air flow exits the thermochemical section $q_{\Delta H}$. The necessary particle mass flow for a thermal power of 3 kW can be determined with

$$\dot{m}_s = \frac{3 \text{ kW}}{q_{red} + q_{\Delta H} + q_{ox}} \quad (\text{A4})$$

to 4 g/s based on the reduced phase of manganese-iron oxide. Here, the heat transfer of each section is calculated with the specific heat capacity of Mn_2O_3 and Mn_3O_4 [23] as, e.g., $dq_{red} = \int_{895^\circ\text{C}}^{1050^\circ\text{C}} c_{p,s}(T_s) dT_s$. In the thermochemical section, the specific reaction enthalpy of 271 J/g based on the oxidized phase results in a heat transfer $q_{\Delta H}$. The required air flow is calculated by considering the heat transfer in the sensible section q_{ox} and thermochemical section $q_{\Delta H}$. With the assumption that the air stream leaves the thermochemical section with a temperature difference of 2 K, the supplied heat of the solid phase can be determined with $q_{ox} + q_{\Delta H}$ resulting in:

$$\dot{m}_g = \frac{\dot{Q}_{ox} + \dot{Q}_{\Delta H}}{\int_{300^\circ\text{C}}^{893^\circ\text{C}} c_{p,g}(T) dT_g} = 4 \text{ g/s}. \quad (\text{A5})$$

This mass flow rate is above the minimal air flow of 0.5 g/s, which is required to provide enough oxygen for a full oxidation of 4 g/s manganese-iron-oxide particle flow. With fixed mass flow rates of gas and solid particles, the gas and solid temperatures at each border between the three sections can be calculated. In the end, a gas outlet temperature of 998 °C can be expected for the ideal case. As a result, the thermochemical share in transferred heat equals 31%.

The dimension of each section is determined with the assumption of ideal convective heat transfer according to Yang et al. [22]. For each section h_{gs} is calculated with a logarithmic temperature

$$\vartheta_m = \frac{\Delta T_{in} - \Delta T_{out}}{\ln\left(\frac{\Delta T_{in}}{\Delta T_{out}}\right)} \quad (\text{A6})$$

for inner diameters of the moving bed reactor between 10 mm and 220 mm. The convective heat transfer $Q = h_{gs} \cdot a_{gs} \cdot \Delta T$ yields the required particle surface to transfer the desired heat, and thus the reactor height h_R in relation to reactor diameter d_R and particle size d_p with $a_{gs} = \frac{3\pi d_R^2 h_R (1-\epsilon_b)}{2d_p}$. In the end, a reactor height of 700 mm and a diameter of 0.152 m for an average particle diameter of 2.5 mm were chosen to assure both sensible and thermochemical heat transfer without fluidizing the particles.

References

1. Pardo, P.; Deydier, A.; Anxionnaz-Minvielle, Z.; Rougé, S.; Cabassud, M.; Cognet, P. A review on high temperature thermochemical heat energy storage. *Renew. Sustain. Energy Rev.* **2014**, *32*, 591–610. doi:10.1016/j.rser.2013.12.014. [CrossRef]
2. Wu, S.; Zhou, C.; Doroodchi, E.; Nellore, R.; Moghtaderi, B. A review on high-temperature thermochemical energy storage based on metal oxides redox cycle. *Energy Convers. Manag.* **2018**, *168*, 421–453. doi:10.1016/j.enconman.2018.05.017. [CrossRef]
3. Block, T.; Schmücker, M. Metal oxides for thermochemical energy storage: A comparison of several metal oxide systems. *Sol. Energy* **2016**, *126*, 195–207. doi:10.1016/j.solener.2015.12.032. [CrossRef]
4. André, L.; Abanades, S.; Flamant, G. Screening of thermochemical systems based on solid-gas reversible reactions for high temperature solar thermal energy storage. *Renew. Sustain. Energy Rev.* **2016**, *64*, 703–715. doi:10.1016/j.rser.2016.06.043. [CrossRef]
5. Wokon, M.; Kohzer, A.; Linder, M. Investigations on thermochemical energy storage based on technical grade manganese-iron oxide in a lab-scale packed bed reactor. *Sol. Energy* **2017**, *153*, 200–214. doi:10.1016/j.solener.2017.05.034. [CrossRef]

6. Wokon, M.; Block, T.; Nicolai, S.; Linder, M.; Schmücker, M. Thermodynamic and kinetic investigation of a technical grade manganese-iron binary oxide for thermochemical energy storage. *Sol. Energy* **2017**, *153*, 471–485. doi:10.1016/j.solener.2017.05.045. [\[CrossRef\]](#)
7. Chen, C.; Lee, H.H.; Chen, W.; Chang, Y.C.; Wang, E.; Shen, C.H.; Huang, K.E. Study of an Iron-Based Oxygen Carrier on the Moving Bed Chemical Looping System. *Energy Fuels* **2018**, *32*, 3660–3667. doi:10.1021/acs.energyfuels.7b03721. [\[CrossRef\]](#)
8. Zeng, L.; Tong, A.; Kathe, M.; Bayham, S.; Fan, L.S. Iron oxide looping for natural gas conversion in a countercurrent moving bed reactor. *Appl. Energy* **2015**, *157*, 338–347. doi:10.1016/j.apenergy.2015.06.029. [\[CrossRef\]](#)
9. Tong, A.; Zeng, L.; Kathe, M.V.; Sridhar, D.; Fan, L.S. Application of the Moving-Bed Chemical Looping Process for High Methane Conversion. *Energy Fuels* **2013**, *27*, 4119–4128. doi:10.1021/ef3020475. [\[CrossRef\]](#)
10. Yanagiya, T.; Yagi, J.; Omori, Y. Reduction of iron oxide pellets in moving bed. *Ironmak. Steelmak.* **1979**, *6*, 93–100.
11. Takenaka, Y.; Kimura, Y. Mathematical model of direct reduction shaft furnace and its application to actual operations of a model plant. *Comput. Chem. Eng.* **1986**, *10*, 67–75. [\[CrossRef\]](#)
12. Parisi, D.R.; Laborde, M.A. Modeling of counter current moving bed gas-solid reactor used in direct reduction of iron ore. *Chem. Eng. J.* **2004**, *104*, 35–43. doi:10.1016/j.cej.2004.08.001. [\[CrossRef\]](#)
13. Ghalandari, V.; Rafsanjani, H.H. Mathematical Modeling and Simulation of Direct Reduction of Iron Ore in a Moving Bed Reactor by the Single Particle Model. *Chem. Chem. Technol.* **2019**, *13*, 205–211. doi:10.23939/chcht13.02.205. [\[CrossRef\]](#)
14. Negri, E.D.; Alfano, O.M.; Chiovetta, M.G. Moving-Bed Reactor Model for the Direct Reduction of Hematite. Parametric Study. *Ind. Eng. Chem. Res.* **1995**, *34*, 4266–4276. doi:10.1021/ie00039a017. [\[CrossRef\]](#)
15. Valipour, M.S.; Saboohi, Y. Numerical investigation of nonisothermal reduction of hematite using Syngas: The shaft scale study. *Model. Simul. Mater. Sci. Eng.* **2007**, *15*, 487–507. doi:10.1088/0965-0393/15/5/008. [\[CrossRef\]](#)
16. Rahimi, A.; Niksiar, A. A general model for moving-bed reactors with multiple chemical reactions part I: Model formulation. *Int. J. Miner. Process.* **2013**, *124*, 58–66. doi:10.1016/j.minpro.2013.02.015. [\[CrossRef\]](#)
17. Kim, H.; Miller, D.C.; Modekurti, S.; Omell, B.; Bhattacharyya, D.; Zitney, S.E. Mathematical modeling of a moving bed reactor for post-combustion CO₂ capture. *AIChE J.* **2016**, *62*, 3899–3914. doi:10.1002/aic.15289. [\[CrossRef\]](#)
18. Preisner, N.C.; Block, T.; Linder, M.; Leon, H. Stabilizing Particles of Manganese-Iron Oxide with Additives for Thermochemical Energy Storage. *Energy Technol.* **2018**, *6*, 2154–2165. doi:10.1002/ente.201800211. [\[CrossRef\]](#)
19. Nield, D.A.; Bejan, A. *Convection in Porous Media*; Springer International Publishing: Cham, Switzerland, 2017. doi:10.1007/978-3-319-49562-0. [\[CrossRef\]](#)
20. Bauer, R.; Schlünder, E.U. Effective radial thermal conductivity of packings in gas flow. *Int. Chem. Eng.* **1978**, *18*, 189–204.
21. Zehner, P.; Schlünder, E.U. Einfluß der Wärmestrahlung und des Druckes auf den Wärmetransport in nicht durchströmten Schüttungen. *Chem. Ingenieur Technol.* **1972**, *44*, 1303–1308 [\[CrossRef\]](#)
22. Yang, W.; Zhou, Z.; Yu, A. Particle scale studies of heat transfer in a moving bed. *Powder Technol.* **2015**, *281*, 99–111. doi:10.1016/j.powtec.2015.04.071. [\[CrossRef\]](#)
23. Barin, I.; Platzki, G. *Thermochemical Data of Pure Substances*, 3rd ed.; VCH Verlagsgesellschaft mbH: Weinheim, Germany, 1995. doi:10.1002/9783527619825. [\[CrossRef\]](#)
24. Ksiazek, M.; Manik, T.; Tangstad, M.; Ringdalen, E. The thermal diffusivity of raw materials for ferromanganese production. In Proceedings of the INFACON International Ferro-Alloys Congress, Almaty, Kazakhstan, 9–12 June 2013.
25. Palacios, A.; Calderón, A.; Barreneche, C.; Bertomeu, J.; Segarra, M.; Fernández, A.I. Study on solar absorptance and thermal stability of solid particles materials used as TES at high temperature on different aging stages for CSP applications. *Sol. Energy Mater. Sol. Cells* **2019**, *201*, 110088. [\[CrossRef\]](#)
26. Wang, H.; Ning, X.; Wang, Q.; Liu, Y.; Song, Y. Preparation and properties of high emissivity Fe–Mn–matrix coatings by air plasma spraying. *Mater. Res. Innov.* **2015**, *19*, S29–S33. [\[CrossRef\]](#)
27. Kunii, D.; Suzuki, M. Particle-to-fluid heat and mass transfer in packed beds of fine particles. *Int. J. Heat Mass Transf.* **1967**, *10*, 845–852. doi:10.1016/0017-9310(67)90064-6. [\[CrossRef\]](#)

28. Wu, S.; Zhou, C.; Doroodchi, E.; Moghtaderi, B. A unique phase change redox cycle using CuO/Cu₂O for utility-scale energy storage. *Energy Convers. Manag.* **2019**, *188*, 366–380. doi:10.1016/j.enconman.2019.03.055. [[CrossRef](#)]
29. Schrader, A.J.; Muroyama, A.P.; Loutzenhiser, P.G. Solar electricity via an Air Brayton cycle with an integrated two-step thermochemical cycle for heat storage based on Co₃O₄/CoO redox reactions: Thermodynamic analysis. *Sol. Energy* **2015**, *118*, 485–495. doi:10.1016/j.solener.2015.05.045. [[CrossRef](#)]
30. Muroyama, A.P.; Schrader, A.J.; Loutzenhiser, P.G. Solar electricity via an Air Brayton cycle with an integrated two-step thermochemical cycle for heat storage based on Co₃O₄/CoO redox reactions II: Kinetic analyses. *Sol. Energy* **2015**, *122*, 409–418. doi:10.1016/j.solener.2015.08.038. [[CrossRef](#)]
31. Carrillo, A.J.; Serrano, D.P.; Pizarro, P.; Coronado, J.M. Understanding Redox Kinetics of Iron-Doped Manganese Oxides for High Temperature Thermochemical Energy Storage. *J. Phys. Chem. C* **2016**, *120*, 27800–27812. doi:10.1021/acs.jpcc.6b08708. [[CrossRef](#)]
32. Bush, H.E.; Loutzenhiser, P.G. Solar electricity via an Air Brayton cycle with an integrated two-step thermochemical cycle for heat storage based on Fe₂O₃/Fe₃O₄ redox reactions: Thermodynamic and kinetic analyses. *Sol. Energy* **2018**, *174*, 617–627. doi:10.1016/j.solener.2018.09.043. [[CrossRef](#)]
33. VDI-Wärmeatlas; Springer: Berlin/Heidelberg, Germany, 2013. doi:10.1007/978-3-642-19981-3. [[CrossRef](#)]
34. Wen, C.Y.; Yu, Y.H. A Generalized Method for Predicting the Minimum Fluidization Velocity. *AIChE J.* **1966**, *12*, 610–612. [[CrossRef](#)]




© 2020 by the authors. Licensee MDPI, Basel, Switzerland. This article is an open access article distributed under the terms and conditions of the Creative Commons Attribution (CC BY) license (<http://creativecommons.org/licenses/by/4.0/>).

2.4 Paper III

Article

A Moving Bed Reactor for Thermochemical Energy Storage Based on Metal Oxides

Nicole Carina Preisner ^{1,*}  and Marc Linder ²¹ Institute of Engineering Thermodynamics, DLR, Linder Höhe, 51147 Köln, Germany² Institute of Engineering Thermodynamics, DLR, Pfaffenwaldring 38–40, 70569 Stuttgart, Germany; marc.linder@dlr.de

* Correspondence: nicole.preisner@dlr.de

Received: 4 February 2020; Accepted: 1 March 2020; Published: 6 March 2020



Abstract: High-temperature thermal energy storage enables concentrated solar power plants to provide base load. Thermochemical energy storage is based on reversible gas–solid reactions and brings along the advantage of potential loss-free energy storage in the form of separated reaction products and possible high energy densities. The redox reaction of metal oxides is able to store thermal energy at elevated temperatures with air providing the gaseous reaction partner. However, due to the high temperature level, it is crucial to extract both the inherent sensible and thermochemical energies of the metal-oxide particles for enhanced system efficiency. So far, experimental research in the field of thermochemical energy storage focused mainly on solar receivers for continuously charging metal oxides. A continuously operated system of energy storage and solar tower decouples the storage capacity from generated power with metal-oxide particles applied as heat transfer medium and energy storage material. Hence, a heat exchanger based on a countercurrent moving bed concept was developed in a kW-scale. The reactor addresses the combined utilization of the reaction enthalpy of the oxidation and the extraction of thermal energy of a manganese–iron-oxide particle flow. A stationary temperature profile of the bulk was achieved with two distinct temperature sections. The oxidation induced a nearly isothermal section with an overall stable off-gas temperature. The oxidation and heat extraction from the manganese–iron oxide resulted in a total energy density of 569 kJ/kg with a thermochemical share of 21.1%.

Keywords: moving bed; thermochemical energy storage; metal oxide

1. Introduction

A thermochemical energy storage (TCS) is able to complement concentrated solar thermal power plants (CSP) to allow for renewable base load supply. The principle of thermochemical energy storage is based on a chemically reversible gas–solid reaction. The thermal energy is either released in the form of reaction enthalpy (discharging), absorbed by the reverse endothermic reaction (charging), or stored in the chemical bond by the separation of the gas and solid phases. Thermochemical energy storage features high energy densities in comparison to other thermal energy storage concepts, i.e., sensible thermal energy storage or thermal energy storage based on a phase change [1,2]. Metal oxides are a suitable candidate for thermochemical energy storage for CSP, since the redox reaction of metal oxides occurs at elevated temperatures [3,4], which are necessary to reach high efficiencies. Furthermore, ambient air can provide the gaseous reaction partner, which simplifies gas handling in comparison to other TCS material systems. Therefore, the considered system (Figure 1) is based on metal-oxide particles as thermochemical energy storage material and heat transfer medium to expand the CSP operation time into evening hours or to compensate weather instability.

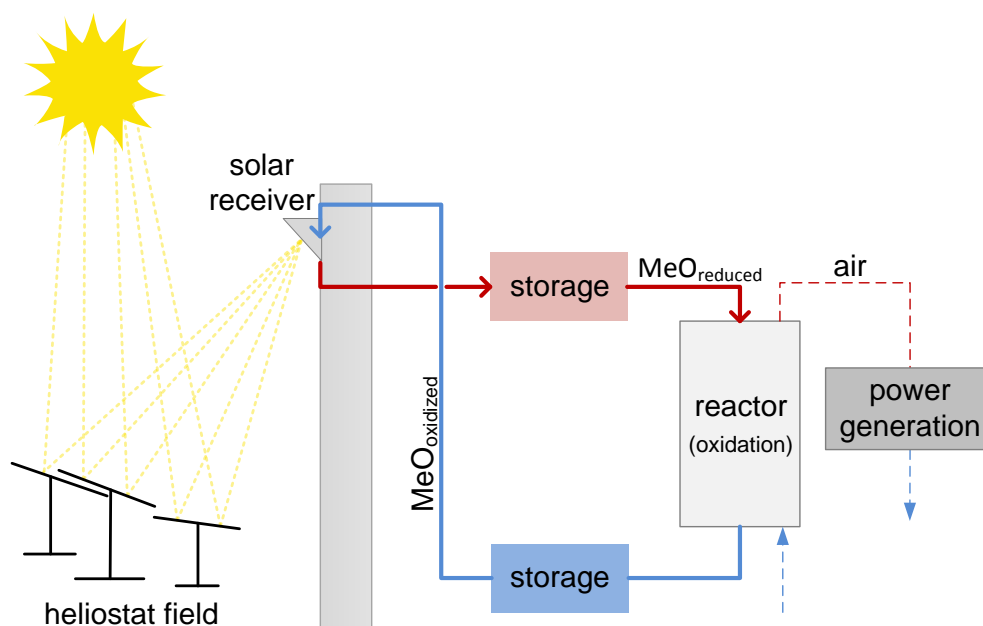


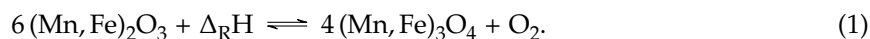
Figure 1. Concept of thermal energy storage based on metal-oxide particles for solar tower applications, including a high-temperature and low-temperature storage tank for decoupling of the system capacity and thermal power output.

The concept enables the decoupling of storage capacity and system power due to the continuously working heat exchanger and solar receiver and to the storage tanks in between. The metal-oxide particles are reduced by supplying concentrated solar irradiation until temperatures exceed the reduction onset temperature of the applied metal oxide. After an intermediate high-temperature storage tank, the discharging is performed in a separate reactor, optimized for oxidation. The particle loop is closed when the material is transported via an intermediate low-temperature storage tank back to the solar tower. Thus, a sufficient flowability of the metal-oxide particles is essential to implement the presented system concept. Schrader et al. [5] suggested a similar concept for thermochemical energy storage, where cobalt oxide is applied under pressurized conditions in a closed system. In addition, the utilization of particles as heat transfer and thermal storage material has been also investigated for sensible energy storage [6–8]. Owing to the high temperature level in the solar receiver, it is crucial to extract both the thermochemical energy and inherent sensible energy of the metal-oxide particles in the heat extraction reactor to enhance the total energy density and system efficiency.

The concept of combined extraction of sensible and thermochemical energy has been also suggested for inert honeycomb structures coated with a thermochemical energy storage material [9] and for the oxidation of CoO and subsequent cooling in pressurized air [5]. Furthermore, a solar-driven cycle based on copper oxide was proposed, where sensible, latent, and thermochemical energy of the metal oxide is extracted for high-temperature power generation and oxygen production [10]. In general and almost independent from the concept, the metal-oxide particles should meet several criteria for long-term utilization in the suggested continuous concept: sufficient mechanical strength, resistance of particle stability towards chemical and thermal stress, adequate chemical reversibility of redox reaction, high reaction enthalpy and heat capacity for enhanced energy density, affordable raw material cost, and low environmental impact due to the open system concept.

Recent work on metal oxides for the application as thermochemical energy storage includes binary metal oxides like $\text{Co}_3\text{O}_4/\text{CoO}$ [11] or perovskites like $\text{CaMnO}_{3-\delta}$ [12]. Furthermore, mixed metal oxides have been in focus lately, e.g., Mn–Fe oxides [13–16], Co–Mn oxides [17], and Co–Fe oxides [15,18]. The replacement of a primary oxide cation with a secondary cation can enhance the redox kinetics

and cycle stability in comparison to pure metal oxides [19]. For this work, manganese–iron oxide was chosen as a reference material to investigate the combined heat extraction of sensible and thermochemical energy. Phase diagrams of Mn–Fe oxides for ambient air condition predict a phase change between bixbyite $(\text{Mn, Fe})_2\text{O}_3$ and spinel phase $(\text{Mn, Fe})_3\text{O}_4$ for the considered Mn/(Mn + Fe) ratio of 0.7 via one or several two-phase regions [15,20–24]. Thus, the redox reaction follows the equation as below:



However, agglomeration of manganese–iron-oxide particles was reported, which could hinder the bulk movement in the considered continuous concept [25,26]. Consequently, we have investigated different supporting materials to improve the particle stability of manganese–iron oxide [26]. The addition of 20 wt.% ZrO_2 was found to enhance mechanical stability and to inhibit agglomeration. Manganese–iron-oxide particles are thus a promising candidate for a continuously operated system, and for this reason they were chosen for the system presented.

So far, solar receivers for metal-oxide reduction are mainly based on the rotary kiln concept [27–29] or applied as fluidized bed [30], packed bed reactor [31], and gravity-driven particle receivers [32–34]. The rotary-kiln concept already achieved wall temperatures up to 1000 °C in solar simulators [27,28]. A continuously operated particle receiver is favorable for CSP to allow for high mass flow rates, sufficient heat transfer between gas and solid phase, as well as decreased possible sintering effects [28]. Furthermore, a continuously working solar receiver needs to be heated up only once, which improves the thermal efficiency of the system. The oxidation of metal oxides for thermochemical storage application was investigated with packed bed reactors [19,25] and a fluidized bed reactor [35]. These reactors are suitable for the oxidation of metal oxides but do not allow for a continuous metal-oxide flow. However, this criterion is a basic requirement to realize the suggested system concept of Figure 1. Therefore, this work focuses on the heat extraction from metal-oxide particles in a continuously operated reactor.

In general, a circulating fluidized bed, flash reactor, moving bed reactor, or reactor with mechanical particle transport, e.g., rotary kiln or sintering band, is applicable for direct heat transfer from a continuous solid flow to a gas flow. In addition, the heat exchanger needs to ensure a particle residence time in the range of several minutes at temperatures suitable for oxidation according to a kinetic analysis of manganese–iron oxides with a similar cation ratio [14,16]. Furthermore, criteria like the ability to handle possible volume changes of the particles due to the reaction, heat transfer between gas and solid, possibility to extract thermochemical and sensible energy, and parasitic loss were taken into account.

The moving bed reactor concept has the advantage of low mechanical stress for the particles, low parasitic loss, no moving reactor parts, and a simple possibility to combine the utilization of sensible and thermochemical energy. The moving bed concept is also applied in an industrial scale, e.g., for a cooling cement clinker [36] or for the direct reduction of hematite to produce sponge iron [37,38]. In addition, the moving bed concept is used in chemical-looping combustion (CLC), where metal-oxide particles act as oxygen carriers to oxidize fuels in an oxygen-free atmosphere and reoxidize in air [39–41]. However, no continuously operated reactor for non-isothermal oxidation of metal oxides has been reported so far. Therefore, in this work, a moving bed reactor was designed for direct heat transfer between a metal-oxide particle flow in countercurrent to a gas flow for the discharging step of the system concept presented in Figure 1. Since an extraction of thermal energy leads naturally to a temperature decrease, the reaction rate of the thermochemical material is affected. Therefore, the influence of the reaction enthalpy release on the temperature profile of a stationary working moving bed reactor is investigated. Furthermore, the suitability of manganese–iron-oxide particles acting as a heat transfer material and thermal storage medium is explored.

2. Materials and Methods

2.1. Materials

The preparation of the manganese–iron-oxide particles was performed by VITO (Mol, Belgium) via build-up granulation, analogous to the procedure for metal-oxide particles in [16]. The raw materials Mn_3O_4 (Trimanox, Chemalloy), Fe_2O_3 (98% metal basis, Alfa Aesar), and ZrO_2 (99.9% ZrO_2 + HfO_2 , Saint Gobain) are mixed in powder form. A Mn/(Mn + Fe) ratio of 0.7 was chosen based on previous studies concerning cycle stability and reaction enthalpy [3,13,16]. The particles were heat treated for 10 h at 800 °C to obtain a bixbyite phase $(\text{Mn}, \text{Fe})_2\text{O}_3$ and sieved to a size between 2 mm and 3 mm. The obtained metal oxide is denoted $(\text{Mn}_{0.7}\text{Fe}_{0.3})_2\text{O}_3$ in the following. Based on our previous work, an addition of 20 wt.% ZrO_2 was chosen to improve particle stability and to inhibit agglomeration [26]. The material properties are summarized in Table 1.

Table 1. Material parameters of the manganese–iron-oxide particles.

Parameter	Symbol	Value/Correlation	Unit	Reference
Particle diameter	d_p	2–3	mm	as received
Bulk density	ρ_{bulk}	1400	kg/m ³	measured
Reaction enthalpy, based on oxidized phase	$\Delta_r H$	188	J/g	measured
Specific heat capacity of $(\text{Mn}_{0.7}\text{Fe}_{0.3})_2\text{O}_3$ + 20% ZrO_2 (30 °C to 580 °C)	$c_{p_{\text{ox}}}$	$427.76224 + 72.1084(\frac{T_i}{K} - 273.15)^{0.24307}$	J/kg/K	measured
True density of $(\text{Mn}_{0.7}\text{Fe}_{0.3})_2\text{O}_3$ + 20% ZrO_2	ρ_s	5204	kg/m ³	measured via He-pycnometry
Total porosity	ϵ	0.73	—	calculated
Bulk porosity	ϵ_b	0.48	—	calculated
Intra-particle porosity	ϵ_{por}	0.48	—	measured via Hg-intrusion-porosimetry

The bulk density of $1400 \text{ kg/m}^3 \pm 18 \text{ kg/m}^3$ was measured by filling and weighing a 250 mL cylinder. The effective onset temperature of reduction and oxidation was determined by means of thermogravimetric analysis (TGA) (STA 449 F3 Jupiter, Netzsch). Two metal-oxide particles with a total weight of around 30 mg were reduced and oxidized in an atmosphere of 20% oxygen (5.0) in nitrogen (5.0) by applying heating rates of 1, 5, 10, 20, or 30 K/min. The onset temperatures of each experiment were extrapolated with cubic spline method to null K/min for oxidation and reduction. The reaction enthalpy was examined with differential scanning calorimetry (DSC) for the oxidation applying heating rates of 10, 20, or 30 K/min at an oxygen partial pressure of 20 kPa. Based on the composite material in the oxidized phase, a reaction enthalpy of $188 \text{ J/g} \pm 8 \text{ J/g}$ was identified by taking the mean of the second to fourth cycle of each heating rate experiment. The value is in line with measurements in literature for $(\text{Mn}_x\text{Fe}_{1-x})_2\text{O}_3$ with a Mn/(Mn + Fe) ratio x of $x = 0.792$ (203 J/g [13]), $x = 0.75$ (271 J/g [16]), and $x = 0.67$ (162 J/g [3]). The specific heat capacity was measured in a temperature range of 30 °C to 580 °C by means of dynamic scanning calorimetry (DSC 204 F1 Phoenix, Netzsch). A heating and cooling rate of 10 K/min was applied with a nitrogen flow passing the pestled sample of $(\text{Mn}_{0.7}\text{Fe}_{0.3})_2\text{O}_3$ in a Pt/Rh crucible. Furthermore, a long time stability of the redox reaction was tested for 60 cycles in TGA. The mass loss indicated no decline during consecutive cycling (see Appendix A). More detailed properties related to particle stability of the applied manganese–iron-oxide compound can be found in Reference [26].

The reactor was never completely filled with metal-oxide particles. Sintered bauxite (type 30/50, Saint Gobain Proppants in USA) was selected as filling material for unheated reactor parts during the reduction of the manganese–iron-oxide particles. The sintered bauxite particles have an average

diameter of 0.47 mm and a bulk density of 2040 kg/m³. The effect of sintered bauxite on the reactivity of manganese–iron oxide was investigated during 30 redox cycles performed with TGA. For this analysis, the manganese–iron oxide was pestled and mixed with sintered bauxite particles. The sample was cycled in a Pt/Rh crucible without a lid between 850 °C and 1050 °C in a 100 mL/min gas stream with 20 vol % O₂ and nitrogen 5.0 as residual. The mass loss and gain due to the redox reaction stayed stable for all 30 cycles, and no side reactions were visible.

2.2. Experimental Setup

A reactor for direct heat exchange between a particle stream and air stream was designed based on a moving bed concept. The air stream flows in countercurrent to a moved particle bed, leading to a continuous heat transfer of inherent sensible and thermochemical energy. The gas stream provides O₂ for the reaction and would potentially act as heat transfer fluid to, e.g., a subsequent power generation cycle. The three functional sections of the reactor are displayed in Figure 2a.

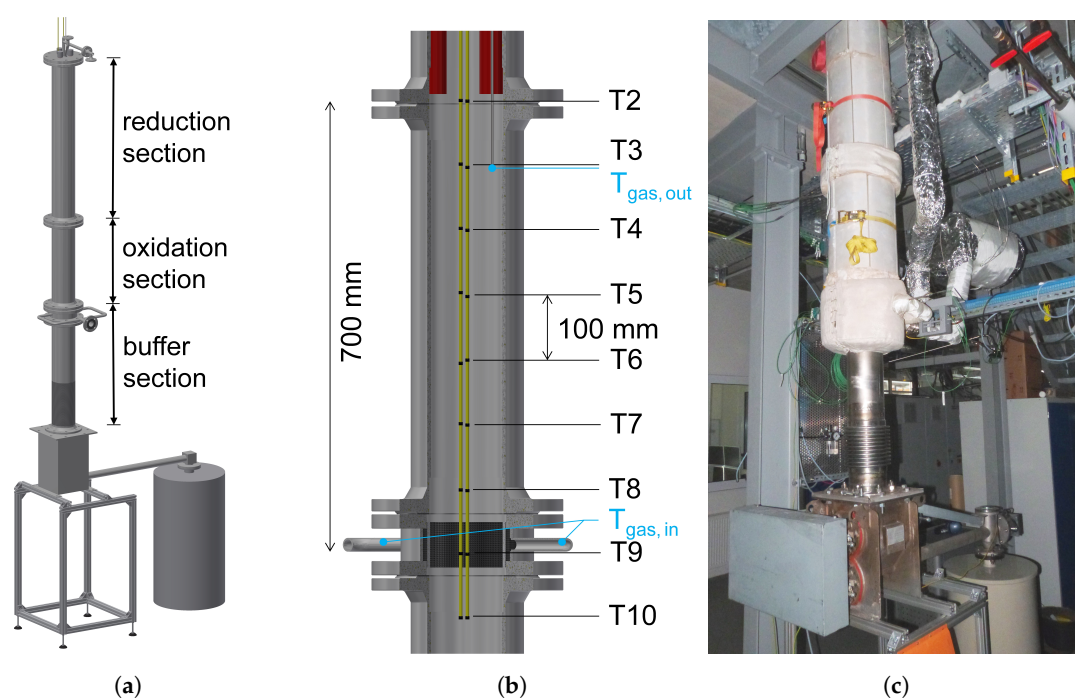


Figure 2. (a) Schematic of the reactor setup. (b) Close-up of the oxidation section with temperature measurement points. (c) Picture of assembled reactor.

Although the reactor is designed for the discharging of the metal-oxide particles, the upper reactor section, i.e., reduction section, corresponds to the solar receiver of the concept displayed in Figure 1. Three heating elements (Multicell, Watlow) inside the reactor tube (inner Ø: 152.3 mm) ensure a bed temperature above the reduction temperature of the applied metal-oxide particles. The heating elements are distributed centrosymmetrically to allow for homogeneous axial temperature distribution and are temperature regulated at three individual height sections to compensate the unequally distributed thermal losses in the reduction section. During the charging step, the whole metal-oxide bulk rests in the reduction section as a fixed bed on top of the filling material (sintered bauxite) in the residual reactor. The heat transfer between solid and gas is investigated in the oxidation section below the reduction section with moving bed conditions. High temperature-resistant wool and microporous silica isolation in height of the reduction and oxidation section reduces heat transfer to the environment. Two multipoint-thermocouples (type K, class 1, total Ø: 5 mm) are installed to measure the bulk temperature along the bed height at 9 levels every 100 mm in central and half radial position in the oxidation section (see Figure 2b) and at a central height in the reduction section.

The multipoint-thermocouples are composed of thermo wires embedded in MgO to reduce thermal conductivity between the measurement points and a 0.6 mm thin steel shell (nickel-based alloy 2.4816). The gas enters the reactor from two sides through a double-walled cylinder below the oxidation section. A filter (0.18 mm mesh size) prevents the particles from penetrating the gas tube system. The inlet gas temperature is analyzed with a thermocouple (\varnothing : 3 mm) in each gas inlet tube. The average temperature of both gas inlet flows is referred to as gas inlet temperature in later experiments. The gas is led through heated tubes or a separate gas heater for higher gas temperatures to preheat the gas to a set temperature at the inlet of the reactor. The off-gas temperature is analyzed by a thermocouple (\varnothing : 1 mm) enclosed in an open tube (\varnothing : 4 mm) at level T3 (see Figure 2b), which is connected to a pump of the gas analyzer. A small gas stream ($<201/h$) flows through the tube to the gas analyzer for oxygen measurement and improvement of heat transfer between gas flow and thermocouple. A screw conveyor regulates the particle volume flow at the bottom of the reactor to attain a moving bed condition. Agglomeration of manganese–iron-oxide particles after several consecutive cycles is reported [25,26] as well as fragmentation and breakage [26]. Thus, the metal–oxide particles are prevented from entering the dosing unit by a sieve (2.5 mm mesh size), which is located between the buffer section and the dosing unit as a precaution. The inert filling material can easily pass the sieve and is transported into a container connected to the screw conveyor. A knocking device is installed at the buffer section to support particle movement (Aldak, VTP-25, operated with 2 bar to 6 bar compressed air). In total, the reduction, oxidation, and buffer sections sum up to a height of 3.1 m.

The flow diagram of the setup is displayed in Figure 3. A mixture of compressed air (01/min to 2001/min) and nitrogen 5.0 (01/min to 751/min) is regulated by two mass flow controllers (Bronkhorst HI-TEC, accuracy $\pm 0.5\%$ reading and $\pm 0.21/\text{min}$). All gas flow rates in this study are based on norm conditions ($T_{g,n} = 0^\circ\text{C}$ and $p_n = 1013.25\text{ hPa}$). The oxygen concentration in the off-gas is analyzed via paramagnetic oxygen measurement (NGA-2000 MLT-2, Emerson Process Management/Rosemount Analytical) and used to calculate the extent of conversion during the reduction and oxidation of the metal-oxide particles. The off-gas is cooled by a water-based cooling unit and filtered (high-efficiency particulate air filter) before entering the gas analyzer. Two pressure transducers ($-1/1\text{ bar}$ relative with an error $\pm 2\text{ mbar}$, B + B sensors) measure the pressure drop across the particle bed inside the reactor. The gas flow can bypass the reactor by adjusting the position of two throttle valves.

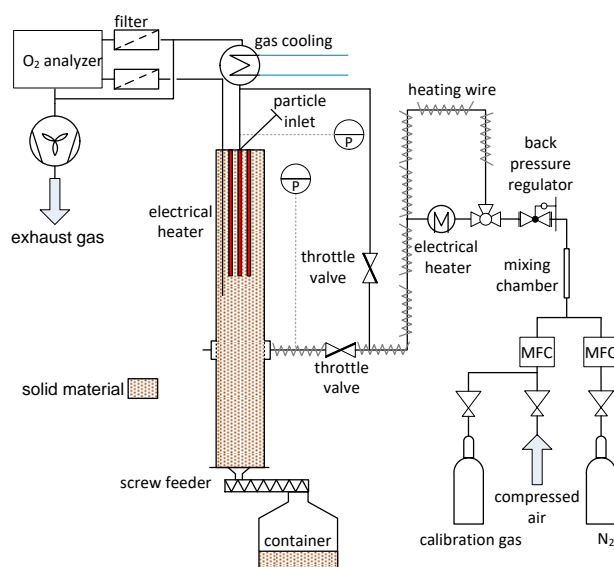


Figure 3. Flow diagram of the reactor setup.

2.3. Experimental Procedure

Prior to each metal-oxide experiment, the reactor was filled with bauxite and metal-oxide particles from the top. The buffer and oxidation section then consisted of bauxite particles, while the metal-oxide particles lay on top of the bauxite bulk in the reduction section. The experiment is composed of two segments: In the beginning, the metal-oxide bulk is reduced in a fixed bed operation (charging), followed by the oxidation under a moving bed condition (discharging). For the charging segment, the temperature of the heating elements was regulated to 1070 °C in order to reduce the metal-oxide particles in the reduction section. During this step, an air stream \dot{V}_n of 35 l/min flowed through the bulk at a gas inlet temperature $T_{g,in}$ of 480 °C to 500 °C. After 14.5 h of dwell time at a heating element temperature of 1070 °C, a bulk temperature of 1055 °C was measured at a central position in the reduction section. To foster the initial particle flowability for the subsequent moving bed operation, the heating element temperatures were reduced to 900 °C. Prior to this decrease of the bulk temperature, the gas flow was switched to a nitrogen flow for a period of 3 h to impede an early oxidation of the manganese–iron-oxide particles. The bulk movement for the moving bed experiment was induced and regulated by the screw conveyor by adjusting the volume flow rate. The dosing unit conveyed the bauxite particles in a connected container, while the metal-oxide bulk stayed in the buffer section, hindered by a filter, to minimize the mechanical stress for the metal-oxide particles. The gas flow was switched from nitrogen back to air before the metal-oxide bulk entered the oxidation section on top of the bauxite bulk. A reference moving bed experiment was performed with a metal-oxide particle flow of 3 g/s in countercurrent to an air flow \dot{V}_n of 150 l/min with a gas inlet temperature $T_{g,in}$ of 300 °C. The selected air flow should result in gas velocities below the minimal fluidization velocity of the manganese–iron-oxide bulk. After 4.5 h, the reduction and oxidation section was emptied of metal-oxide particles.

2.4. Conversion Calculation

The reaction conversion α of the redox reaction is calculated with the start mass of oxidized particles, oxygen concentration in the off-gas stream $c_{O_2,out}$, and the air flow $\dot{V}_{g,in}$ at the gas inlet, all of them being measured input parameters. A stoichiometric mass loss of 2.693% based on the oxidized phase results from the reaction equation (Equation (1)) for $(\text{Mn}_{0.7}\text{Fe}_{0.3})_2\text{O}_3 + 20 \text{ wt.}\% \text{ ZrO}_2$. A nitrogen balance yields the off-gas stream, with the assumption that the air entering the reactor only consists of O_2 and N_2 , N_2 being inert:

$$\dot{V}_{g,out} = \frac{\dot{V}_{g,in}(1 - c_{O_2,in})\rho_{N_2,in}}{(1 - c_{O_2,out})\rho_{N_2,out}}. \quad (2)$$

The oxygen concentration of the air flow $c_{O_2,in}$ at the gas inlet is fitted with the oxygen concentration in the off-gas $c_{O_2,out}$ when the reactor is under ambient condition, and thus, a nonreactive environment can be assumed. The difference of molar oxygen flow in and out of the reactor yields the molar amount of oxygen connected to the redox reaction. As a final step, the conversion α is calculated as a ratio of the accumulated molar uptake or release of oxygen due to the reaction $\dot{n}_{O_2,r}(t)$ to the stoichiometric molar oxygen release or uptake of the metal-oxide start mass $n_{O_2,s}$:

$$\alpha(t) = \frac{\sum_{t=0}^{t_{end}} \dot{n}_{O_2,r}(t) \times \Delta t}{n_{O_2,s}}. \quad (3)$$

3. Results and Discussion

The functional investigation of the installed moving bed reactor was performed with a manganese–iron-oxide particle flow in countercurrent to an air flow. Since the heat transfer of thermal and thermochemical energy can overlap in the moving bed reactor, the temperature and pressure dependence of the reaction rate of the redox reaction of the manganese–iron-oxide

particles is decisive. Therefore, in the first step, the reaction characteristics of the metal-oxide particles were examined regarding the effective onset temperatures as well as the pressure and temperature dependence on the reaction rate. In the next step, the effect of the release of reaction enthalpy on the temperature profile and reactor performance of a moving bed reactor was investigated experimentally. Finally, the suitability of the manganese-iron-oxide particles for application as heat transfer medium and thermochemical energy storage material in a moving bed reactor is discussed.

3.1. Reaction Characteristics

The effective onset temperature of the manganese-iron oxide is one crucial material parameter which influences the temperature profile of the moving bed reactor being studied. Dynamic thermogravimetric analyses yield a temperature threshold of 915.5 °C for the oxidation onset and 1003.1 °C for the reduction onset of the manganese-iron-oxide particles based on an oxygen partial pressure of 200 hPa (see Appendix B). This temperature difference is referred to as “thermal hysteresis” and was also reported for manganese-iron oxides with different cation ratios [14,16]. Apparently, reaction kinetics limit the conversion between 915.5 °C and 1003.1 °C in such an amount that this temperature area is technically irrelevant for a moving bed reactor. Nevertheless, the samples were reduced and oxidized to a conversion extent of at least 99% during all cycles of the applied heating and cooling rates between 1 K/min and 30 K/min. Therefore, two conclusions concerning the envisaged moving bed experiments can be drawn: Firstly, the oxidation of the manganese-iron-oxide particles will occur below the effective onset temperature of 915.5 °C, and finally, reaction kinetics should not limit the conversion for cooling rates up to 30 K/min in case of an oxygen partial pressure of 200 hPa.

As a next step, the temperature dependence on the reaction rate is analyzed with TGA. The obtained conversion during isothermal measurements between 500 °C and 925 °C is presented in Figure 4. The samples were reduced in a gas flow containing 21% oxygen at 1050 °C prior to the analysis of the oxidation reaction for a selected temperature. As a next step, to initiate the oxidation, the material was at first cooled to the specific temperature in nitrogen, and then after 5 min dwell time, it was exposed to a gas flow containing 21% oxygen. The reaction rate reaches its maximum between a temperature of 700 °C to 800 °C for the considered oxygen partial pressure of 210 hPa. Outside of this temperature range, the induction period is prolonged and the reaction rate decreases. Especially a solid temperature above 900 °C or below 550 °C drastically reduces the reaction rate. A minimal induction period of 1 min can be identified for all isothermal measurements in Figure 4b. Furthermore, the isothermal measurement at 925 °C indicates that the oxidation can be triggered above the previously determined onset temperature, although with a low reaction rate. Regarding the application in a moving bed, the operational conditions should allow for a particle residence time of at least 4 min in the temperature range of 700 °C to 800 °C to favor a full conversion of the material.

However, in contrast to the conditions in thermogravimetric analysis, the oxygen partial pressure will be reduced by oxidation in the moving bed experiment due to a higher ratio of particle mass to gas flow. Therefore, the pressure dependence of the reaction is examined using isothermal measurements at 850 °C (see Figure 5).

The measurements indicate a clear correlation between the oxygen partial pressure and the reaction rate. A lower oxygen partial pressure causes a lower reaction rate and prolongs the induction period of the reaction. Higher gas flows could therefore lead to an increased reaction conversion as they counteract the drop in oxygen partial pressure and thus increase the reaction rate.

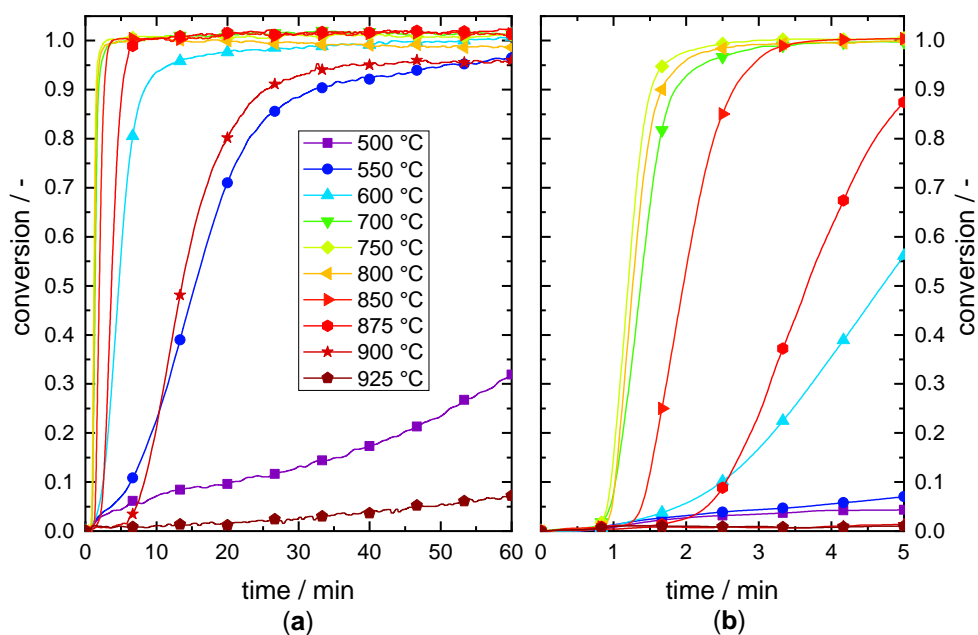


Figure 4. Oxidation conversion of manganese–iron oxide particles during isothermal measurements with an oxygen partial pressure of 210 hPa in a thermogravimetric analyzer. (a) Overview of the reaction conversion of the isothermal section. (b) Enlarged plot of the reaction conversion during the first 5 min of the isothermal section.

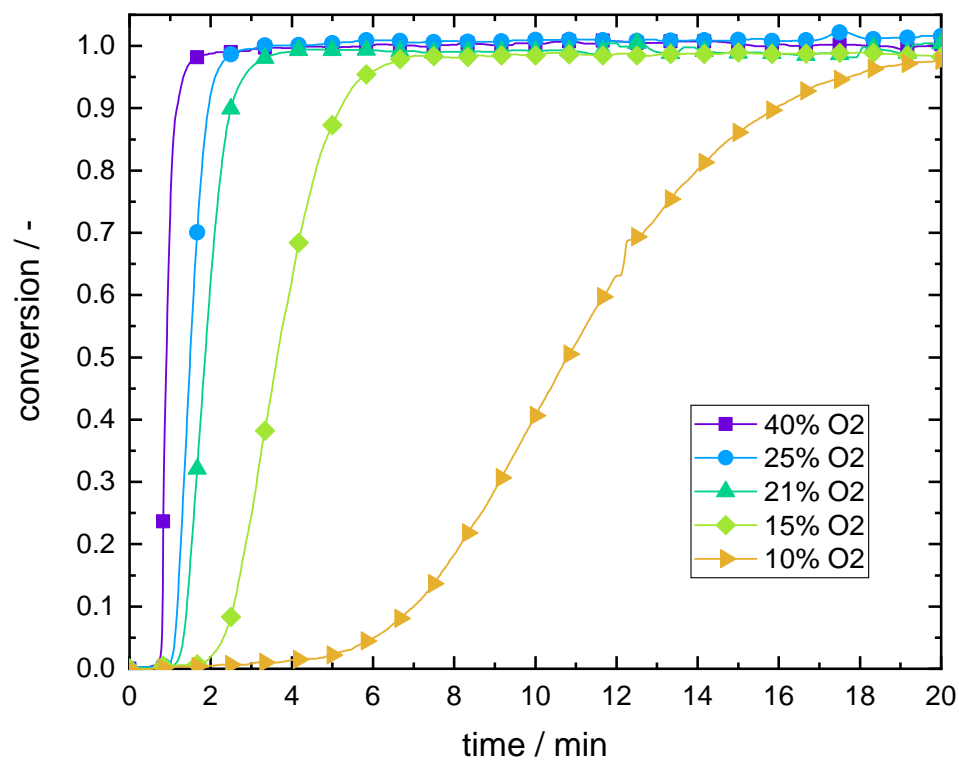


Figure 5. Isothermal oxidation of manganese–iron oxide particles with varying oxygen partial pressure in a thermogravimetric analyzer at 850 °C.

3.2. Experimental Results of a Moving Bed Reactor Operated with Mn–Fe-Oxide Particles

The interaction of the release of reaction enthalpy and the direct heat transfer of sensible thermal energy to a gas stream was investigated with a moving bed reactor based on metal-oxide particles. In Figure 6, the gas and solid temperatures during moving bed condition with a metal-oxide flow of 3 g/s in countercurrent to an air flow \dot{V}_n of 150 l/min are displayed together with the oxygen concentration in the off-gas. The diagram represents a period of the moving bed operation, when preheated manganese–iron-oxide particles continuously enter the oxidation section (compare Figure 2a). The position of the thermocouples in the oxidation section is given in the schematic next to the diagram.

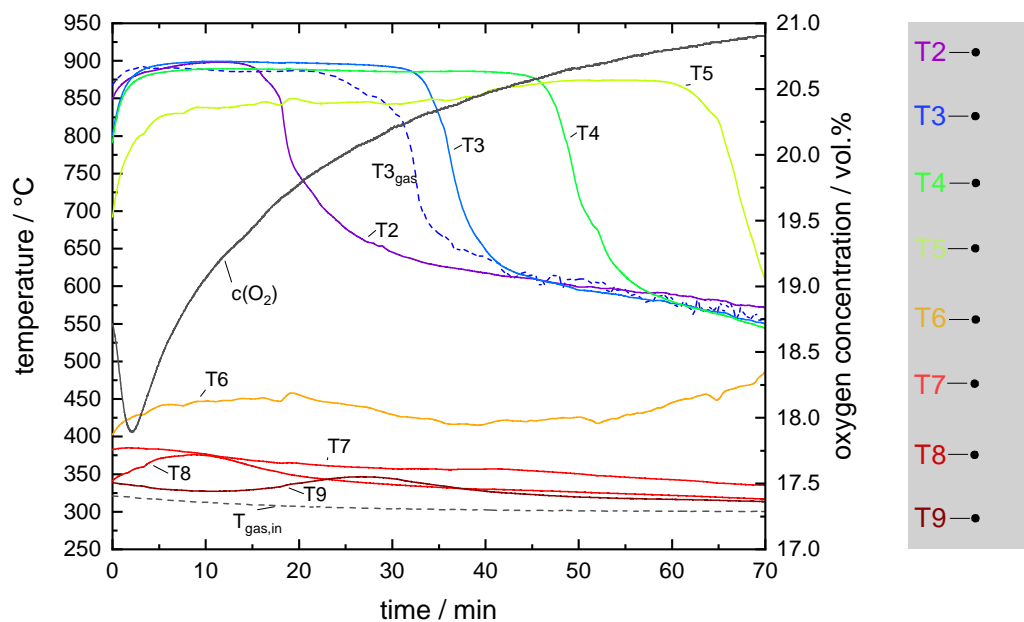


Figure 6. Solid (continuous line) and gas temperatures (dashed line) during moving bed operation with 3 g/s particle flow in countercurrent to an air flow \dot{V}_n of 150 l/min. The oxygen concentration in the exhaust gas is shown on the right axis of ordinate. The schematic of the oxidation section next to the diagram displays the temperature measurement points.

The bulk temperatures show a different course at different bed heights. In the first 20 cm of bed height (T2 to T4), the bulk temperature forms plateaus between 886 °C and 897 °C. The bulk temperature at level T5 increases with time to the temperature range of the temperature plateaus as well. The temperature drop at the end of each plateau marks the point in time when the top layer of the manganese–iron-oxide bulk falls below this measuring point. In contrast to the temperature plateaus between bed height level T2 to T5, the bulk temperature strongly decreases in the following 10 cm to bed height level T6. As a result, the bulk is cooled with a rate of 24 K/min in between those measurement points, considering the temperature change of the topmost layer of the metal-oxide bulk. The gas temperature at level T3 follows the course of the bulk temperature at the same bed height. Due to the heat transfer between the particle bed and the gas flow, the gas temperature increases from $T_{gas,in}$ to $T_{3,gas}$ by a maximum value of 580 K. This temperature increase correlates with the obtained thermal power of the reactor, which will be discussed in Section 3.3. The oxygen concentration strongly declines during the first 10 min, which can be attributed to the oxygen uptake caused by the oxidation reaction. However, the starting oxygen concentration in the off-gas is still on a low level because of the nitrogen atmosphere prior to the displayed period of the moving bed operation. In total, 80.2% of the former reduced particles were oxidized during moving bed operation. The initial heating period under fixed-bed condition resulted in an absolute reduction conversion of 77.1%. It has to be noted that the measured oxygen concentration provides the reaction condition as an average over the whole

bed. Therefore, the effect of oxidation on the oxygen concentration at a lower bed height could exceed the effect of reduction from the bulk close to the heating section of the reactor. This fact could result in a higher absolute conversion than calculated.

In Figure 7, the development of a temperature profile of several particle layers during the moving bed operation of the reactor with a Mn–Fe-oxide mass flow of 3 g/s is displayed. The temperature profile depicts the change in temperature when particle layers, in distance of 2 cm to each other, move through the oxidation section. The temperature of the first particle layer in Figure 7 at a bed height of 70 cm corresponds to the solid particle temperature which is measured after 3 min in Figure 6 at the level of T2. The temperature development of the particle layers is selected according to the theoretical bulk movement of 0.65 cm/min.

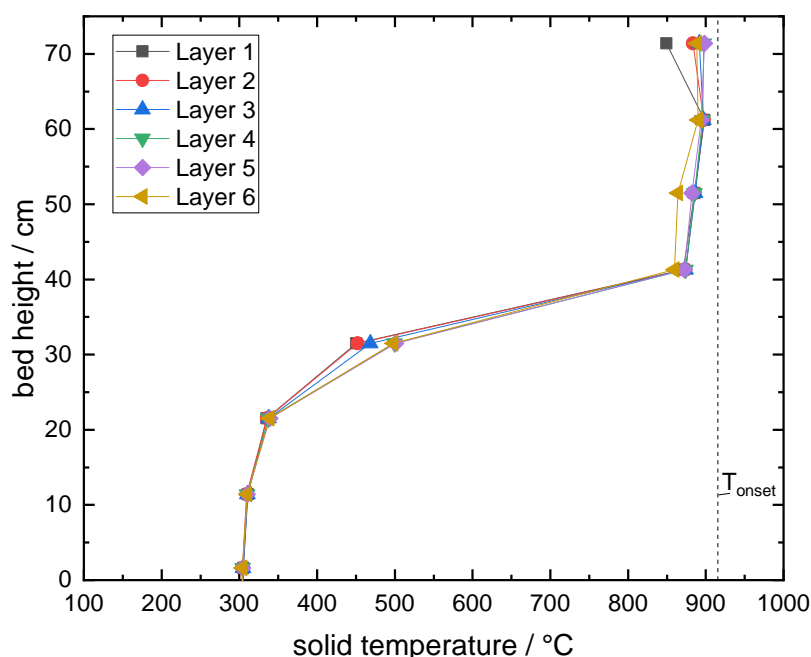


Figure 7. Development of the solid temperature of several layers (in 2 cm distance to each other) along the bed height in the oxidation section. The temperature development is selected according to the theoretical bulk movement. The effective onset temperature of the oxidation of the manganese–iron oxides is added as a dashed line.

The effect of the exothermic reaction is clearly visible by the nearly isothermal bed height of 30 cm. In general, the layers show a stationary temperature profile for the presented time period. Apparently, the amount of the released reaction enthalpy of the oxidation is able to compensate to a great extent for the heat transfer to the gas flow and thermal energy losses to the surrounding, e.g., thermal mass of reactor tube and heat transfer through insulation in the upper part (at bed height 40 cm to 70 cm) of this reactor setup. Overall, the solid temperature drops from 900 °C to 300 °C along the bed height. However, the particles reach the gas inlet temperature within a sharp front of ~20 cm. The lower part of the oxidation section (at bed height 0 cm to 20 cm) is again almost isothermal, however, in this case without chemical reaction. Thus, the reactor length could be shortened by around 20 cm without reducing the attained energy density of the thermochemical storage material or the thermal power of the moving bed reactor. The reproducibility of the formation of this characteristic nearly isothermal bed height is confirmed in Appendix C.

So far, it is unknown if the heat transfer of thermochemical and thermal energy overlap in the height section of high cooling rates. Obviously, oxidation takes part in the isothermal bed height. However, the experimental data does not describe the local oxygen concentration and thus conversion status. The determined reaction characteristics at different temperatures, cooling rates, or oxygen

partial pressures of the previous Section 3.1 can be applied to estimate the possibility of further reaction conversion in the section with a temperature gradient of the bulk. The moving bed experiment resulted in an oxidation conversion of 80.2% and temperature plateaus between 886 °C and 897 °C, which is below the effective onset temperature for oxidation of 915.5 °C. In TGA, the reaction requires 50 min at a sample temperature of 900 °C to attain a conversion extent of 96%, whereas full conversion is achieved after 5 min at 850 °C in case of 20% oxygen in the atmosphere (see Figure 4). The residence time of the particles in the nearly isothermal bed height of the moving bed reactor is around 50 min, considering a particle velocity of 0.65 cm/min. Thus, if the effect of the oxygen partial pressure can be neglected, the particles should be oxidized in the bed height of nearly isothermal conditions before their temperature is decreased to 300 °C. Furthermore, the attained cooling rates in the moving bed experiment depicted in Figure 6 are in the range of the investigated cooling rates of TGA measurements (Figure A2), where the extent of oxidation conversion was determined to exceed 99% for cooling rates of up to 30 K/min. However, as a minimal oxygen concentration of 17.9% was measured during the moving bed experiment, the oxygen partial pressure in the moving bed experiment was lower than the applied oxygen partial pressure in the TGA measurements regarding the temperature dependence of the reaction rate or the determination of onset temperatures for various cooling rates. Isothermal measurements at 850 °C based on TGA indicated that a decrease of oxygen concentration from 21% to 15% doubles the reaction time required to achieve an oxidation conversion of 99% (see Figure 5). In the end, the metal-oxide particles probably continued oxidizing in the section with high temperature gradients below the bed height with nearly isothermal conditions, which would result in overlapping heat transfer of thermochemical and thermal energy. An additional simulation of the presented moving bed experiment could yield the local extent of conversion caused by this complex correlation between chemical reaction and heat transfer.

3.3. Energetic Evaluation of the Moving Bed Reactor

The heat transfer between gas and solid is the main task of the presented moving bed reactor. Even though the gas temperature is difficult to measure at these elevated temperatures, the thermal power of the heat exchanger is estimated with $P_{th} = \int \dot{V}_{g,in} \rho_{g,norm} c_{p_g}(T) dT_g$. Here, $c_{p_g}(T)$ equals the temperature dependent specific heat capacity of the gas flow $\dot{V}_{g,in}$, which is stated for the gas density at norm condition $\rho_{g,norm}$. Figure 8 displays the attained thermal power during the period of moving bed operation corresponding to Figure 6. The gas temperature at level T3 directly determines the course of the thermal power curve, since the gas inlet temperature is nearly constant. The thermal power is nearly constant when particles with a stationary inlet temperature entered the oxidation section and drops, as soon as the top of the bulk passed level T3. From this moment on, the available bulk height for heat exchange decreases with time. Overall, the experiment achieved a peak power of 2.1 kW and an average power of 2.0 kW for 30 min.

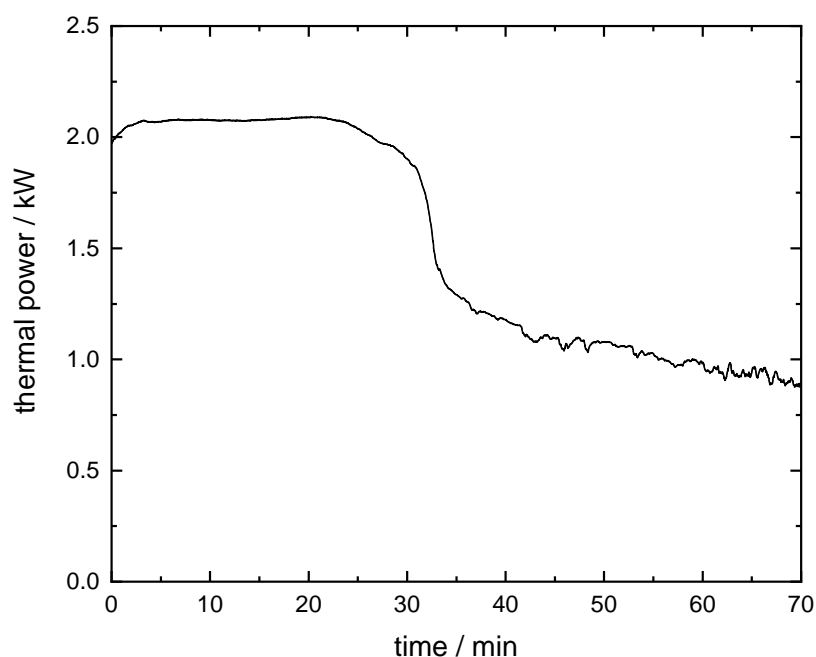


Figure 8. Attained thermal power of the moving bed reactor, which is transferred to the gas flow (150 l/min) by the countercurrent metal-oxide flow of 3 g/s: The displayed period of moving bed operation equals the period shown in Figure 6.

The energy density is a crucial factor to compare energy storage materials. Since the presented reactor facilitates the heat transfer of sensible as well as thermochemical energy to the countercurrent gas flow, the energy density of the manganese–iron-oxide particles is increased by the sensible share in energy density in comparison to other thermochemical energy storage materials. The manganese–iron-oxide particles entered the oxidation section of the reactor with 895 °C at position T3 and exited the oxidation section with 304 °C at T9. The gravimetric energy density of the metal-oxide particles can be calculated based on the specific heat capacity for the oxidized phase and the reaction enthalpy of 188 J/g (see Section 2). As a result, an energy density of 569 kJ/kg (or 158 Wh/kg) is achieved with the investigated metal-oxide particles and reactor setup, based on the oxidized phase of the material $(\text{Mn}_{0.7}\text{Fe}_{0.3})_2\text{O}_3 + 20\text{wt.}\% \text{ ZrO}_2$. Here, the thermochemical share in energy density accounts for 21.1 %.

In conclusion, the concept of combined utilization of the release of reaction enthalpy and heat transfer of sensible thermal energy in a countercurrent moving bed reactor is feasible. The manganese–iron oxide was reoxidized to an extent of 80.2% relative to the extent of previous reduction. To improve the extent of oxidation conversion, three options are conceivable: Firstly, it is beneficial to increase the oxygen partial pressure during the moving bed operation to impede the limitations of the reaction kinetics. However, raising the oxygen partial pressure beyond ambient conditions would negate the advantage of simple gas handling when utilizing metal oxides as thermochemical energy storage. Secondly, lower solid flow rates would cause a higher particle residence time in a temperature range relevant for higher reaction rates, but it would also decrease the thermal power. Finally, an indirect heat transfer in the bed height of the nearly isothermal condition has the potential to lower the solid temperature to a level that allows for higher reaction rates without the need to decrease the total gas flow. For example, the gas flow could be first heated indirectly by the bed height of the nearly isothermal condition before entering the moving bed reactor for the heat transfer of sensible thermal energy. However, this would lead to higher solid outlet temperatures and thus a reduced utilization of the inherent thermal energy. In addition, the indirect heat transfer in the bed height of nearly isothermal conditions could power other high temperature processes, such as a thermoelectric generator or an alkali-metal thermal to electric converter.

3.4. Particle Handling in a Moving Bed Reactor Based on Manganese–Iron Oxide

The flowability of manganese–iron-oxide particles at elevated temperatures posed a major challenge when performing moving bed experiments. Especially the initiation of the metal-oxide movement after the particles were heated in the reduction section of the reactor (see Figure 2a) caused a discontinuous particle flow during most of the experiments, which are not presented in this study. In addition, the subsequent particle movement through the different sections of the reactor was aided by a knocking device and partial manual knocking on the buffer section. The blocking of the particles in the reactor tube after being heated and reduced in fixed bed operation emphasizes the necessity of a continuously working solar receiver. Concerning the presented metal-oxide experiment, the cooling of the manganese–iron-oxide particles in nitrogen atmosphere to around 905 °C particle temperature in combination with several pressure surges resulted in a successful initiation of the moving bed operation.

Agglomeration of the particles could constitute one reason for the low flowability of the metal-oxide bulk. However, our previous work about the particle stability of the same manganese–iron oxide did not indicate a high tendency towards agglomeration [26]. A picture of the uppermost layer of the metal-oxide bulk after the moving bed experiment is displayed in Figure 9b. For this purpose, the reactor was opened between the oxidation section and the buffer section. No agglomerates or channels were discovered after this experiment. Furthermore, Figure 9a depicts an exemplary amount of metal-oxide particles in the untreated condition (1) or after 15 experiments in the moving bed reactor (2). The comparison reveals no visible change in particle constitution.

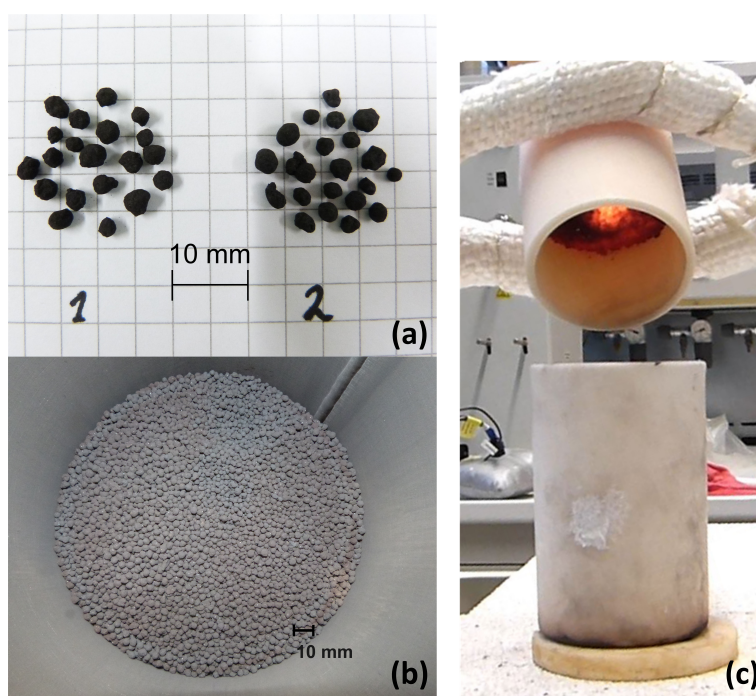


Figure 9. (a) Comparison of fresh manganese–iron oxide particles (1) to manganese–iron oxide particles after 15 redox cycles in the moving bed reactor (2). (b) Picture of the uppermost bulk layer after the described moving bed experiment. (c) Picture of the flowability tests performed after the sample was extracted from the chamber furnace set at 1050 °C.

The flowability of the metal-oxide bulk in the reactor setup was tested at room temperature with a particle flow of 3 g/s. The velocity of the uppermost particle layer was determined and compared with the theoretical velocity, which was obtained by calibrating the screw conveyor. The agreement of the experimental velocity with the theoretical velocity proves the basic flowability of the material at room temperature. Therefore, the temperature dependence of the particle flowability was additionally

investigated. An amount of 100 g manganese–iron oxide particles was filled in a ceramic beaker and cycled between temperatures of 50 °C and 1050 °C in a chamber furnace with ambient atmosphere. The metal-oxide sample was extracted from the furnace at different temperatures and transferred into an empty ceramic beaker to examine the flowability. The picture in Figure 9c illustrates a time section of the particle transfer when the sample was extracted from the furnace at 1050 °C with a measured sample temperature of 1034 °C initially to the decanting process. At this high temperature, the sample was initially stuck in the ceramic beaker. Over several stages, the sample then flowed into the empty beaker within a cooling time of 2 min, requiring slight shaking movements or knocking of the beaker onto a refractory brick. The sample was transferred back to the original ceramic beaker without difficulty at a particle temperature of around 700 °C to 860 °C. Repeating the decanting process between 850 °C and 1050 °C confirmed the reduced flowability, whereas the particles were free flowing at a sample temperature of 550 °C. In summary, the flowability of the manganese–iron oxide particles is limited, when they are previously heated as a fixed bed to temperatures between 850 °C and 1050 °C.

4. Conclusions

The first moving bed reactor for thermochemical energy storage at high temperatures has been put into operation and analyzed in detail. The reactor addressed the combined utilization of thermochemical and sensible energy based on metal-oxide particles, which is important to enhance the system efficiency. The reaction behavior of the material at different temperatures and pressures was investigated to pretest the reaction capability at probable experimental operation conditions. Furthermore, the suitability of the manganese–iron oxide was assessed for application in a continuously operated system. The main conclusions considering technical applications are as follows:

- Thermogravimetric analyses revealed that cooling rates of up to 30 K/min pose no challenge for the oxidation of the investigated manganese–iron oxide at an oxygen partial pressure of 20 kPa. Furthermore, sufficient long-term stability of the redox reaction was demonstrated for 60 consecutive cycles in TGA.
- The oxidation of the manganese–iron oxide caused two distinct temperature sections during the moving bed experiment: one section with nearly isothermal conditions and one section with a temperature gradient similar to a moving bed operation based on inert storage material. A thermal power of 2 kW was transferred to the gas flow during stationary temperature conditions.
- The manganese–iron oxide particles were oxidized to an extent of 80.2% during moving bed operation, based on the preceding partial reduction of 77.1%. An indirect heat transfer in the section of nearly isothermal condition could increase the oxidation conversion because the particle temperature could be regulated to a level of higher reaction rates.
- The flowability of the manganese–iron-oxide particles was limited at high temperatures in the moving bed reactor. Additional tests revealed an insufficient flowability between 850 °C and 1050 °C. However, the underlying mechanism needs to be further addressed for an application of this manganese–iron oxide compound in a continuously operated system.

Author Contributions: Conceptualization, N.C.P. and M.L.; methodology, N.C.P. and M.L.; software, N.C.P.; validation, N.C.P. and M.L.; formal analysis, N.C.P.; investigation, N.C.P.; resources, N.C.P.; data curation, N.C.P.; writing—original draft preparation, N.C.P.; writing—review and editing, M.L.; visualization, N.C.P.; supervision, M.L.; project administration, M.L.; funding acquisition, M.L. All authors have read and agreed to the published version of the manuscript.

Funding: This research received no external funding.

Acknowledgments: The authors wish to thank Andreas Kohzer, Niklas Giesen (both Institute of Thermodynamic Engineering, German Aerospace Center, Cologne, Germany), and Sofie Ek (Department of Chemistry and Chemical Engineering, Chalmers University of Technology, Gothenburg, Sweden) for their support while assembling the reactor and running experiments. Furthermore, the authors thank Andrea Hanke (Institute of Thermodynamic Engineering, German Aerospace Center, Stuttgart, Germany) for performing the DSC to

examine the specific heat capacity of the metal-oxide particles and Henrik Winnemöller (Johannes Gutenberg University Mainz, Mainz) for proofreading.

Conflicts of Interest: The authors declare no conflict of interest.

Appendix A. Cycle Stability of the Redox Reaction of Mn–Fe Oxide

Two consecutive cycling tests, consisting each of 30 redox cycles, were carried out in TGA with a heating and cooling rate of 20 K/min at an oxygen partial pressure of 20 kPa. The first 30 cycles were performed between a sample temperature of 850 °C and 1050 °C, whereas the lower sample temperature was decreased to 750 °C for the following 30 cycles. Figure A1 depicts the mass loss of exemplary cycles. Both the reduction and oxidation indicate a stable mass loss over 60 redox cycles.

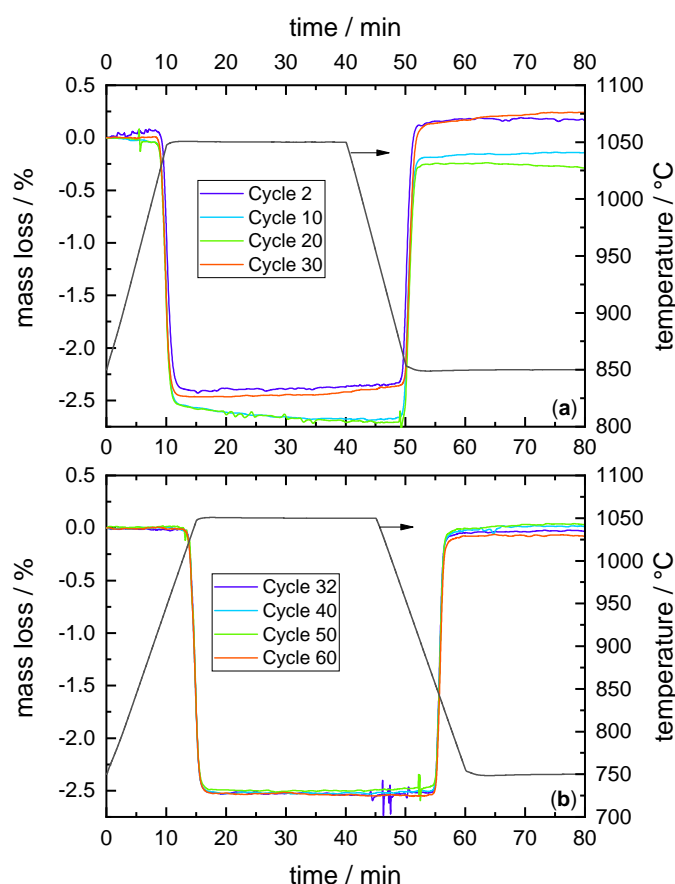


Figure A1. Relative mass loss of the manganese–iron oxide compound during several redox cycles performed in TGA with an oxygen partial pressure of 20 kPa and a heating and cooling rate of 20 K/min. (a) The sample temperature was varied between 850 °C and 1050 °C during the first 30 redox cycles. (b) The next 30 redox cycles were carried out between a sample temperature of 750 °C and 1050 °C.

Appendix B. Determination of the Effective Onset Temperature of the Investigated Mn–Fe Oxide

The effective onset temperature of the oxidation and reduction of the transition of $(\text{Mn}_{0.7}\text{Fe}_{0.3})_3\text{O}_4/(\text{Mn}_{0.7}\text{Fe}_{0.3})_2\text{O}_3$ is determined via thermogravimetric analysis. Dynamic measurements with 1–5–10–20 and 30 K/min heating or cooling rate and an atmosphere of 20% oxygen were performed. The extrapolation to 0 K/min of the average onset temperatures of 3 cycles with different heating or cooling rates yields the effective onset temperature and is displayed with dashed lines in Figure A2 for oxidation and reduction.

Obviously, the effective onset temperature of the reduction deviates from the effective onset temperature of the oxidation. A temperature difference of 87.6 °C between the two onset temperatures

is found for the applied oxygen partial pressure and is referred to as thermal hysteresis of the redox reaction. The gained temperature borders do not equal the thermodynamic equilibrium, which was calculated with Factsage (phase transition: bixbyite + spinel to bixbyite). However, the effective onset temperatures constitute a technical temperature threshold for the application of the Mn–Fe oxide under ambient atmospheric conditions.

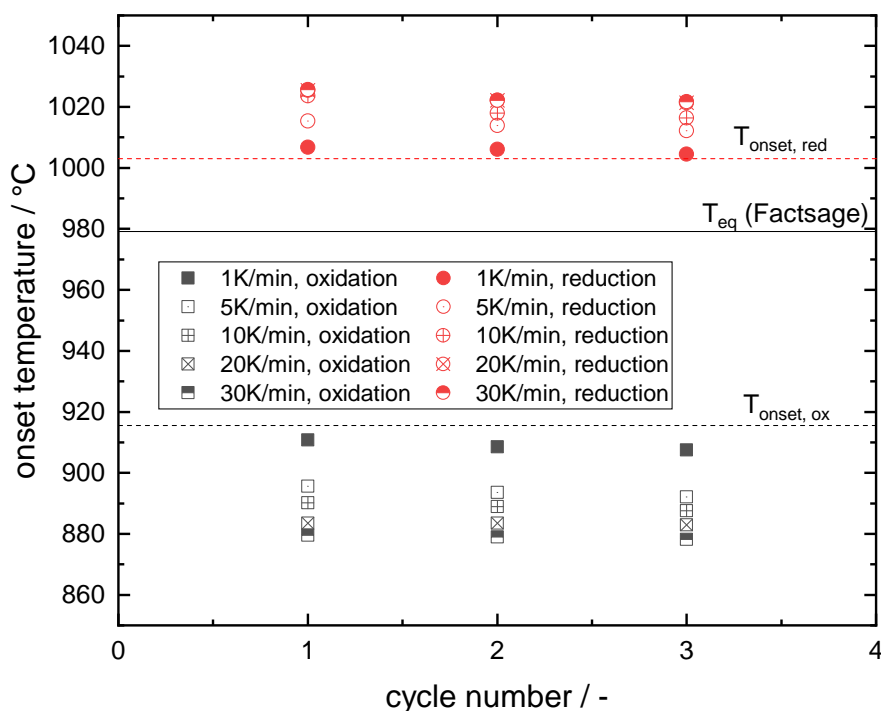


Figure A2. Obtained onset temperatures of reduction and oxidation of the investigated manganese–iron oxide for 3 consecutive cycles in a thermogravimetric analyzer, applying an oxygen concentration of 20% at different heating and cooling rates: The effective onset temperatures (dashed lines) and the thermodynamic equilibrium (solid line) are displayed as well.

Appendix C. Reproducibility of the Characteristic Isothermal Bed Segment

The development of the solid temperature of several particle layers during nearly steady-state operation of the moving bed experiment presented in this study is compared to an additional moving bed experiment in Figure A3. The additional experiment was performed with the same particle flow rate but a lower gas flow rate and gas inlet temperature. The characteristic isothermal bed segment (bed height of 40 cm to 70 cm), which is caused by the oxidation, is identical for both experiments in position and temperature. The following segment (bed height 10 cm to 40 cm), where the temperature profile is dominated by the sensible cooling of the particle layers, indicates a lower temperature gradient for the additional experiment. This variation between the temperature profiles could be caused by the lower gas flow and an insufficient particle flowability in the additional experiment. Due to the inconsistent particle movement, the results of the additional experiment are not discussed in more detail. Nevertheless, they corroborate the reproducibility of the characteristic temperature profile of a countercurrent moving bed based on a thermochemical material in principle.

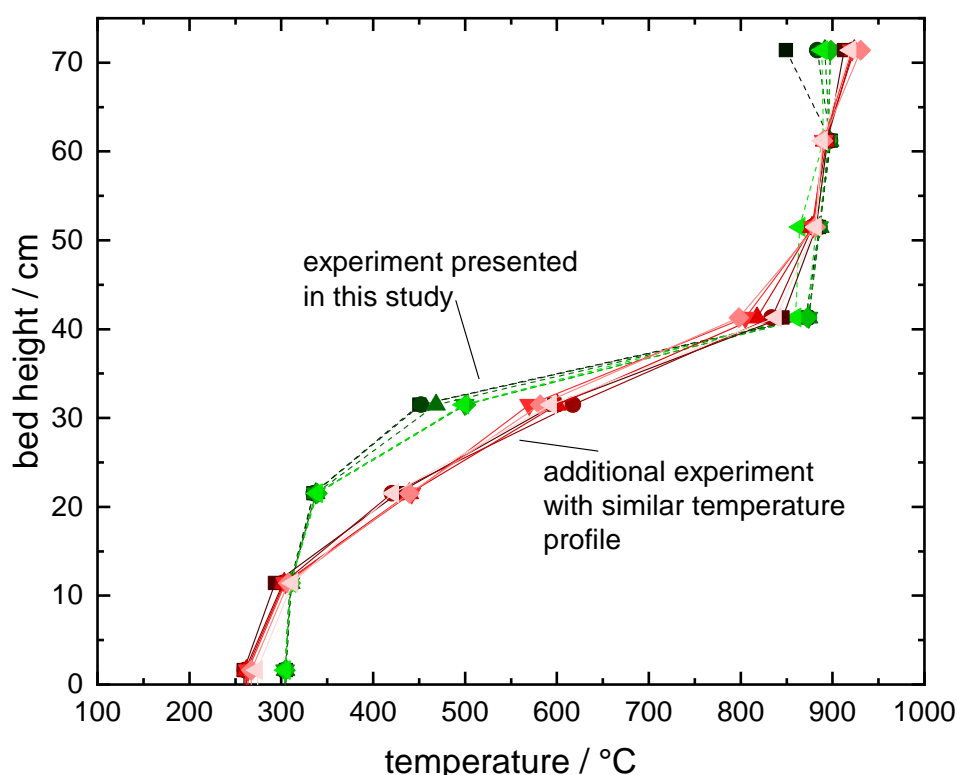


Figure A3. Development of the temperature of 6 particle layers (in 2 cm distance to each other) along the bed height during moving bed operation of the experiment in the study (green dotted lines, compare to Figure 7) and a similar experiment (red solid lines).

References

1. Pardo, P.; Deydier, A.; Anxionnaz-Minvielle, Z.; Rougé, S.; Cabassud, M.; Cognet, P. A review on high temperature thermochemical heat energy storage. *Renew. Sustain. Energy Rev.* **2014**, *32*, 591–610, doi:10.1016/j.rser.2013.12.014. [[CrossRef](#)]
2. Wu, S.; Zhou, C.; Doroodchi, E.; Nellore, R.; Moghtaderi, B. A review on high-temperature thermochemical energy storage based on metal oxides redox cycle. *Energy Conv. Manag.* **2018**, *168*, 421–453, doi:10.1016/j.enconman.2018.05.017. [[CrossRef](#)]
3. Block, T.; Schmücker, M. Metal oxides for thermochemical energy storage: A comparison of several metal oxide systems. *Solar Energy* **2016**, *126*, 195–207, doi:10.1016/j.solener.2015.12.032. [[CrossRef](#)]
4. André, L.; Abanades, S.; Flamant, G. Screening of thermochemical systems based on solid-gas reversible reactions for high temperature solar thermal energy storage. *Renew. Sustain. Energy Rev.* **2016**, *64*, 703–715, doi:10.1016/j.rser.2016.06.043. [[CrossRef](#)]
5. Schrader, A.J.; Muroyama, A.P.; Loutzenhiser, P.G. Solar electricity via an Air Brayton cycle with an integrated two-step thermochemical cycle for heat storage based on $\text{Co}_3\text{O}_4/\text{CoO}$ redox reactions: Thermodynamic analysis. *Sol. Energy* **2015**, *118*, 485–495, doi:10.1016/j.solener.2015.05.045. [[CrossRef](#)]
6. Falcone, P.K.; Noring, J.E.; Hacket, C.E. Evaluation and application of solid thermal energy carriers in a high temperature solar central receiver system. In Proceedings of the IECEC 17th Intersociety Energy Conversion Engineering Conference, Los Angeles, CA, USA, 8–12 August 1982. [[CrossRef](#)]
7. Siegel, N.; Kolb, G. Design and on-sun testing of a solid particle receiver prototype. In Proceedings of the ASME 2008 2nd International Conference on Energy Sustainability, ASMEDC, Jacksonville, FL, USA, 10–14 August 2008; Volume 2, doi:10.1115/es2008-54090.
8. Flamant, G.; Gauthier, D.; Benoit, H.; Sans, J.L.; Garcia, R.; Boissière, B.; Ansart, R.; Hemati, M. Dense suspension of solid particles as a new heat transfer fluid for concentrated solar thermal plants: On-sun proof of concept. *Chem. Eng. Sci.* **2013**, *102*, 567–576, doi:10.1016/j.ces.2013.08.051. [[CrossRef](#)]

9. Agrafiotis, C.; de Oliveira, L.; Roeb, M.; Sattler, C. A solar receiver-storage modular cascade based on porous ceramic structures for hybrid sensible/thermochemical solar energy storage. In *SolarPACES, AIP Conference Proceedings*; AIP Publishing LLC: Melville, NY, USA, 2016; Volume 1734, doi:10.1063/1.4949099. ISBN 978-0-7354-1386-3. [\[CrossRef\]](#)
10. Jafarian, M.; Arjomandi, M.; Nathan, G.J. Thermodynamic potential of molten copper oxide for high temperature solar energy storage and oxygen production. *Appl. Energy* **2017**, *201*, 69–83, doi:10.1016/j.apenergy.2017.05.049. [\[CrossRef\]](#)
11. Agrafiotis, C.; Roeb, M.; Schmücker, M.; Sattler, C. Exploitation of thermochemical cycles based on solid oxide redox systems for thermochemical storage of solar heat. Part 1: Testing of cobalt oxide-based powders. *Sol. Energy* **2014**, *102*, 189–211, doi:10.1016/j.solener.2013.12.032. [\[CrossRef\]](#)
12. Imponenti, L.; Albrecht, K.J.; Kharait, R.; Sanders, M.D.; Jackson, G.S. Redox cycles with doped calcium manganites for thermochemical energy storage to 1000 °C. *Appl. Energy* **2018**, *230*, 1–18, doi:10.1016/j.apenergy.2018.08.044. [\[CrossRef\]](#)
13. Carrillo, A.J.; Serrano, D.P.; Pizarro, P.; Coronado, J.M. Improving the thermochemical energy storage performance of the Mn_2O_3/Mn_3O_4 redox couple by the incorporation of iron. *ChemSusChem* **2015**, *8*, 1947–1954, doi:10.1002/cssc.201500148. [\[CrossRef\]](#)
14. Carrillo, A.J.; Serrano, D.P.; Pizarro, P.; Coronado, J.M. Understanding redox kinetics of iron-doped manganese oxides for high temperature thermochemical energy storage. *J. Phys. Chem. C* **2016**, *120*, 27800–27812, doi:10.1021/acs.jpcc.6b08708. [\[CrossRef\]](#)
15. André, L.; Abanades, S.; Cassayre, L. High-temperature thermochemical energy storage based on redox reactions using Co-Fe and Mn-Fe mixed metal oxides. *J. Solid State Chem.* **2017**, *253*, 6–14, doi:10.1016/j.jssc.2017.05.015. [\[CrossRef\]](#)
16. Wokon, M.; Block, T.; Nicolai, S.; Linder, M.; Schmücker, M. Thermodynamic and kinetic investigation of a technical grade manganese-iron binary oxide for thermochemical energy storage. *Solar Energy* **2017**, *153*, 471–485, doi:10.1016/j.solener.2017.05.045. [\[CrossRef\]](#)
17. Carrillo, A.J.; Moya, J.; Bayón, A.; Jana, P.; de la Peña O'Shea, V.A.; Romero, M.; Gonzalez-Aguilar, J.; Serrano, D.P.; Pizarro, P.; Coronado, J.M. Thermochemical energy storage at high temperature via redox cycles of Mn and Co oxides: Pure oxides versus mixed ones. *Solar Energy Mat. Solar Cells* **2014**, *123*, 47–57, doi:10.1016/j.solmat.2013.12.018. [\[CrossRef\]](#)
18. Block, T.; Knoblauch, N.; Schmücker, M. The cobalt-oxide/iron-oxide binary system for use as high temperature thermochemical energy storage material. *Thermochim. Acta* **2014**, *577*, 25–32, doi:10.1016/j.tca.2013.11.025. [\[CrossRef\]](#)
19. Wong, B. *Thermochemical Heat Storage for Concentrated Solar Power*; Technical Report; Phase II Final Report for the period September 30, 2008 through April 30, 2011; U.S. Department of Energy: Washington, DC, USA, 2011. [\[CrossRef\]](#)
20. Muan, A.; Somiya, S. The system iron oxide-manganese oxide in air. *Am. J. Sci.* **1962**, *260*, 230–240.
21. Wickham, D.G. The chemical composition of spinels in the system $Fe_3O_4-Mn_3O_4$. *J. Inorg. Nucl. Chem.* **1969**, *31*, 313–320. [\[CrossRef\]](#)
22. Crum, J.V.; Riley, B.J.; Vienna, J.D. Binary phase diagram of the manganese oxide-iron oxide system. *J. Am. Ceram. Soc.* **2009**, *92*, 2378–2384, doi:10.1111/j.1551-2916.2009.03230.x. [\[CrossRef\]](#)
23. Kjellqvist, L.; Selleby, M. Thermodynamic Assessment of the Fe-Mn-O system. *J. Ph. Equilib. Diffus.* **2010**, *31*, 113–134, doi:10.1007/s11669-009-9643-6. [\[CrossRef\]](#)
24. Kang, Y.B.; Jung, I.H. Thermodynamic modeling of oxide phases in the Fe-Mn-O system. *J. Phys. Chem. Solids* **2016**, *98*, 237–246, doi:10.1016/j.jpcs.2016.07.017. [\[CrossRef\]](#)
25. Wokon, M.; Kohzer, A.; Linder, M. Investigations on thermochemical energy storage based on technical grade manganese-iron oxide in a lab-scale packed bed reactor. *Sol. Energy* **2017**, *153*, 200–214, doi:10.1016/j.solener.2017.05.034. [\[CrossRef\]](#)
26. Preisner, N.C.; Block, T.; Linder, M.; Leion, H. Stabilizing particles of manganese-iron oxide with additives for thermochemical energy storage. *Energy Technol.* **2018**, *6*, 2154–2165, doi:10.1002/ente.201800211. [\[CrossRef\]](#)
27. Alonso, E.; Pérez-Rábago, C.; Licurgo, J.; Fuentealba, E.; Estrada, C.A. First experimental studies of solar redox reactions of copper oxides for thermochemical energy storage. *Sol. Energy* **2015**, *115*, 297–305, doi:10.1016/j.solener.2015.03.005. [\[CrossRef\]](#)

28. Neises, M.; Tescari, S.; de Oliveira, L.; Roeb, M.; Sattler, C.; Wong, B. Solar-heated rotary kiln for thermochemical energy storage. *Sol. Energy* **2012**, *86*, 3040–3048, doi:10.1016/j.solener.2012.07.012. [[CrossRef](#)]
29. Tescari, S.; Sundarraj, P.; Moumin, G.; Duarte, J.P.R.; Agrafiotis, C.; de Oliveira, L.; Willsch, C.; Roeb, M.; Sattler, C. Solar rotary kiln for continuous treatment of particle material: Chemical experiments from micro to milli meter particle size. In Proceedings of the SOLARPACES 2019: International Conference on Concentrating Solar Power and Chemical Energy Systems, Daegu, Korea, 1–4 October 2019. [[CrossRef](#)]
30. Jackson, G.S.; Imponenti, L.; Albrecht, K.J.; Miller, D.C.; Braun, R.J. Inert and reactive oxide particles for high-temperature thermal energy capture and storage for concentrating solar power. *J. Sol. Energy Eng.* **2019**, *141*, doi:10.1115/1.4042128. [[CrossRef](#)]
31. Alonso, E.; Gómez, F.; Gonzalez-Aguilar, J.; Romero, M. Experimental analysis of Mn_3O_4/MnO reduction in a packed-bed type solar reactor: Oxygen partial pressure influence. In Proceedings of the 2011 SolarPACES Conference, Granada, Spain, 20–23 September 2011.
32. Oles, A.S.; Jackson, G.S. Modeling of a concentrated-solar, falling-particle receiver for ceria reduction. *Solar Energy* **2015**, *122*, 126–147, doi:10.1016/j.solener.2015.08.009. [[CrossRef](#)]
33. Schrader, A.J.; Dominici, G.D.; Schieber, G.L.; Loutzenhiser, P.G. Solar electricity via an Air Brayton cycle with an integrated two-step thermochemical cycle for heat storage based on Co_3O_4/CoO redox reactions III: Solar thermochemical reactor design and modeling. *Sol. Energy* **2017**, *150*, 584–595, doi:10.1016/j.solener.2017.05.003.
34. Nie, F.; Cui, Z.; Bai, F.; Wang, Z. Properties of solid particles as heat transfer fluid in a gravity driven moving bed solar receiver. *Sol. Energy Mater. Solar Cells* **2019**, *200*, 110007, doi:10.1016/j.solmat.2019.110007. [[CrossRef](#)]
35. Álvarez de Miguel, S. Analysis of redox reactions in a fluidized/fixed bed reactor for thermochemical energy storage in solar thermal power plants. Ph.D. Thesis, Universidad Politécnica de Madrid, Madrid, Spain, 2017. [[CrossRef](#)]
36. Cui, Z.; Shao, W.; Chen, Z.; Cheng, L. Mathematical model and numerical solutions for the coupled gas–solid heat transfer process in moving packed beds. *Appl. Energy* **2017**, *206*, 1297–1308, doi:10.1016/j.apenergy.2017.10.011. [[CrossRef](#)]
37. Negri, E.D.; Alfano, O.M.; Chiovetta, M.G. Moving-bed reactor model for the direct reduction of hematite. parametric study. *Ind. Eng. Chem. Res* **1995**, *34*, 4266–4276, doi:10.1021/ie00039a017.
38. Takenaka, Y.; Kimura, Y.; Narita, K.; Kaneko, D. Mathematical model of direct reduction shaft furnace and its application to actual operations of a model plant. *Comput. Chem. Eng.* **1986**, *10*, 67–75, doi:10.1016/0098-1354(86)85047-5. [[CrossRef](#)]
39. Tong, A.; Sridhar, D.; Sun, Z.; Kim, H.R.; Zeng, L.; Wang, F.; Wang, D.; Kathe, M.V.; Luo, S.; Sun, Y.; et al. Continuous high purity hydrogen generation from a syngas chemical looping 25 kW_{th} sub-pilot unit with 100% carbon capture. *Fuel* **2013**, *103*, 495–505, doi:10.1016/j.fuel.2012.06.088. [[CrossRef](#)]
40. Zeng, L.; Tong, A.; Kathe, M.; Bayham, S.; Fan, L.S. Iron oxide looping for natural gas conversion in a countercurrent moving bed reactor. *Appl. Energy* **2015**, *157*, 338–347, doi:10.1016/j.apenergy.2015.06.029. [[CrossRef](#)]
41. Chen, C.; Lee, H.H.; Chen, W.; Chang, Y.C.; Wang, E.; Shen, C.H.; Huang, K.E. Study of an iron-based oxygen carrier on the moving bed chemical looping system. *Energy Fuels* **2018**, *32*, 3660–3667, doi:10.1021/acs.energyfuels.7b03721. [[CrossRef](#)]



3 Discussion and conclusion

In this chapter, all findings are summarized and discussed with regard to an application of manganese-iron-oxide particles in a continuously operated reactor for the extraction of both sensible thermal energy and thermochemical energy. The effect of the oxidation on the temperature profile and resulting energy and power density is assessed as well as the applicability of the manganese-iron-oxide particles for the suggested CSP system. In the end, proposals for further work are presented.

3.1 The impact of the modification of manganese-iron-oxide particles on their stability and handling

The application of metal oxide particles as thermochemical energy storage material and heat transfer medium in a continuously operated CSP plant necessitates sufficient flowability of the particles and resistance of the particles against mechanical stress, especially for long-term utilization. Therefore, the mechanical strength and agglomeration tendency of manganese-iron oxides modified with 20 wt.% ZrO_2 , CeO_2 or TiO_2 was investigated and compared to a pure manganese-iron oxide.

For this purpose, an attrition jet cup simulated strong *mechanical stress* for the particles. The unsupported manganese-iron oxide showed a linear attrition trend in the jet cup after the particles were pretreated with 30 redox cycles in a fixed-bed reactor. Thus, a high particle loss in the continuously operated system can be expected when the unsupported manganese-iron oxide is applied for several cycles. In contrast, the addition of CeO_2 or especially ZrO_2 improved the attrition resistance, in particular after several redox cycles, compared to the unsupported manganese-iron oxide particles.

Furthermore, the particle stability during 30 redox cycles, causing mainly *chemical stress* for the particles, was investigated in a fixed bed reactor by comparing the particle size distribution of fresh and treated samples. The thermal cycling of the redox reaction with unmodified manganese-iron oxide induced agglomeration of the particles, an increase in bed volume, and the formation of fines. The addition of ZrO_2 or CeO_2 impeded the agglomeration of the particles as well as the formation of fines and bed volume expansion. The reduced agglomeration tendency can be correlated to a decrease in grain growth on the particle surface after 30 redox cycles, in particular for the addition of ZrO_2 .

In addition, in temperature shock experiments, the pure and modified manganese-iron oxide particles were exposed to high heating and cooling rates in an either air or nitrogen atmosphere, to focus on the effect of *thermal stress* on the different compounds. The temperature shock experiments with an atmosphere containing only nitrogen did not result

in the formation of agglomerates of any material sample. Therefore, the agglomeration of the unmodified manganese-iron oxide particles, which was detected after cooling the sample, is connected to the redox reaction of the sample and not caused by some sintering process of the reduced phase at these elevated temperatures.

Since the redox reaction of the manganese-iron oxides is the main reason for their application, a modification is inevitable to prevent flowability issues due to the formation of agglomerates. The addition of CeO_2 and particularly ZrO_2 proved promising regarding the enhancement of the mechanical strength and agglomeration tendency of the manganese-iron oxide based samples. Despite X-ray diffraction measurements of the treated samples indicated that CeO_2 and ZrO_2 are mostly inert in the manganese-iron oxide particles, their addition led to a decreased reaction rate and slightly increased deviation of the onset temperatures of reduction and oxidation in the fixed-bed experiment. However, a stable conversion was detected with an extent of at least 90 % for the pure and the ZrO_2 or CeO_2 modified samples in a TGA with similar operational conditions to the thermally induced redox cycles in the fixed-bed reactor. In contrast, the addition of TiO_2 caused the formation of pseudobrookite, hence this sample showed only negligible redox reactivity.

Although the modification of the manganese-iron oxides by means of adding supportive material reduces the reaction rate and the energy density, it is still indispensable for the continuously operated system due to the enhanced particle stability. In the end, the modification of manganese-iron oxide with 20 wt. % ZrO_2 was successful and promising, with regard to the enhanced mechanical strength and agglomeration inhibition. Since additionally, a long-term stability of the redox reaction was demonstrated for 60 consecutive cycles in a TGA, this material was chosen for the moving bed experiment in 20 kg scale.

The application of modified manganese-iron-oxide particles in the moving bed reactor confirmed the low agglomeration tendency, as long as the bulk is investigated at room temperature after the redox cycle, comparable to the previous investigations. Some of the moving bed experiments revealed minor agglomerates on top of the bulk, which easily disintegrated in the hand. Nevertheless, the flowability of the metal oxide bulk was limited at high particle temperatures, especially the initiation of movement after the bulk was heated and reduced under a fixed-bed condition. Thus, the extraction of particles from the high temperature storage tank between the solar receiver and the oxidation reactor, which allows the decoupling of the system's capacity and thermal power, could prove as problematic.

A moving bed experiment at room temperature yielded a continuous movement of the metal oxide bulk with sufficient flowability. Therefore, the effect of the high temperature level and the redox reaction on the flowability was examined by means of decanting experiments at temperatures up to 1050 °C. The flowability decreased in the temperature

range of 550 °C to 850 °C and was significantly diminished at 1034 °C sample temperature, at which the sample was extracted from the oven in form of a fixed bed in a ceramic beaker. Once the particle movement was initiated, the samples could be easily transferred, although still being at an elevated temperature. This fact also emphasizes the necessity of a continuously operated solar receiver. The reduced flowability could be attributed to the redox reaction or a sintering process, which is not detectable anymore when the bulk is cooled to room temperature.

Nevertheless, the modification of manganese-iron oxide with ZrO_2 did lower the agglomeration tendency and thus the particle flowability. Future work should address the flowability of metal oxide particles at high temperatures. A suitable test rig to characterize the granular flowability for high temperature applications is proposed by A. Schrader [58], due to observed agglomeration of perovskite particles in a solar receiver. The addition of ZrO_2 could also have a beneficial effect on the agglomeration tendency of perovskite particles. However, the influence of the amount of supportive ZrO_2 on particle stability and the prevention of agglomeration needs to be considered to possibly increase the energy density of the particles.

3.2 The effect of the oxidation on a moving bed operation

The effect of the metal oxide oxidation and associated release of reaction enthalpy on the temperature profile and thermal power of a counter-current moving bed reactor as well as on the attainable energy density of the metal oxides was investigated experimentally and numerically for the first time. Both the numeric analysis and the experiment revealed the formation of a nearly isothermal segment within the bed, when the moving bed operation approximated steady state. The characteristic temperature profile of a moving bed experiment is depicted in Fig. 3.1. Following to the nearly isothermal segment (orange area in Fig. 3.1), the bulk exhibited a segment with a distinctive temperature gradient (gray area in Fig. 3.1), which is thus dominated by a sensible cooling of the particle flow.

The temperature of the nearly isothermal segment of the moving bed experiment (paper III) complies with the temperature plateau, which was detected during the thermal cycling in fixed-bed operation (paper I), both applying manganese-iron oxide supported with 20 wt.% ZrO_2 . This nearly isothermal bed segment obviously demonstrates the effect of the exothermic oxidation reaction.

The moving bed experiment resulted in a relative oxidation conversion of 80.2 % of the manganese-iron-oxide bulk. However, the experiment is not able to provide information about the local oxygen concentration in the gas phase with the associated conversion status of the solid. A transient 1D FEM simulation of a counter-current moving bed reactor (paper II) was performed to numerically approach the effect of the oxidation. The simulation

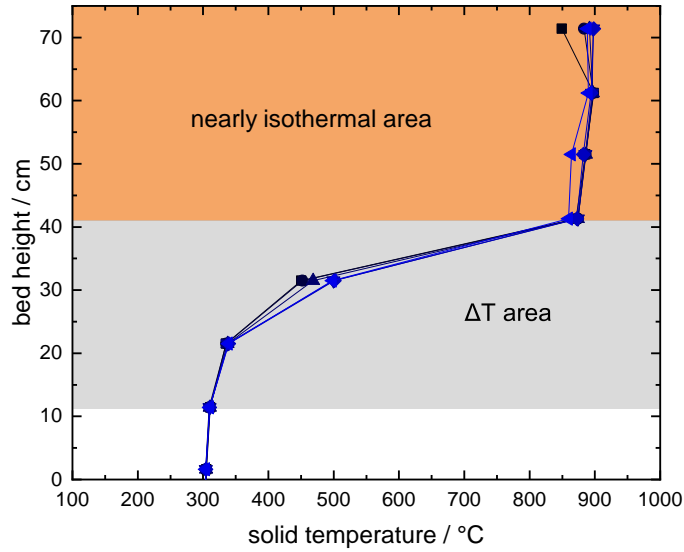


Figure 3.1 Characteristic temperature profile of a moving bed experiment with experimental data from paper III. The temperature development of several particle layers during their travel through the oxidation section of the setup is depicted. Each point corresponds to a temperature measurement in the bulk (Compared to Fig. 7 in paper III).

is based on an unsupported manganese-iron oxide with a slightly increased manganese-content compared to the metal oxides utilized for the experiment. Nevertheless, the fundamental findings on the effect of the oxidation on the temperature profile, the local extent of conversion, the energy density and the thermal power of the reactor can be transferred to the experiment. The simulation identified the highest oxidation conversion in the segment of high temperature gradients close to the gas inlet, since the solid temperature in the nearly isothermal bed segment is in a range, in which the oxidation precedes very slowly. Furthermore, the simulation indicated that in the bed segment with nearly isothermal conditions only a small amount of heat could be transferred from solid to gas, since the gas had already approached the solid temperature. The prevailing cooling rate following the nearly isothermal bed segment impeded full oxidation conversion resulting in an extent which is in range of the experimentally attained extent of conversion for comparable particle and gas flow rates. Thus, in the moving bed experiment, the metal oxides probably continued oxidizing in the bed segment with high temperature gradients, which resulted in an overlapping of reaction enthalpy release and heat transfer of thermal energy between the particle flow and gas flow.

A comparison of a simulated counter-current moving bed operated with inert or reactive manganese-iron oxide highlighted the beneficial effect of the oxidation on the gas outlet

temperature and thus thermal power as well as on the energy density of the particles. However, the extent of conversion and the resulting temperature profile drastically changed in the simulation, when the heat capacity rate ratio of solid to fluid fell below a material characteristic 'tipping point'. In this case, the temperature profile of the solid resembled more that of an inert moving bed with an even higher temperature gradient, which caused a significant drop of the attainable oxidation conversion. The highest extent of conversion was observed for a gas flow rate just below the 'tipping point' for a given particle flow rate. Thus, this 'tipping point' is a crucial material-specific parameter when considering the achievable extent of conversion.

Higher particle flow rates and gas flow rates, selected for the maximal attainable conversion of the corresponding particle flow rate, yielded similar temperature profiles with respect to the temperature and dimension of the nearly isothermal segment. Thus, the characteristic temperature profile of a moving bed reactor operated with manganese-iron oxide stays stable when higher flow rates are applied with a heat capacity rate ratio of the 'tipping point' for an increase of thermal power. Furthermore, the flow rate variation indicated that the moving bed reactor facilitates a more stable gas outlet temperature for a fluctuating gas flow below the 'tipping point', which was attributed to the oxidation of the manganese-iron oxide particles by comparing to a moving bed based on inert manganese-iron oxide.

The heat capacity rate ratio of the 'tipping point' increased for higher particle flow rates due to a kinetic limitation, which resulted in a reduced extent of oxidation conversion with increasing flow rates. Therefore, the effective oxidation kinetics limited the attainable energy density and thermal power of the moving bed reactor. However, the energy density and thermal power followed an opposite trend if both flow rates are increased. Higher flow rates led to higher thermal power despite the reduction of the energy density of the manganese-iron oxide due to a lower residence time of the particles in a temperature range where high conversion rates are achievable. Consequently, the share of thermochemical energy in the total energy density decreased. In the end, the 'tipping point' of the metal oxide needs to be considered, since both the limited heat transfer in the nearly isothermal bed segment and oxidation kinetics confine the attainable power density of the moving bed reactor.

As a consequence of the numerical and experimental results, three operational or technical adaptations are feasible to extract both the sensible thermal energy and complete thermochemical energy of the investigated manganese-iron oxides in a moving bed reactor:

1. The increase of the oxygen partial pressure in the oxidation reactor would be beneficial for the oxidation rate. However, an increase of the oxygen partial pressure beyond ambient conditions would negate the advantage of an easy gas handling

when employing metal oxides as thermochemical energy storage.

2. Lower solid flow rates could be applied, since this would cause a higher particle residence time in a temperature range relevant for high reaction rates. However, it would also reduce the thermal power.
3. Additional indirect heat transfer in the nearly isothermal bed segment could lower the solid temperature. Besides the additional thermal energy extraction, the solid temperature is regulated to a level that allows higher reaction rates without reducing the overall gas flow. Therefore, the dimension of the isothermal bed segment is reduced and thus the power density of the moving bed reactor is increased. For example, the indirect integration of a process, which is operated isothermally at elevated temperatures could potentially enhance the extent of the conversion, e.g., a thermoelectric generator or an alkali-metal thermal-to-electric converter. In the end, the moving bed reactor would provide the thermal energy for two processes.

3.3 Evaluation of the manganese-iron-oxide application as TCS material for a continuous CSP system

Manganese-iron oxide acted as a reference material to investigate the possibility of extracting sensible thermal energy and the thermochemical energy of metal oxides in the context of a continuously operated CSP system in this work. The energy density of the investigated manganese-iron oxides is one crucial parameter to determine the competitiveness against sensible thermal storage material. Thus, in Fig. 3.2 the attained energy densities of this work are compared to theoretical values of the starting metal oxides (Mn_2O_3 / Mn_3O_4 and Fe_2O_3 / Fe_3O_4 , see also Fig. 1.2) as well as to a sensible thermal energy storage material, i.e. sintered bauxite.

The partial oxidation of the manganese-iron oxide particles and temperature reduction of about 600 °C in the moving bed experiment (paper III) with nearly steady-state operation resulted in a gravimetric energy density of around 158 Wh/kg with a thermochemical share in energy density of 21.1 %. The experimentally realized energy density is plotted for the temperature range of the characteristic nearly isothermal bed height of the moving bed, which can be attributed to the oxidation reaction.

Furthermore, the theoretical value of almost 200 Wh/kg (TGA in paper III) is displayed for the equilibrium temperature of 981 °C, which is calculated for an atmosphere containing 21 % O_2 . The discrepancy between the experimentally gained energy density (moving bed experiment in paper III) to the theoretical energy density results from the incomplete oxidation and lower temperature and thus available sensible thermal energy.

The simulation of a steady-state moving bed reactor operated with the same particle and

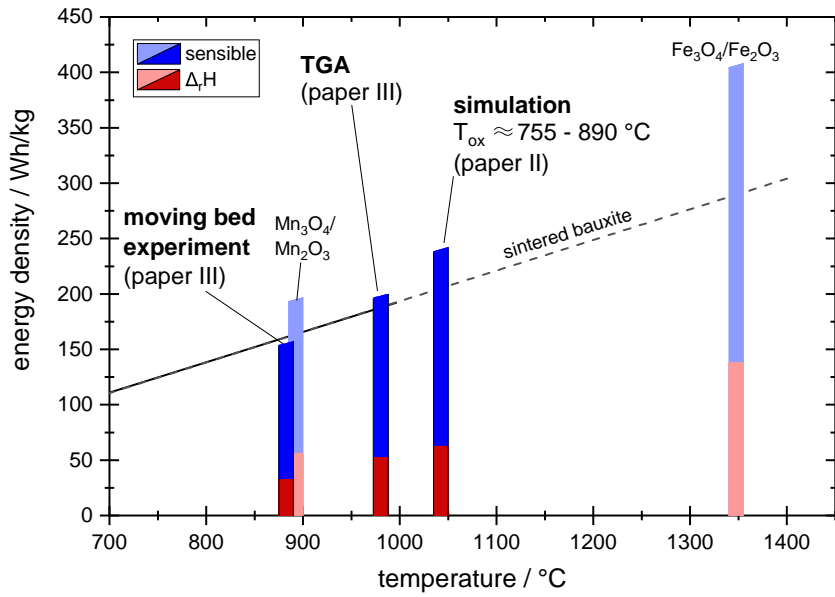


Figure 3.2 Gravimetric energy density attained at the moving bed experiment (including oxidation of $(\text{Mn}_{0.7}\text{Fe}_{0.3})_3\text{O}_4 + 20 \text{ wt.}\% \text{ ZrO}_2$, paper III) or simulation (including oxidation of $(\text{Mn}_{0.75}\text{Fe}_{0.25})_3\text{O}_4$, paper II) in comparison to the theoretical energy density of $(\text{Mn}_{0.7}\text{Fe}_{0.3})_3\text{O}_4 + 20 \text{ wt.}\% \text{ ZrO}_2$ based on the measured specific heat capacity and reaction enthalpy in TGA (paper III) displayed at the theoretical equilibrium temperature for 21 % O_2 oxygen concentration. Additionally, sintered bauxite as a sensible thermal energy material based on a lower temperature border of 300 °C [31] is depicted.

gas flow rates in comparison to the presented experiment yields the highest energy density of around 240 Wh/kg of the delineated manganese-iron oxides (paper II). The considered manganese-iron oxide in the simulation was unmodified and contained a slightly different manganese-to-iron ratio. Furthermore, the simulation assumes a particle inlet temperature greater than the oxidation temperature, in contrast to the experimentally or theoretically determined energy densities. Therefore, the energy density is increased by an additional amount of sensible thermal energy due to the cooling of the reduced phase of the metal oxides until the oxidation starts. The simulation also confirmed the incomplete oxidation resulting in an extent of conversion of 78 % and, thus, a thermochemical share in energy density of 26 %. A full conversion under the same operational conditions would result in an energy density of 258 Wh/kg.

The comparison between the energy densities of the investigated manganese-iron oxides and sintered bauxite, as a candidate for particle based thermal energy storage, reveals that the energy densities fall within a similar range at the same upper temperature threshold.

Operations with sintered bauxite in a solar receiver achieved an average receiver outlet temperature of 965 °C and thus proofed the general applicability of the material for a temperature range comparable to manganese-iron oxide particles [15]. Therefore, in terms of energy density, the manganese-iron oxides investigated in this work offer no significant advantage over sintered bauxite as a candidate for thermal energy storage. This results from the lower heat capacity in comparison to bauxite, and the low reaction enthalpy, in comparison to the redox reaction of other metal oxides.

A techno-economic analysis for the presented CSP system based on either manganese oxide, perovskite, cobalt oxide or bauxite applied as a heat transfer medium and thermo-chemical/thermal energy storage material was performed by project partners [33]. The application of manganese oxide materials showed slightly lower levelized cost of electricity (LCOE) of -1.4 % compared to bauxite, whereas the high cost of cobalt oxide negates the advantage of the high reaction enthalpy and resulted in an increase of LCOE of 43.7 % compared to bauxite as a reference. The LCOE of the investigated manganese-iron oxide can be assumed to be in the order of magnitude of the manganese oxide evaluated, since the reaction enthalpy and the raw material costs are similar. Therefore, the investigated manganese-iron-oxide does not seem to be suitable for an application in the presented CSP system, unless an additional indirect heat transfer in the nearly isothermal bed segment generates an additional benefit. Future work on metal oxides should therefore focus on materials that meet the following requirements in order to be competitive with inert thermal energy storage materials:

- The metal oxide needs to provide a higher reaction enthalpy and/or specific heat capacity in comparison to manganese-iron oxide in order to increase the energy density of the storage material.
- Faster effective oxidation kinetics of the metal oxide is necessary to overcome the kinetic limitation and increase the power density of the moving bed.
- The material cost should be comparable or lower than the cost of manganese oxide due to the large-scale availability of sintered bauxite.

Based on the results of this work, the phase transition of Fe_2O_3 / Fe_3O_4 could be an extremely interesting candidate for thermochemical energy storage that combines a high reaction enthalpy and low cost of raw material.

4 Summary

This thesis presents an experimental and numerical investigation of the heat extraction from metal oxide particles in a counter-current moving bed reactor, in context of a thermochemical energy storage system for a continuously operated point-focusing CSP plant. The focus is on a combined utilization of both the sensible thermal energy and thermochemical energy of the metal oxide particles, due to the elevated temperature level at the CSP plant. The investigation is based on manganese-iron-oxide particles as reference material, since they offer a suitable reaction temperature at ambient pressure operation in air and sufficient chemical stability of the redox reaction. The material was modified with CeO_2 , ZrO_2 , or TiO_2 , in order to mitigate the reported tendency towards agglomeration. The addition of ZrO_2 resulted in an enhanced particle stability in an attrition test rig and a significant decrease of agglomeration during redox cycles in a fixed-bed reactor. Therefore, the manganese-iron oxide was modified with ZrO_2 to allow a continuous operation of the counter-current moving bed. Thus, as a next step, the effect of the oxidation of a metal oxide particle flow on the thermal performance of a counter-current moving bed was analyzed experimentally in the scale of 2 kW and numerically with a transient 1D FEM model, resulting in the following findings:

- Both investigations revealed the formation of two distinct temperature segments along the moving bed height: One segment with nearly isothermal condition, and one segment with a distinct temperature gradient.
 - The nearly isothermal segment contributes only a negligible proportion to the oxidation conversion, since the temperature is in a range of low reaction rates, according to the numerical results. Furthermore, the heat transfer between gas and solid is limited in this segment, due to a quickly decreasing temperature difference in comparison to the segment with a distinctive temperature gradient.
 - The segment with the distinctive temperature gradients causes the major extent of metal oxide conversion, however, not to a full extent due to the high cooling rates.
- The simulation clearly demonstrates the kinetic limitation of the manganese-iron oxide, which effects the attainable energy density of the material and the thermal power of the moving bed reactor caused by an incomplete conversion and the limitation of flow rates.
- The described temperature profile of two distinctive segments in the moving bed changes to only one segment with a temperature gradient for the heat capacity rate

ratios above a material-specific 'tipping point', which is also effected by the kinetics in case of the utilized manganese-iron oxides.

- In order to increase the extent of conversion, an additional indirect heat transfer in the nearly isothermal segment has the potential to locally reduce the solid temperature to allow faster reaction rates. Thus, the moving bed reactor could provide direct heat transfer to an air flow and indirect heat transfer to a subsequent high-temperature process.
- Furthermore, the experiments indicated that future work needs to focus on the particle flowability at high temperatures to allow the utilization of metal oxide particles as a heat transfer material and thermal energy storage medium. In addition, the beneficial effect of ZrO_2 should be addressed, especially concerning the required amount of additive to possibly improve the energy density of the metal oxide particles.

In the end, a comparison of the energy densities achieved in this work with an inert material revealed a similar range of energy density for both materials. Taking also a techno-economic analysis into account for the overall CSP system, the metal oxide needs to offer a higher heat capacity than the bauxite material and/or higher reaction enthalpy than the investigated manganese-iron oxide, in order to be competitive with a purely inert operated CSP system. In this context, the phase transition of Fe_2O_3 / Fe_3O_4 could be considered in future.

Bibliography

- [1] IRENA. Renewable energy statistics 2019. Abu Dhabi, July 2019.
- [2] Guy Ervin. Solar heat storage using chemical reactions. *Journal of Solid State Chemistry*, 22(1):51–61, September 1977.
- [3] Stefan Pfenninger, Paul Gauché, Johan Lilliestam, Kerstin Damerau, Fabian Wagner, and Anthony Patt. Potential for concentrating solar power to provide baseload and dispatchable power. *Nature Climate Change*, 4(8):689–692, June 2014.
- [4] National Renewable Energy Laboratory. Shouhang dunhuang 100 mw phase ii. <https://solarpaces.nrel.gov/shouhang-dunhuang-100-mw-phase-ii>. Accessed: 2020-02-24.
- [5] B. Wong. Thermochemical heat storage for concentrated solar power. Technical report, U.S. Department of Energy, October 2011. Phase II Final Report for the period September 30, 2008 through April 30, 2011.
- [6] Mila Dieterich, Inga Bürger, and Marc Linder. Open and closed metal hydride system for high thermal power applications: Preheating vehicle components. *International Journal of Hydrogen Energy*, 42(16):11469–11481, April 2017.
- [7] Christos Agrafiotis, Martin Roeb, Martin Schmücker, and Christian Sattler. Exploitation of thermochemical cycles based on solid oxide redox systems for thermochemical storage of solar heat. part 1: Testing of cobalt oxide-based powders. *Solar Energy*, 102:189–211, April 2014.
- [8] Alfonso J. Carrillo, Javier Moya, Alicia Bayón, Prabhas Jana, Víctor A. de la Peña O’Shea, Manuel Romero, José Gonzalez-Aguilar, David P. Serrano, Patricia Pizarro, and Juan M. Coronado. Thermochemical energy storage at high temperature via redox cycles of Mn and Co oxides: Pure oxides versus mixed ones. *Solar Energy Materials and Solar Cells*, 123:47–57, April 2014.
- [9] Tina Block and Martin Schmücker. Metal oxides for thermochemical energy storage: A comparison of several metal oxide systems. *Solar Energy*, 126:195–207, March 2016.
- [10] Laurie André, Stéphane Abanades, and Gilles Flamant. Screening of thermochemical systems based on solid-gas reversible reactions for high temperature solar thermal

- energy storage. *Renewable and Sustainable Energy Reviews*, 64:703–715, October 2016.
- [11] P. K. Falcone, J. E. Noring, and C. E. Hacket. Evaluation and application of solid thermal energy carriers in a high temperature solar central receiver system. In *Seventeenth Intersociety Energy Conversion Engineering Conference*. IECEC, IECEC, 1982.
 - [12] Nathan Siegel and Greg Kolb. Design and on-sun testing of a solid particle receiver prototype. In *ASME 2008 2nd International Conference on Energy Sustainability, Volume 2*. ASMEDC, January 2008.
 - [13] Gilles Flamant, Daniel Gauthier, Hadrien Benoit, Jean-Louis Sans, Roger Garcia, Benjamin Boissière, Renaud Ansart, and Mehdi Hemati. Dense suspension of solid particles as a new heat transfer fluid for concentrated solar thermal plants: On-sun proof of concept. *Chemical Engineering Science*, 102:567–576, October 2013.
 - [14] W. Wu, L. Amsbeck, R. Buck, R. Uhlig, and R. Ritz-Paal. Proof of concept test of a centrifugal particle receiver. *Energy Procedia*, 49:560–568, 2014.
 - [15] Miriam Ebert, Lars Amsbeck, Jens Rheinländer, Bärbel Schlögl-Knothe, Stefan Schmitz, Marcel Sibum, Ralf Uhlig, and Reiner Buck. Operational experience of a centrifugal particle receiver prototype. In *SOLARPACES 2018: International Conference on Concentrating Solar Power and Chemical Energy Systems*. AIP Publishing, 2019.
 - [16] Z. Ma, G.C. Glatzmaier, and M. Mehos. Development of solid particle thermal energy storage for concentrating solar power plants that use fluidized bed technology. *Energy Procedia*, 49:898–907, 2014.
 - [17] Andrew J. Schrader, Alexander P. Muroyama, and Peter G. Loutzenhiser. Solar electricity via an air brayton cycle with an integrated two-step thermochemical cycle for heat storage based on $\text{Co}_3\text{O}_4/\text{CoO}$ redox reactions: Thermodynamic analysis. *Solar Energy*, 118:485–495, August 2015.
 - [18] Christos Agrafiotis, Lamark de Oliveira, Martin Roeb, and Christian Sattler. A solar receiver-storage modular cascade based on porous ceramic structures for hybrid sensible/thermochemical solar energy storage. *SolarPACES, AIP Conference Proceedings*, 1734, May 2016. ISBN: 978-0-7354-1386-3.
 - [19] Christos Agrafiotis, Andreas Becker, Martin Roeb, and Christian Sattler. Exploitation of thermochemical cycles based on solid oxide redox systems for thermochemical

- storage of solar heat. Part 5: Testing of porous ceramic honeycomb and foam cascades based on cobalt and manganese oxides for hybrid sensible/thermochemical heat storage. *Solar Energy*, 139:676–694, December 2016.
- [20] Mehdi Jafarian, Maziar Arjomandi, and Graham J. Nathan. Thermodynamic potential of molten copper oxide for high temperature solar energy storage and oxygen production. *Applied Energy*, 201:69–83, September 2017.
- [21] Christos Agrafiotis, Martin Roeb, and Christian Sattler. Exploitation of thermochemical cycles based on solid oxide redox systems for thermochemical storage of solar heat. part 4: Screening of oxides for use in cascaded thermochemical storage concepts. *Solar Energy*, 139:695–710, December 2016.
- [22] S Abanades, P Charvin, G Flamant, and P Neveu. Screening of water-splitting thermochemical cycles potentially attractive for hydrogen production by concentrated solar energy. *Energy*, 31(14):2805–2822, November 2006.
- [23] Manuel Romero and Aldo Steinfeld. Concentrating solar thermal power and thermochemical fuels. *Energy & Environmental Science*, 5(11):9234, 2012.
- [24] Mahesh M. Nair and Stéphane Abanades. Experimental screening of perovskite oxides as efficient redox materials for solar thermochemical CO₂ conversion. *Sustainable Energy & Fuels*, 2(4):843–854, 2018.
- [25] Josua Vieten, Brendan Bulfin, Patrick Huck, Matthew Horton, Dorottya Guban, Liya Zhu, Youjun Lu, Kristin A. Persson, Martin Roeb, and Christian Sattler. Materials design of perovskite solid solutions for thermochemical applications. *Energy & Environmental Science*, 12(4):1369–1384, 2019.
- [26] Cindy Y. Lau, Matthew T. Dunstan, Wenting Hu, Clare P. Grey, and Stuart A. Scott. Large scale in silico screening of materials for carbon capture through chemical looping. *Energy & Environmental Science*, 10(3):818–831, 2017.
- [27] A. Fossdal, E. Bakken, B.A. Øye, C. Schøning, I. Kaus, T. Møkkelbost, and Y. Larring. Study of inexpensive oxygen carriers for chemical looping combustion. *International Journal of Greenhouse Gas Control*, 5(3):483–488, May 2011.
- [28] Sebastian Sundqvist, Mehdi Arjmand, Tobias Mattisson, Magnus Rydén, and Anders Lyngfelt. Screening of different manganese ores for chemical-looping combustion (CLC) and chemical-looping with oxygen uncoupling (CLOU). *International Journal of Greenhouse Gas Control*, 43:179–188, December 2015.

- [29] Anders Lyngfelt, Anders Brink, Øyvind Langørgen, Tobias Mattisson, Magnus Rydén, and Carl Linderholm. 11,000 h of chemical-looping combustion operation - Where are we and where do we want to go? *International Journal of Greenhouse Gas Control*, 88:38–56, September 2019.
- [30] Ihsan Barin and Gregor Platzki. *Thermochemical Data of Pure Substances*. VCH Verlagsgesellschaft mbH, 3 edition, October 1995.
- [31] T. Baumann and S. Zunft. Properties of granular materials as heat transfer and storage medium in CSP application. *Solar Energy Materials and Solar Cells*, 143:38–47, December 2015.
- [32] K. Hutchings, M. Wilson, P. Larsen, and R. Cutler. Kinetic and thermodynamic considerations for oxygen absorption/desorption using cobalt oxide. *Solid State Ionics*, 177(1-2):45–51, January 2006.
- [33] Reiner Buck, Stefania Tescari, Martin Schmücker, Nicole Preisner, and Christos Agrafiotis. Techno-economic analysis of thermochemical storage for csp systems. In *SOLARPACES 2019: International Conference on Concentrating Solar Power and Chemical Energy Systems*, 2019.
- [34] Laurie André, Stéphane Abanades, and Laurent Cassayre. High-temperature thermochemical energy storage based on redox reactions using Co-Fe and Mn-Fe mixed metal oxides. *Journal of Solid State Chemistry*, 253:6–14, September 2017.
- [35] Alfonso J. Carrillo, David P. Serrano, Patricia Pizarro, and Juan M. Coronado. Thermochemical heat storage based on the $\text{Mn}_2\text{O}_3/\text{Mn}_3\text{O}_4$ redox couple: influence of the initial particle size on the morphological evolution and cyclability. *J. Mater. Chem. A*, 2(45):19435–19443, October 2014.
- [36] Alfonso J. Carrillo, David P. Serrano, Patricia Pizarro, and Juan M. Coronado. Improving the thermochemical energy storage performance of the $\text{Mn}_2\text{O}_3/\text{Mn}_3\text{O}_4$ redox couple by the incorporation of iron. *ChemSusChem*, 8(11):1947–1954, April 2015.
- [37] R.G. Bowrey and J. Jutsen. Energy storage using the reversible oxidation of barium oxide. *Solar Energy*, 21(6):523–525, 1978.
- [38] M. A. Fahim and J. D. Ford. Energy storage and using the bao-bao and reaction cycle. *The Chemical Engineering Journal*, 1983.
- [39] A. J. Carrillo, D. Sastre, D. P. Serrano, P. Pizarro, and J. M. Coronado. Revisiting the BaO_2/BaO redox cycle for solar thermochemical energy storage. *Physical Chemistry Chemical Physics*, 18(11):8039–8048, 2016.

- [40] M. Hänchen, A. Stiel, Z. R. Jovanovic, and A. Steinfeld. Thermally driven copper oxide redox cycle for the separation of oxygen from gases. *Industrial & Engineering Chemistry Research*, 51(20):7013–7021, May 2012.
- [41] Elisa Alonso, Carlos Pérez-Rábago, Javier Licurgo, Edward Fuentealba, and Claudio A. Estrada. First experimental studies of solar redox reactions of copper oxides for thermochemical energy storage. *Solar Energy*, 115:297–305, May 2015.
- [42] Hossein Beidaghy Dizaji and Hannaneh Hosseini. A review of material screening in pure and mixed-metal oxide thermochemical energy storage (TCES) systems for concentrated solar power (CSP) applications. *Renewable and Sustainable Energy Reviews*, 98:9–26, December 2018.
- [43] Tina Block, Nicole Knoblauch, and Martin Schmücker. The cobalt-oxide/iron-oxide binary system for use as high temperature thermochemical energy storage material. *Thermochimica Acta*, 577:25–32, February 2014.
- [44] Alfonso J. Carrillo, David P. Serrano, Patricia Pizarro, and Juan M. Coronado. Understanding redox kinetics of iron-doped manganese oxides for high temperature thermochemical energy storage. *The Journal of Physical Chemistry C*, 120(49):27800–27812, December 2016.
- [45] Michael Wokon, Tina Block, Sven Nicolai, Marc Linder, and Martin Schmücker. Thermodynamic and kinetic investigation of a technical grade manganese-iron binary oxide for thermochemical energy storage. *Solar Energy*, 153:471–485, September 2017.
- [46] Duygu Yilmaz, Esraa Darwish, and Henrik Leion. Investigation of the combined mn-si oxide system for thermochemical energy storage applications. *Journal of Energy Storage*, 28:101180, April 2020.
- [47] Sean M. Babiniec, Eric N. Coker, James E. Miller, and Andrea Ambrosini. Doped calcium manganites for advanced high-temperature thermochemical energy storage. *International Journal of Energy Research*, 40(2):280–284, December 2015.
- [48] A. Muan and S. Somiya. The system iron oxide-manganese oxide in air. *American Journal of Science*, 260:230 – 240, 1962.
- [49] D. G. Wickham. The chemical composition of spinels in the system $\text{Fe}_3\text{O}_4\text{-Mn}_3\text{O}_4$. *Journal of inorganic nuclear Chemistry*, 31:313 – 320, 1969.
- [50] Lina Kjellqvist and Malin Selleby. Thermodynamic assessment of the Fe-Mn-O system. *Journal of Phase Equilibria and Diffusion*, 31(2):113–134, February 2010.

- [51] Jarrod V. Crum, Brian J. Riley, and John D. Vienna. Binary phase diagram of the manganese oxide-iron oxide system. *Journal of the American Ceramic Society*, 92(10):2378–2384, October 2009.
- [52] Youn-Bae Kang and In-Ho Jung. Thermodynamic modeling of oxide phases in the Fe–Mn–O system. *Journal of Physics and Chemistry of Solids*, 98:237–246, November 2016.
- [53] Lauren Farcot, Nolwenn Le Pierrès, Benoit Michel, Jean-François Fourmigué, and Philippe Papillon. Numerical investigations of a continuous thermochemical heat storage reactor. *Journal of Energy Storage*, 20:109–119, December 2018.
- [54] Sike Wu, Cheng Zhou, Elham Doroodchi, Rajesh Nellore, and Behdad Moghtaderi. A review on high-temperature thermochemical energy storage based on metal oxides redox cycle. *Energy Conversion and Management*, 168:421–453, July 2018.
- [55] M. Neises, S. Tescari, L. de Oliveira, M. Roeb, C. Sattler, and B. Wong. Solar-heated rotary kiln for thermochemical energy storage. *Solar Energy*, 86(10):3040–3048, October 2012.
- [56] Stefania Tescari, Pradeepkumar Sundarraj, Gkiokchan Moumin, Juan Pablo Rincon Duarte, Christos Agrafiotis, Lamark de Oliveira, Christian Willsch, Martin Roeb, and Christian Sattler. Solar rotary kiln for continuous treatment of particle material: Chemical experiments from micro to milli meter particle size. In *SOLARPACES 2019: International Conference on Concentrating Solar Power and Chemical Energy Systems*, 2019.
- [57] Andrew S. Oles and Gregory S. Jackson. Modeling of a concentrated-solar, falling-particle receiver for ceria reduction. *Solar Energy*, 122:126–147, December 2015.
- [58] Andrew J. Schrader. *Design modeling and testing of a solar thermochemical inclined granular flow reactor for concentrated solar power*. PhD thesis, G. W. Woodruff School of Mechanical Engineering, 2019.
- [59] Fuliang Nie, Zhiying Cui, Fengwu Bai, and Zhifeng Wang. Properties of solid particles as heat transfer fluid in a gravity driven moving bed solar receiver. *Solar Energy Materials and Solar Cells*, 200:110007, September 2019.
- [60] Elisa Alonso, Fabrisio Gómez, José Gonzalez-Aguilar, and Manuel Romero. Experimental analysis of Mn_3O_4 / MnO reduction in a packed-bed type solar reactor: Oxygen partial pressure influence. *Proceedings of SolarPACES Conference 2011*, September 2011.

- [61] Abhishek Singh, Justin Lapp, Johannes Grobbel, Stefan Brendelberger, Jan P. Reinhold, Lamark Olivera, Ivan Ermanoski, Nathan P. Siegel, Anthony McDaniel, Martin Roeb, and Christian Sattler. Design of a pilot scale directly irradiated, high temperature, and low pressure moving particle cavity chamber for metal oxide reduction. *Solar Energy*, 157:365–376, November 2017.
- [62] Samantha J. Kopping, Jack Hoeniges, Jesse Greenhagen, Zachary Matejczyk, and Luke J. Venstrom. Model of the solar-driven reduction of cobalt oxide in a particle suspension reactor. *Solar Energy*, 177:713–723, January 2019.
- [63] Gregory S. Jackson, Luca Imponenti, Kevin J. Albrecht, Daniel C. Miller, and Robert J. Braun. Inert and reactive oxide particles for high-temperature thermal energy capture and storage for concentrating solar power. *Journal of Solar Energy Engineering*, 141(2), January 2019.
- [64] Andrew J. Schrader, Gianmarco De Dominicis, Garrett L. Schieber, and Peter G. Loutzenhiser. Solar electricity via an air brayton cycle with an integrated two-step thermochemical cycle for heat storage based on $\text{Co}_3\text{O}_4/\text{CoO}$ redox reactions III: Solar thermochemical reactor design and modeling. *Solar Energy*, 150:584–595, July 2017.
- [65] Fuliang Nie, Fengwu Bai, Zhiying Cui, Ziwei Zhao, and Zhifeng Wang. Cold-state experimental study on discharge characteristics of solid particles in a gravity driven moving bed solar receiver. *Solar Energy*, 195:14–26, January 2020.
- [66] S. Ströhle, A. Haselbacher, Z. R. Jovanovic, and A. Steinfeld. The effect of the gas–solid contacting pattern in a high-temperature thermochemical energy storage on the performance of a concentrated solar power plant. *Energy & Environmental Science*, 9(4):1375–1389, 2016.
- [67] 10th International Conference on Energy Sustainability. *Considerations for the design of a high-temperature particle reoxidation reactor for extraction of heat in thermochemical energy storage systems*, number ES2016-59646, Charlotte, North Carolina, June 2016.
- [68] Andrea Ambrosini, James E Miller, Sean Michael Babiniec, Peter Loutzenhiser, Ellen B. Stechel, Sheldon Jeter, and Hany Al-Ansary. High performance reduction/oxidation metal oxides for thermochemical energy storage (promotes): A project overview. Technical report, June 2018.

- [69] Sandra Álvarez de Miguel. *Analysis of redox reactions in a fluidized/fixed bed reactor for thermochemical energy storage in solar thermal power plants*. PhD thesis, Universidad Politécnica de Madrid, 2017.
- [70] Michael Wokon, Andreas Kohzer, and Marc Linder. Investigations on thermochemical energy storage based on technical grade manganese-iron oxide in a lab-scale packed bed reactor. *Solar Energy*, 153:200–214, September 2017.
- [71] Magnus Rydén, Anders Lyngfelt, and Tobias Mattisson. Combined manganese/iron oxides as oxygen carrier for chemical looping combustion with oxygen uncoupling (CLOU) in a circulating fluidized bed reactor system. *Energy Procedia*, 4:341–348, 2011.
- [72] Alberto Abad, Iñaki Adánez-Rubio, Pilar Gayán, Francisco García-Labiano, Luis F. de Diego, and Juan Adánez. Demonstration of chemical-looping with oxygen uncoupling (CLOU) process in a 1.5kW_{th} continuously operating unit using a Cu-based oxygen-carrier. *International Journal of Greenhouse Gas Control*, 6:189–200, January 2012.
- [73] Pontus Markström, Carl Linderholm, and Anders Lyngfelt. Operation of a 100 kW chemical-looping combustor with mexican petroleum coke and cerrejón coal. *Applied Energy*, 113:1830–1835, January 2014.
- [74] Jochen Ströhle, Matthias Orth, and Bernd Epple. Chemical looping combustion of hard coal in a 1 MW_{th} pilot plant using ilmenite as oxygen carrier. *Applied Energy*, 157:288–294, November 2015.
- [75] Lei Xu, Hongming Sun, Zhenshan Li, and Ningsheng Cai. Experimental study of copper modified manganese ores as oxygen carriers in a dual fluidized bed reactor. *Applied Energy*, 162:940–947, January 2016.
- [76] Andrew Tong, Liang Zeng, Mandar V. Kathe, Deepak Sridhar, and Liang-Shih Fan. Application of the moving-bed chemical looping process for high methane conversion. *Energy & Fuels*, 27(8):4119–4128, March 2013.
- [77] Andrew Tong, Deepak Sridhar, Zhenchao Sun, Hyung R. Kim, Liang Zeng, Fei Wang, Dawei Wang, Mandar V. Kathe, Siwei Luo, Yuhao Sun, and Liang-Shih Fan. Continuous high purity hydrogen generation from a syngas chemical looping 25 kW_{th} sub-pilot unit with 100% carbon capture. *Fuel*, 103:495–505, January 2013.
- [78] Liang Zeng, Andrew Tong, Mandar Kathe, Samuel Bayham, and Liang-Shih Fan. Iron oxide looping for natural gas conversion in a countercurrent moving bed reactor. *Applied Energy*, 157:338–347, November 2015.

- [79] Cetera Chen, Hsiu-Hsia Lee, Wilson Chen, Yu-Cheng Chang, Eric Wang, Cheng-Hsien Shen, and Kuo-En Huang. Study of an iron-based oxygen carrier on the moving bed chemical looping system. *Energy & Fuels*, 32(3):3660–3667, February 2018.
- [80] Cetera Chen, Chien-Hua Chen, Ming-Hui Chang, Hsiu-Hsia Lee, Yu-Cheng Chang, Tzeng-Wen Wen, Cheng-Hsien Shen, and Hou-Peng Wan. A 30-kWth moving-bed chemical looping system for hydrogen production. *International Journal of Greenhouse Gas Control*, 95:102954, April 2020.
- [81] Golnar Azimi, Henrik Leion, Magnus Rydén, Tobias Mattisson, and Anders Lyngfelt. Investigation of different mn–fe oxides as oxygen carrier for chemical-looping with oxygen uncoupling (CLOU). *Energy & Fuels*, 27(1):367–377, December 2012.
- [82] Golnar Azimi, Henrik Leion, Tobias Mattisson, Magnus Rydén, Frans Snijkers, and Anders Lyngfelt. Mn–fe oxides with support of MgAl_2O_4 , CeO_2 , ZrO_2 and $\text{Y}_2\text{O}_3\text{--ZrO}_2$ for chemical-looping combustion and chemical-looping with oxygen uncoupling. *Industrial & Engineering Chemistry Research*, 53(25):10358–10365, June 2014.